Effect of VC, Cr_3C_2 and Ru Additives on Mechanical Properties of WC-10wt%Co Sintered with Spark Plasma Sintering

MSc Dissertation

Prepared by

Sibusiso Luthuli 900957

Submitted to

School of Chemical and Metallurgical Engineering, Faculty of Engineering and the Built Environment, University of the Witwatersrand, Johannesburg,

South Africa

2022

DECLARATION

I, Sibusiso Tholinhlanhla Luthuli

(Student number: 900957) am a student registered for Master of Science in Engineering

in the year 2021. I hereby declare the following:

I am aware that plagiarism (the use of someone else's work without their permission and/or without acknowledging the original source) is wrong. I confirm that the work submitted for assessment for the above course is my own unaided work except where I have explicitly indicated otherwise. I have followed the required conventions in referencing the thoughts and ideas of others. I understand that the University of the Witwatersrand may take disciplinary action against me if there is a belief that this is not my own unaided work or that I have failed to acknowledge the source of the ideas or words in my writing.

Student Signature: _____ Date: _____

Abstract

This dissertation presents the effect of VC, Cr_3C_2 and Ru additives on the mechanical properties of WC-10wt%Co manufactured using spark plasma sintering (SPS). Spark plasma sintering has the advantage of being a high-speed sintering process and achieves full densification (>99%) at a lower sintering temperature than other conventional sintering techniques, thereby preventing Ostwald ripening. The study involved the characterisation of the microstructures of both powder and sintered samples morphology and phases present using optical microscopy, particle size analyser, SEM and XRD. Eight samples were made with a composition of 0.2 wt% of the grain growth inhibitors (VC, Cr_3C_2 and Ru) and base sample of WC-10wt%Co. The powders were milled using a planetary ball mill with 4:1 ball-to-powder ratio. Powders were sintered in SPS at 1150°C for 8 minutes at 50MPa under vacuum and the relative density of all samples was above 99%. The addition of grain growth inhibitors successfully decreased the WC grain size from a maximum of 0.524 ± 0.003 µm to a minimum of 0.489 ± 0.002 µm. The binder mean free path and WC contiguity was dependent on the amount of WC/WC contact, and smaller WC grain size resulted increased Co binder between WC, thus lowering the number of WC/WC contacts. Therefore, decreasing the binder mean free path increased the hardness of the samples. Since there was an inverse relationship between binder mean free path and WC contiguity, a lower WC contiguity resulted in a lower hardness and an increase in fracture toughness.

Dedications

I dedicate this work to myself, my family for always believing in me and for always seeing what is best for me.

This dedication also extends to my mother Philisiwe Goodness Luthuli for believing in me even when I am at my lowest point in life.

Acknowledgements

My sincere gratitude is extended to:

- **Professor Lesley Cornish,** for suggesting the project and guidance throughout the project, her patience and providing great leadership and allowing me to grow.
- **Dr David Whitefield,** for his great supervision, guidance and his extensive knowledge and advice.
- **DSI-NRF Centre of Excellence in Strong Materials,** South Africa for their financial support and providing a bursary.
- **AMSEN**: African Materials Science and Engineering Network (AMSEN), A Carnegie – IAS RISE Network for their extra financial support.
- **School of Chemical and Metallurgical Engineering, University of the Witwatersrand** for affording me the opportunity to study, and all Postgraduate students in Richard Ward 418 for their support.
- **My Family** for believing in me**.**

Table of Contents

List of Figures

List of Tables

Chapter One

1. Introduction

Tungsten carbide - cobalt (WC-Co) is a composite of tungsten particles with metallic cobalt as a binder, sintered at high temperatures (Upadhyaya, 2001). WC-Co possesses superior mechanical properties, due to the wettability of tungsten by cobalt and with tungsten carbide grain size below 0.1 µm, they have excellent abrasive wear resistance compared to steels (Chabretou *et al*., 2003). Thus, WC-Co is commonly used in cutting tools, drilling and wear resistant machine parts.

Cemented carbides are commonly used in mining for drilling due to their high hardness and wear resistance. WC-Co hardness and wear resistance can be improved by reducing the WC grain size. Fracture toughness can be increased by increasing the cobalt content in the binder, which is why WC-Co cements with 5-10 wt% Co are common, since they provide a good balance of fracture toughness and hardness (Wei *et al*., 2015; Siwak *et al*., 2016). The most successful way of controlling WC grain growth is by addition of transition metal carbides such as VC, Cr_3C_2, NbC, TaC, TiC and Mo_2C within a range of 0.1 - 1 wt% (Huang *et al*., 2007).

Full densification of WC-Co has been achieved by conventional sintering, spark plasma sintering (SPS), hot isostatic pressing (HIP), plasma pressure compacting and dynamic shock compressing, with SPS being the most effective thus far (Hwan *et al*., 2004). Spark plasma sintering, which is also known as pulse electric current sintering (PECS), is a process that combines a fast-heating rate by flowing a pulsed electric current through the die, punch and powder compact set-up under an applied pressure (Haung *et al*., 2006).

Typical hard-facings on softer materials include WC-Co of varying Co contents, and this affects the binding of the hard-facings. Under abrasive wear conditions, the binder is rapidly removed, which then allows the hard WC particles to be easily removed (Upadhyaya, 2001). Thus, a technique of strengthening the binder is needed.

1.1. Aim of the project

This project focused on strengthening the cobalt binder in WC-10wt%Co by additions of VC, Cr_3C_2 and Ru in sufficient amounts to increase the overall mechanical and microstructural properties of the material. Eight alloys based on WC-10wt%Co with different amounts of the grain growth inhibitors substituting WC were studied. The microstructures were characterised by X-ray diffraction and scanning electron microscopy with energy dispersive X-ray analysis. The aim of this project was to compare the effect of the different grain growth inhibitors, and their combinations, on cemented carbide properties.

1.2. Objections of the Study

The objections of this research are

- To strengthen WC-10wt%Co by additions of VC, Cr_3C_2 and Ru while retaining its mechanical properties and increase its wear resistance.
- To increate WC-10wt%Co density and mechanical properties by using Spark Plasma Sintering process as oppose the conventional way of sintering which tends decrease in density.
- To study the influence of the additives on grain size of the WC grains, the WC grain contiguity and Co binder mean free path

1.3. Hypothesis

Based on the benefits in mechanical properties, and microstructure WC-Co cemented carbides with transitional metal additives has been a subject of study over the years. Several studies have been carried our involving the improvement on WC-Co manufacturing and strengthen of WC-Co cemented carbide while returning it's fracture toughness. This research will therefore focus on adding Ru, VC and Cr_3C_2 to change the microstructure and mechanical properties of WC-Co. By changing the production of the cemented carbides using SPS instead of the conventional way of sintering, it is expected that this will reduce sintering time and increase density of the samples.

1.4. Research Questions

The research question of this projects is

- Are additives of 0.2 wt% to WC-10wt%Co enough to improve the mechanical properties?
- Does SPS sintered WC-Co cause diffusion of additives when the sintering temperature is increased to 1250°C from 1150°C?
- Does the sintering temperature and pressure play a role on densification process on SPSed WC-Co materials?

Layout of the dissertation

The dissertation begins with a brief description of the method of investigation in Chapter 1 before describing the important features of WC-Co Cemented carbides using relevant literature in Chapter 2. It then moves on to the experimental procedure in Chapter 3 and the results in Chapter 4. The discussion is given in Chapter 5 and the conclusion in Chapter 6.

Chapter Two

2. Background and literature survey

Cemented carbides are one of the mostly used materials in mining sector because of their strong mechanical properties. They are composite materials that consist of tungsten cobalt and carbon, thus, WC-Co. Tungsten carbides can be used as cutting tools, drills, milling inserts etc. Tungsten carbide's unique strength and hardness which satisfies the most demanding applications. The different shapes and sizes in which the materials can be produced using modern technology as opposed to conventional production and designing these materials offer a range of cost-effective metallurgical products. This study thus focused on conventional and SPS sintered material literature on cemented carbides with additives, and ways of improving their mechanical properties, microstructural properties and effective way of sintering using SPS.

2.1. Properties of hardmetals

The main component of cemented carbides is the hard and brittle WC particles, with a Co, Ni or Fe binder material. Cemented carbides are usually improved by the addition of transition metal carbides to obtain superior mechanical properties (Upadhyaya, 2001). Transition metal carbides have similar characteristics to each other, including their structures leading to a mixture of ionic, metallic and covalent bonds (Upadhyaya, 2001).

Cemented carbides are known as hardmetals in most parts of the world. In manufacturing hardmetals, cemented carbide can be too brittle for industrial use, and some toughness was required (Upadhyaya, 2001). Mixing tungsten carbide (WC) powder with up to 30 wt% of metals such as cobalt, iron or nickel pressed and sintered at about 1450°C provided toughness, high hardness and a low level of porosity to the hard metals (Jones *et al*., 2004).

WC-Co properties can be metallurgically modified to suit a specific application. The starting materials are in the form of powders that are pressed to shape using powder metallurgy

techniques. The pressed shape is referred to as a green body which is then heated to approximately 1450°C at a rate of 600°C/min (Siwak *et al*., 2017). During sintering a gas pressure can be applied and kept between 55-65 MPa throughout the sintering process to achieve full densification.

Tungsten carbide (WC) and cobalt are the most used hard and binder phase in hardmetals (Upadhyaya, 2001). Over the years, researchers have spent time trying to improve the WC-Co compositions to gain even better mechanical properties with the addition of carbides such as chromium carbide (Cr_3C_2), vanadium carbide (VC), titanium carbides (TiC), tantalum carbide (TaC) or niobium carbide (NbC). Cemented carbides with chromium, iron, nickel, or molybdenum binder phase can be produced (Sandvik, 1998).

2.2. Production of cemented carbides

Conventional WC-Co production

The conventional way of cemented carbide production is shown in Figure 2.1 where WC is the main component with Co as the binder. The starting material of WC is sometimes partially replaced by additive carbides. The traditional sintering required heating in a sealed furnace to about 1400°C to sinter materials with a low cobalt content (6 wt%). This was a traditional way of sintering which has been tested and applied by many manufacturing companies (Upadhyaya, 2001). The development of a more efficient way of sintering was needed since the latter was not time efficient, because it took a long time to produce a component and the density was often low, implying porosity was present (Upadhyaya, 2001). The spark plasma sintering (SPS) process (Figure 2.2) is one of the most efficient ways of cemented carbide manufacturing that is still being tested by many (Upadhyaya, 2001).

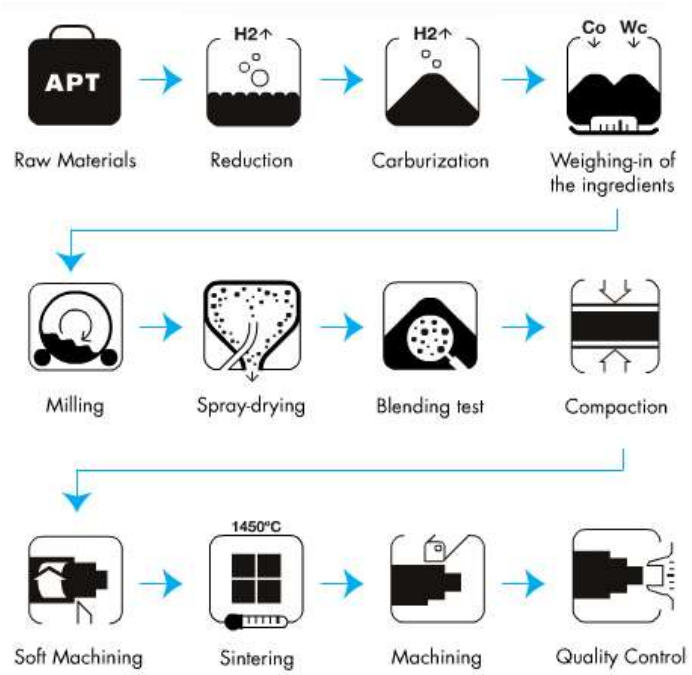

Figure 2.1 Consolidation of cemented carbides (Upadhyaya, 2001).

Hardmetal manufacturing processes vary but follow the same general production route. The conventional processing route involves mixing the binder and tungsten carbide powders, followed by milling the powders and pressing them into green compacts (Figure 2.1), then sintering them at the desired temperature and pressure (Haung *et al*., 2006).

Milling is the first stage in cemented carbide production and is done with methanol for lubrication and wax to increase the strength of the green powder compacts (Upadhyaya, 2001). Exhaustive milling is done to crush the initial carbide grains to the desired size, and to combine different components, so that every carbide particle is coated by the binder material. Milling also ensures the even distribution of the binder material, to avoid large binder islands and agglomeration in the sintered product (Haung et al., 2006). Carbide mixtures are wet milled using rotary, vibratory or attrition mills, with rotary mills such as ball mills being commonly used due to their ready availability and lower associated costs (Haung *et al.*, 2006).

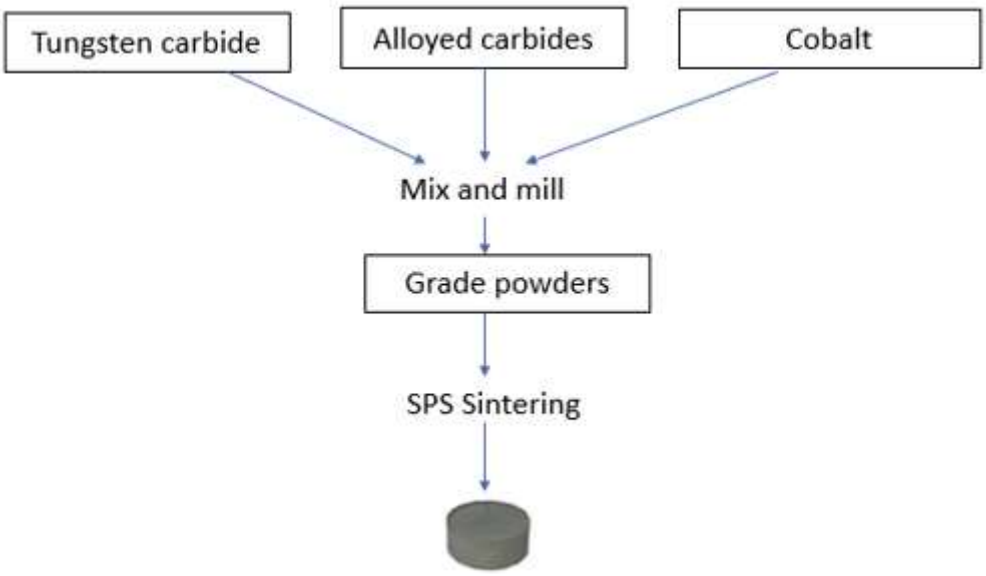

Figure 2.2 Schematic diagram of cemented carbide production (Haung *et al*., 2006).

The production steps of WC-Co are as follows (Haung *et al*., 2006):

- Step 1: Tungsten carbide and binder powders are produced.
- Step 2: The powders are then mixed and milled in the presence of a wax binder and organic solvents, such as ethanol
- Step 3: Spark plasma sintering to the desired temperature to increase diffusion of Co binder and WC matrix while simultaneously increasing pressure to eradicate all porosity.

2.3. Liquid Phase Sintering (LPS)

The phenomenon of liquid phase sintering (LPS) helps with mechanically alloyed powders and composites such as WC-Co (Upadhyaya, 2001). The sintering temperatures are such that the binder phase is melted and not the WC phase. This allows the liquid to bond to the WC grains, after spreading over the solid particles and filling the pores. During the process of LPS, a low melting point liquid is used for rapid sintering, where the liquid wets the particles due to a low contact angle (Jaydeep, 2014). A liquid film then provides the surface tension force for maximum densification. The entire densification in LPS is characterised in three stages which include liquid spreading, which helps with rearrangement of particles, solution re-

precipitation and solid phase bonding. The full process is shown in Figure 2.3 (Jaydeep, 2014). On heating, small particles of the binder material melt and this continues until saturation is reached and on cooling, the grains grow by nucleation and recrystallisation.

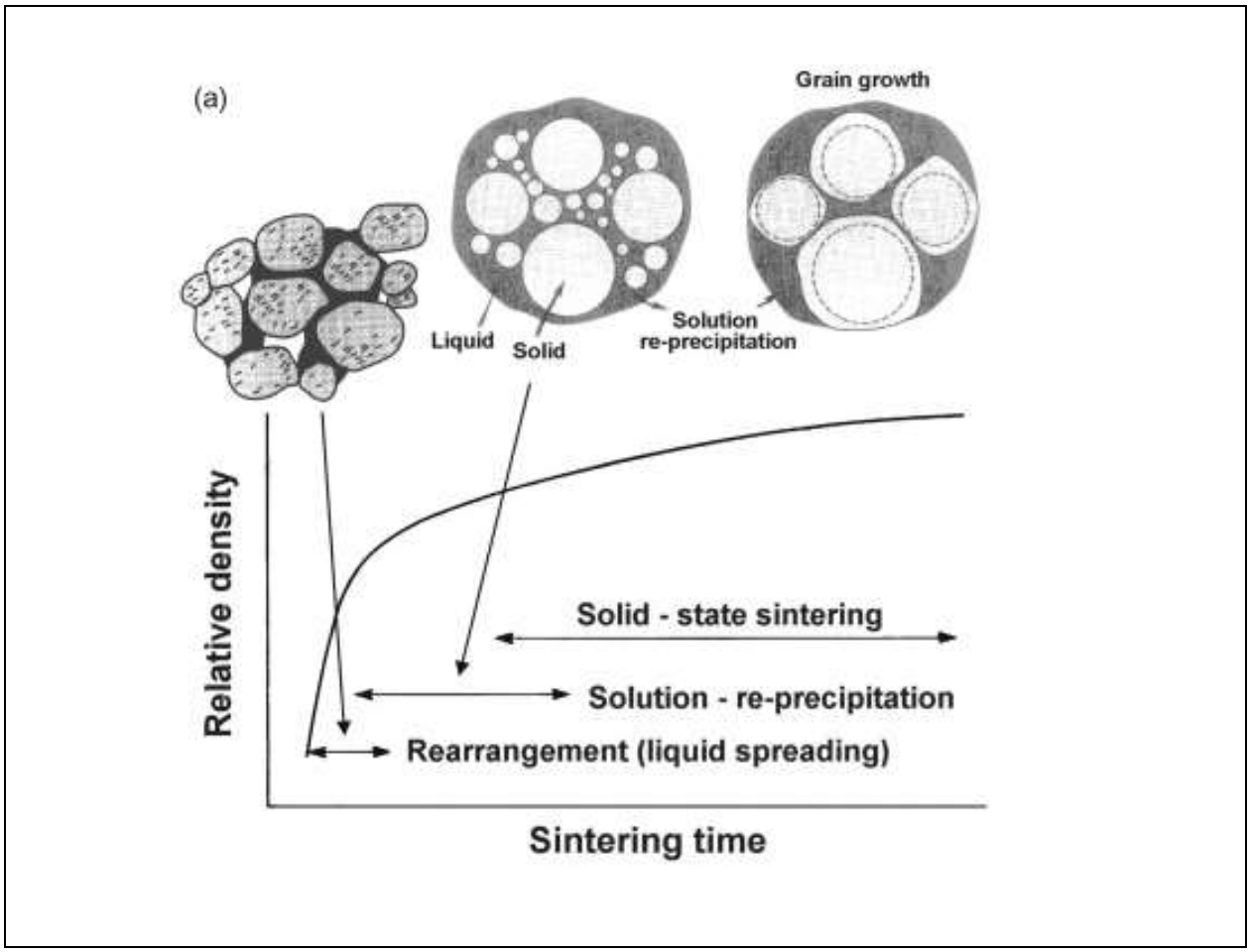

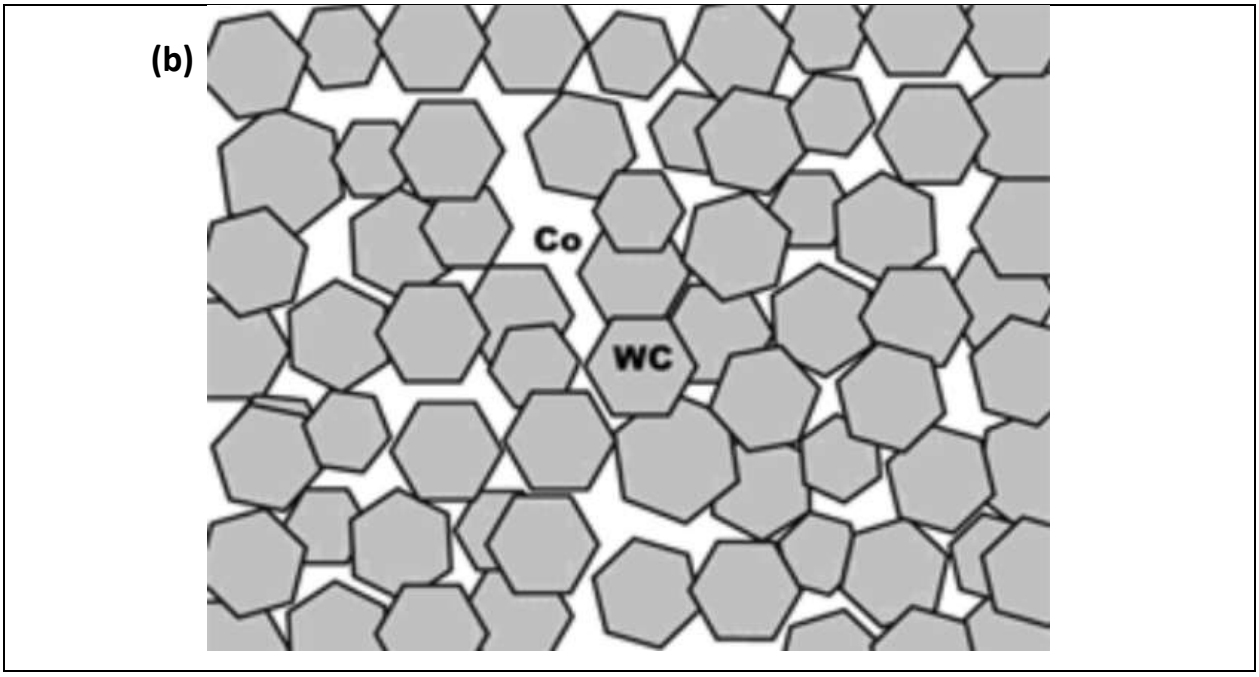

Figure 2.3 Liquid phase sintering (a) stages of LPS, (b) resultant microstructure (Jaydeep, 2014).

During the heating cycle, the densification mechanism changes from liquid spreading to re-precipitation, and then to solid state sintering where pores are removed (Jaydeep, 2014). The densification process in LPS is driven by thermodynamic forces to reduce interfacial free energy of the system (Jaydeep, 2014). The change in free energy when going from solid-liquid-vapour system is given by Equation 2.1.

$$\Delta G = \Delta A_{SV}\gamma_{SV} + \Delta A_{SS}\gamma_{SS} + \Delta A_{SL}\gamma_{SL} + \Delta A_{LV}\gamma_{LV} \quad \ldots\ldots\ldots\ldots\ldots\ldots \quad 2.1$$

where: ΔA_{SV}, ΔA_{SS}, ΔA_{SL} and ΔA_{LV} are changes that occurs in the different interfacial free energy and γ_{SV}, γ_{SS}, γ_{SL} and γ_{LV} are the corresponding changes in interfacial energies, with the subscripts being solid, liquid and vapour. If the solid wetting is good, then ΔA_{SV} and ΔA_{SS} are negligible (Jaydeep, 2014). In addition, this results in little to no grain growth and ΔA_{SL} therefore becomes negligible. The $\Delta A_{LV}\gamma_{LV}$ becomes an imperative component of the driving force for liquid phase sintering.

2.4. Spark Plasma Sintering (SPS)

The SPS process uses a low voltage, high density pulse current and applied pressure (Siwak *et al*., 2017). The SPS sintering technique is faster than the conventional sintering techniques that take longer to complete. There are more advantages of using SPS compared to the conventional way of sintering. In SPS, sintering time is reduced due to small holding time at the sintering temperature, which slows grain growth. Other advantages include its ability to enhance diffusion (sintering) kinetics, clean interfaces and good grain-to-grain bonding with dense compacts of potentially >99% of its theoretical density (Siwak *et al*., 2017). Also, samples are sintered uniformly, therefore all the regions in the samples have uniform properties. The compaction and sintering stages are combined in one operation. However, sintering in SPS only allows symmetrical shapes to be prepared, and the pulsed DC generator is expensive (Siwak *et al*., 2017).

The SPS furnace makes use of pulsed electric currents with fast heating and application of pressure for a desired density in a short period (Mam, 2002). The SPS furnace set-up is shown in Figure 2.4 (Mam, 2002). The mixed powders are loaded directly into the graphite dies and are sintered in a vacuum or argon environment (Mam, 2002). The process begins by applying pulsed current discharge, achieved by a voltage of about 30 V and a current of 600-1000 A (Mam, 2002). The period of an individual pulse may be varied from 1 to 300 ms.

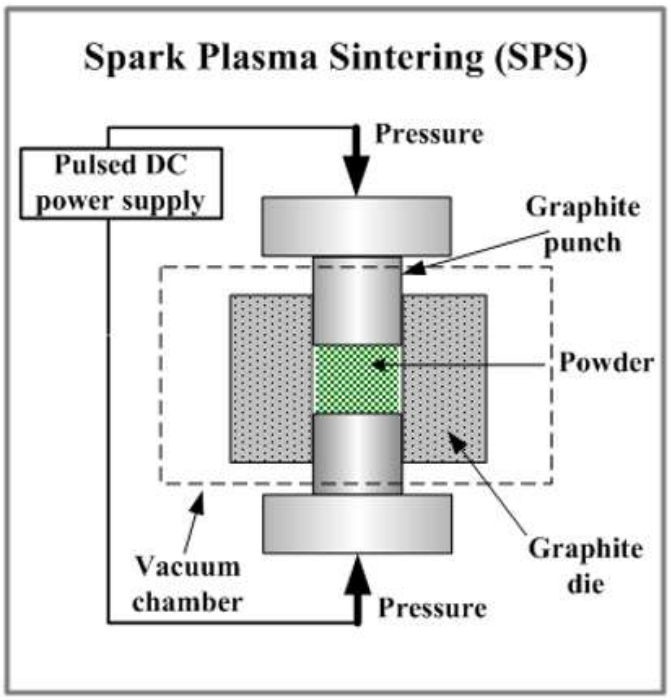

Figure 2.4 Schematic diagram showing spark plasma sintering (SPS) during sintering (Mam, 2002).

Normally, for conductive powders, the heating is due to the Joule effect and heat transfer from the graphite dies and punches, which occur as a result of current flowing through paths 1, 2 and 3 indicated in Figure 2.4 (Mam, 2002). Heating of non-conductive powders is by heat transfer from the dies and the punches. The heating of the dies and punches is due to their resistance to current flow.

During spark plasma sintering, the on-off direct current (DC) pulse voltage and current from the pulse generator are applied to the loose powders. The current goes to the path of least resistance, and this is normally through points of contact between particles as shown in Figure 2.5 (Mam, 2002). This is because there is generally an electrical potential difference between two contacting particles, thus the local current will flow from the higher electrical potential particle to the lower electrical potential particle (Mam, 2002).

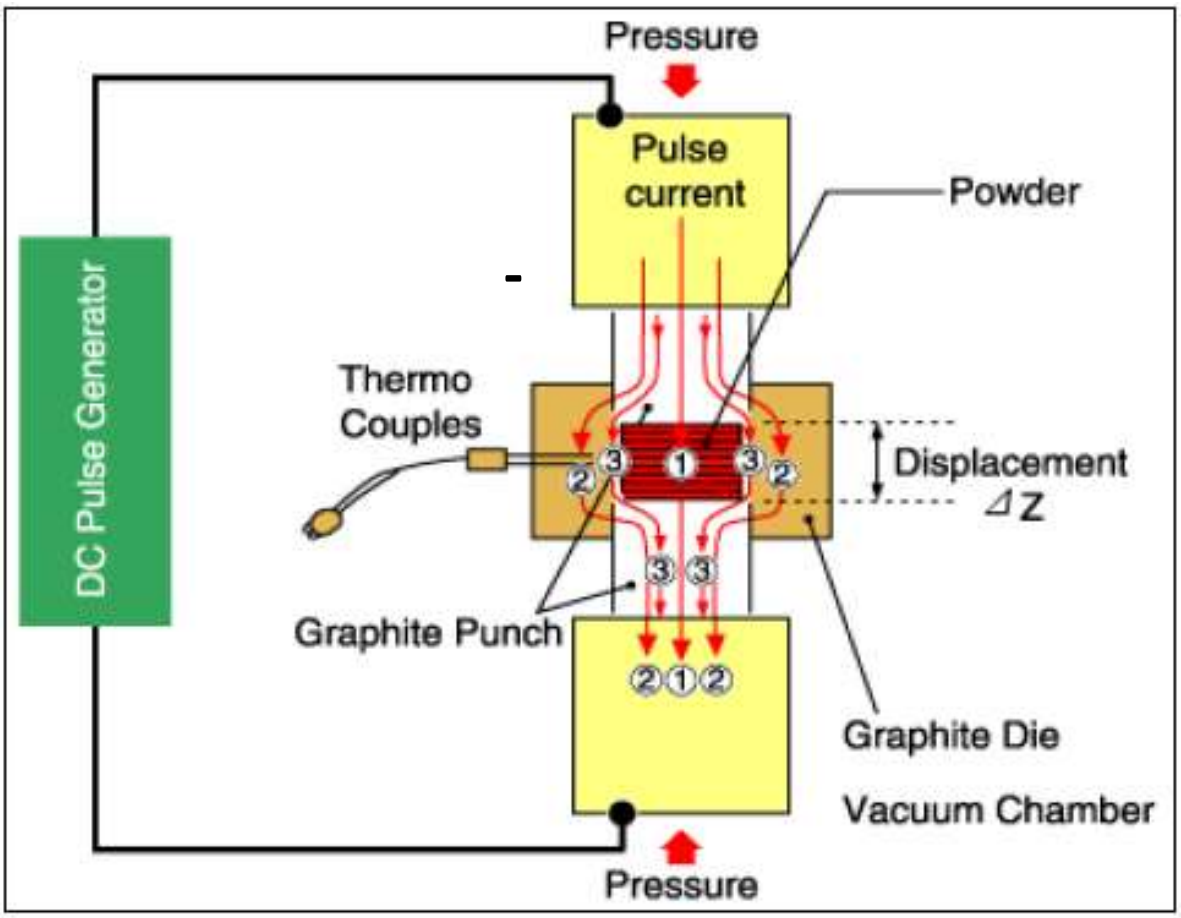

Figure 2.5 Diagram showing the flow of pulse electric current in SPS during sintering (Mam, 2002).

2.5. Cobalt binder in WC

Cobalt has two allotropic structures, close-packed hexagonal which is stable at 400°C and a face-centred cubic structure which is stable at higher temperatures (Upadhyaya, 2001). A conversion from the close-packed to the cubic structure depends on the presence of interstitial impurities. Cobalt is the most preferred hardmetal binder, since it has a good wetting of WC, a melting point of 1493°C and can form a liquid phase at the eutectic temperature of 1270°C (Upadhyaya, 2001). This liquid phase sintering produces a fully dense sintered product. The cobalt binder satisfies most of the desired properties of a binder in hardmetals.

2.6. WC-Co background

Hardmetals with a cobalt binder were the first cemented carbides available commercially and consist of fine tungsten particles with metallic cobalt (Upadhyaya, 2001; Chabretou *et al*., 2003). WC-Co has superior abrasive wear resistance compared to steel and has many applications in machining (Upadhyaya, 2001).

Chabretou *et al*. (2003) undertook quantitative analysis of the effect binder phase composition has on grain growth in WC-Co sintered materials. In their study, six ternary alloys were investigated, with compositions in Table 2.1. The four alloys (1), (2), (1S) and (2S) were in two-phase field {WC + liq}, while (1) and (1S) were along the ternary line WC-$Co_{0.99}C_{0,01}$, alloy (2) and (2S) were along the ternary line WC-$Co_{0.94}W_{0,06}$. The cobalt content was 35 wt% in compositions (1), (2) and 8 wt% in compositions (1S) and (2S). The compositions (3) and (4) were in three-phase domains {WC + liq +C} and {WC + liq + η}.

Table 2.1 Compositions of the samples, in at.%, Co balance (Chabretou *et al.*, 2003).

	C	W	V	Cr
(1)	25.5	25	0	0
(1)V	26.5	25	1.5	0
(2)	25	28	0	0
(2)V	25	28	1.5	0
(3)	30	20	0	0
(3)V	30	20	1.8	0
(3)Cr	30	20	0	1.8
(4)	20	30	0	0
(4)V	20	30	1.8	0
(4)Cr	20	30	0	1.8
(1S)	43.35	43.25	0	0
(1S)V	43.35	42.95	0.4	0
(2S)	42.85	43.65	0	0
(2S)V	42.95	43.25	0.4	0

Eight quaternary alloys, with V and Cr additions (Table 2.1) were prepared and investigated with their compositions corresponding to a 3 at% Co content substituted by the inhibitors in the ternary binders. A starting material with WC powders of median sizes 5.5, 1.7 and 0.9 µm,

and a maximum size of 50, 12 and 8 µm. Samples were compacted at a 600MPa, heat treated at 900°C for 1 hour then at 1450 °C. Figure 2.6 illustrates the equilibrium phases and the alloy compositions used.

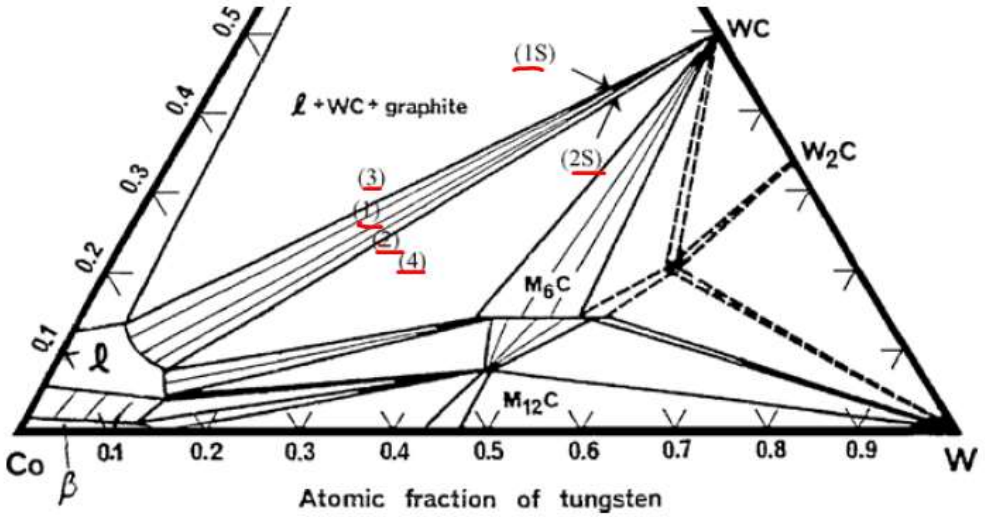

Figure 2.6 Compositions of the studied ternary alloys reported on the W-C-Co isothermal section at 1425◦C (Chabretou *et al.*, 2003).

Chabretou *et al.* (2003) noticed the driving force for grain growth in Co based liquid was the reduction of WC/liquid interface area. As the initial WC grains gets smaller, the larger the interface area and the larger the driving force. Their results showed a contribution of the C/W ratio in the binder phase was the starting mean intercept and the mean intercept variation were smaller in ternary alloys with lower C/W ratio, or materials with inhibitors. This quantitative analysis can be explained by the enhancement of grain growth during heating and during isothermal holding as the carbon content increases.

To achieve maximum possible hardness, tungsten carbide grains must be fine, possibly smaller than 0.8 µm (Figure 2.7 (Upadhyaya, 2001)). The lower the cobalt content in tungsten carbide - cobalt, the greater the hardness and abrasive resistance, provided that enough cobalt is present for liquid-phase sintering to be successful. The cobalt content must range from 2-3 wt% in tungsten carbide for maximum hardness, with 3 wt% Co being the minimum

for commercial use (Upadhyaya, 2001). Increasing cobalt content and grain size in carbides results in less abrasion-resistance grades.

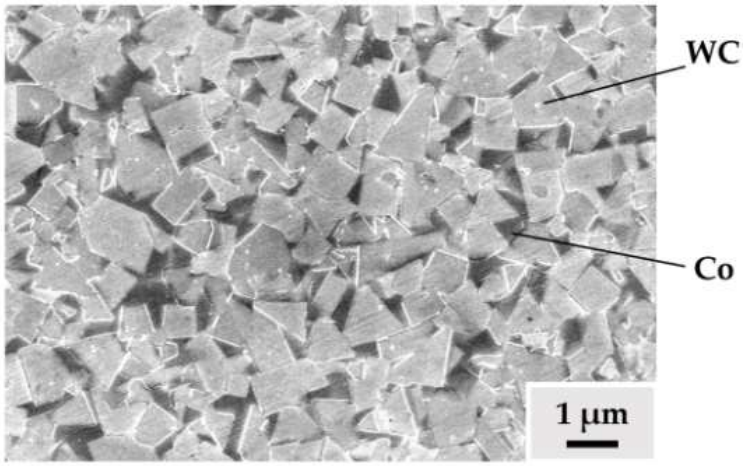

Figure 2.7 Micrograph of WC-Co cemented carbide with an average WC grain size of 0.68 µm (Upadhyaya, 2001).

Although the WC-Co composition ranges from about 2-3 wt% cobalt for metal cutting tools (Brookes, 1975), for press tools and highly abrasive wear environments, the cobalt content can be increased to below 30 wt% with carbide grains of a maximum of 20 µm (Upadhyaya, 2001). High strength hardmetals, combining sub-micrometre carbide grains with relatively high cobalt contents have found increasing use in machining metals at low and medium speeds and high feed rates. An earlier use was in routers and similar high-speed woodworking cutters needing especially sharp cutting edges.

2.7. Porosity and segregation

Porosity is the open space between grains in a microstructure. Porous materials can absorb fluids or moisture, which can cause corrosion. In general, almost all materials have some level of porosity (Owais, 2013). Porosity can cause stress concentrations which can ultimately result in failure of materials. Pores can be defined as an entrapped gas that creates voids in a sample. The total volume of these voids is termed porosity (Owais, 2013). The pores can negatively affect the mechanical properties of the material above the critical pore volume, which can vary for different materials and applications. Figure 2.8 a) shows the one type of

the porosity that was measured with a use of a light microscopy while b) shows the micro pores on a fractured surface (Owais, 2013).

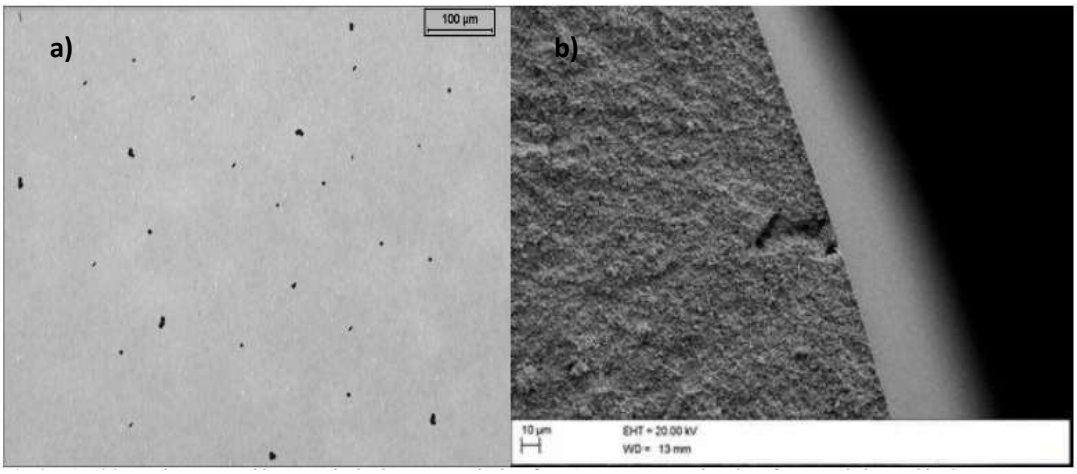

Figure 2.8 SEM micrographs of a) porosity B06 type measured with a light microscopy and b) Micro pores as small back dots (Owais, 2013).

In cemented carbides, the porosity can be measured by a light microscope and a built-in algorithm function. The total area of pores is calculated and rated according to ASTM C 29/C 29M-97 (Montes *et al*., 2005).

Pores that are less than 10 µm in size are classified as A type porosity, and are scaled from A00, A02, A04, A06 to A08 (Figure 2.9, Owais, 2013). Porosity of A00 refers to a material with no porosity, while A02 means the material has 0.02% porosity less than 10 µm in diameter of the total material volume (Owais, 2013).

Voids that have a diameter between 10-25 µm are referred to as B type porosity. Type B pores are scaled from B00, B02, B04, B06 to B08 similar to "type A" porosity (Roebuck *et al*., 1999). The C type "porosity" refers to excess carbon in the material (Figure 2.8). There is usually a trace of excess carbon after sintering, and where carbon causes graphite precipitation. The C type porosity is a measure of free carbon scaled from C00-C08 with C00 referring to no free carbon (Owais, 2013).

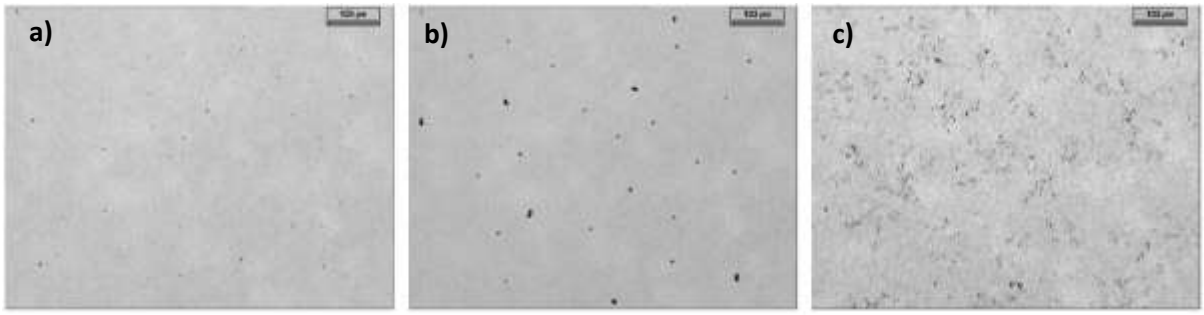

Figure 2.9 Light microscope micrographs showing a) A06 porosity b) B06 type porosity and c) C06 carbon porosity (Owais, 2013).

2.8. Phase relations in WC-Co

The understanding of phase diagrams of cemented carbides is important for predicting the phases after the sintering stage and to ensure an adequate sintering temperature (Fernandes *et al*., 2011). The relevant region of phase diagram of WC-Co cemented carbides is the two-phase region between the hard matrix and the binder phase (Figure 2.10). The optimum properties in WC-Co system are within this two-phase region (Fernandes *et al*., 2011).

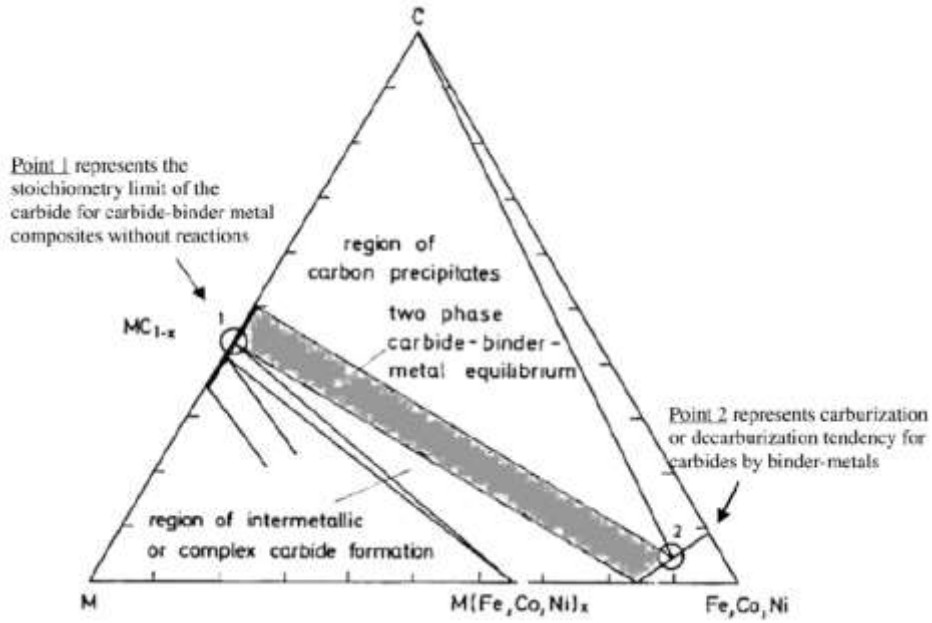

Figure 2.10 Schematic diagram of the cemented carbide phase equilibrium (Fernandes *et al*., 2011).

There have been many studies of the W-C-Co phase diagram over the years, and these include the study done by Wyman and Kelley (1931). The work on W-C-Co done by Takeda (1936), with a tentative W-C-Co diagram considered both stable and metastable equilibria. Later, the equilibrium phase diagram of the W-C-Co system was modified by Rautela and Norton (1952) using X-ray diffraction, metallographic and thermal analysis techniques, where they proposed two phases θ and κ, having compositions $Co_3W_6C_2$ and $Co_3W_{10}C_4$. The challenge with the proposed diagram was that it could not explain the presence of η-phase in cemented carbides after a rapid cooling, even at relatively high carbon contents (Upadhyaya, 2001; Fernandes *et al*., 2011). Pollok and Stadenlmaier (1970) calculated an isothermal section of the W-C-Co system at 1400°C (Figure 2.11), that represented a normal sintering temperature. They found eta-carbides of compositions Co_2W_4 and CoW_3C that were reported by Rautala and Norton (1952) as θ and κ. From this isothermal section the WC is in stable equilibrium with liquid cobalt only within a narrow region of composition (Fernandes *et al*., 2011). Gruter (1959) proposed that the η-phase remains in equilibrium from 1280°C to 1450°C (Figure 2.12).

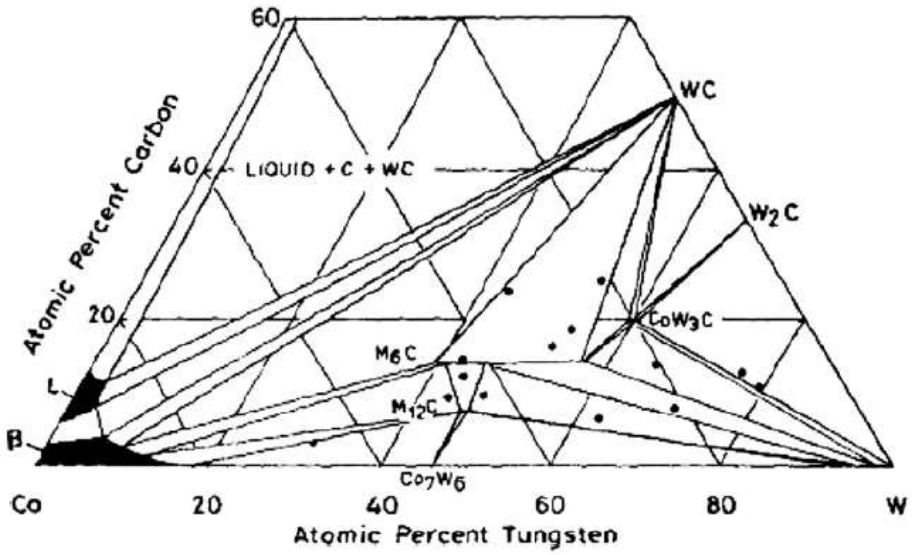

Figure 2.11 Isothermal section of the W-C-Co phase diagram at 1400°C by Pollok and Stadelmaier (1970).

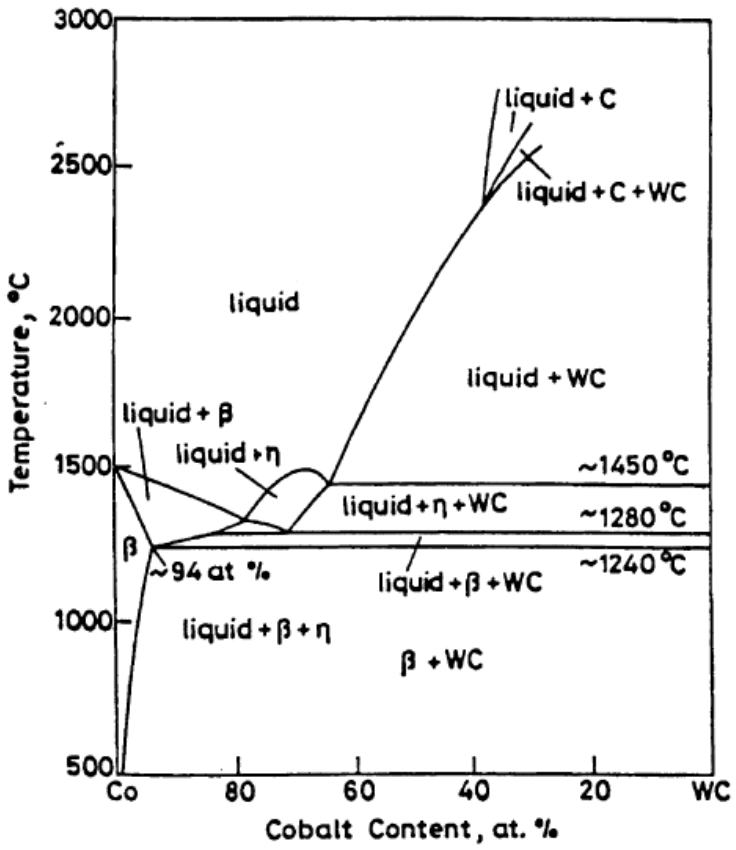

Figure 2.12 Vertical section of the phase diagram of W-C-Co by Gruter (1959).

The extensive study of thermodynamics and the W-C-Co phase relationships done by Guillermet (1987) shows a reduction in solid solution on cooling and precipitation on carbide grains. However, experiences and traditions are strong tools in cemented carbide production since they can produce quality materials with little understanding of phase diagrams. Generally, this is common in W-C-Co systems since it is a simple system for cemented carbides, with a eutectic temperature of 1280°C which is well below cobalt's melting point of 1490°C. Guillermet (1987) derived the W-C-Co phase diagram and the WC-Co vertical section for 10 wt% Co (Figure 2.13), to show what happens at each temperature during cooling.

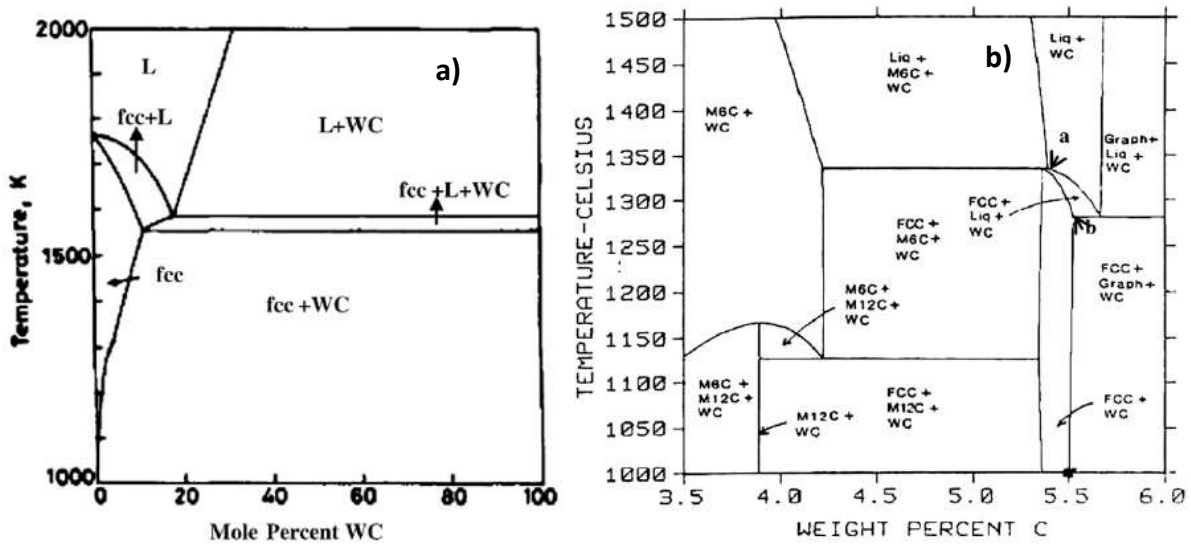

Figure 2.13 Vertical sections of W-C-Co: a) between stochiometric WC and Co and b) WC-Co with a binder of 10 wt% (Guillerment, 1987).

Assuming there is no segregation (Figure 2.13b), the symbols 'a' and 'b' represent the minimum and maximum of the carbon contents after solidification of the fcc + WC mixture. Since the M_6C phase is unstable and has a low dissolution rate, points 'a' and 'b' act as limits to the region of favourable carbon contents, in the absence of graphite or M_6C for mixtures sintered in non-equilibrium conditions (Fernandes *et al*., 2011). Thus, no precipitation of graphite can take place during solidification of pure WC and Co (Figure 2.13). However, adding an excess of 0.05 wt% C can result in graphite precipitation during cooling. Guillermet (1987) studied how the Co content was affected in the critical carbon range. He found that the addition of Co between 6-10 wt% induced an increase of approximately 70% of carbon in the range of the high carbon contents (Fernandes *et al*., 2011). A reported four-phase equilibria (Markström, 2005) with the liquid phase in the W-C-Co system showed a high solubility of WC in Co (Guillermet, 1987). The solubility of W at ambient temperature is 3.5 wt% in the Co binder. The solubility of Co in W is insignificant and can be neglected. At high temperatures, the solid solution of carbon in Co binder for WC-Co is in the range 0-0.2 wt%, with higher values at the lower tungsten levels (Fernandes *et al*., 2011). The solid solubilities of tungsten and carbon in cobalt have an inversely proportional relationship.

Calculated equilibrium phase diagrams are graphical representations of chemical composition systems showing the region of material and stability under different conditions of temperature and composition (Figure 2.14). CALculation of PHAse Diagrams (CALPHAD) is a useful computer simulation which incorporates thermodynamic calculations to estimate the multicomponent phase behaviour, a method introduced by Larry Kaufman in 1960. Thermodynamic properties can be described through the concept of Gibbs free energy.

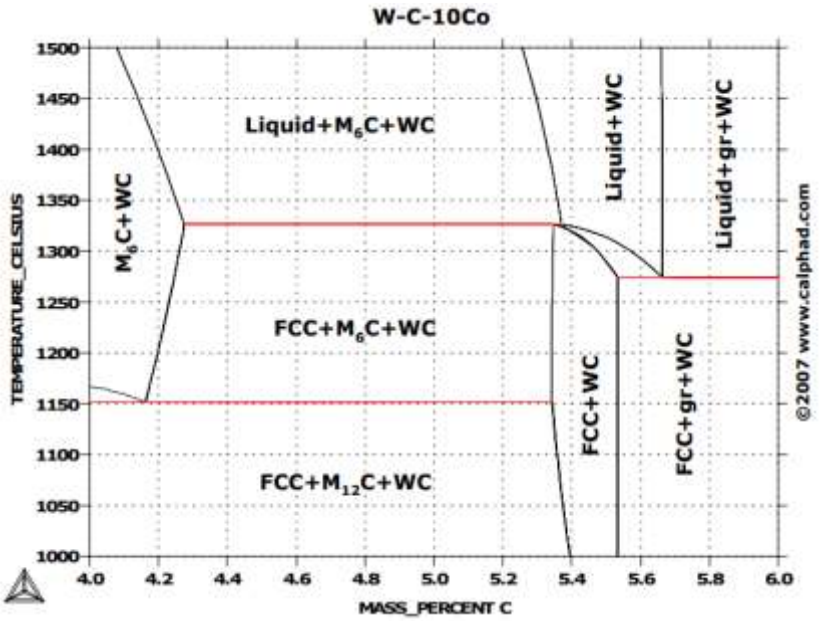

Figure 2.14 Phase diagram of W-Co-C calculated using CALPHAD computer simulation (Garcia *et al*., 2019).

2.9. Eta (η)-Phase

Eta-phase is a substoichiometric ternary carbide comprising W, Co and C which occurs when there is an insufficient carbon in WC-Co system (Garcia *et al*., 2019). Eta (η)-phase is also described as M_6C and $M_{12}C$ (Garcia *et al*., 2019). The $M_{12}C$ has a composition of Co_6W_6C and is stable above 1000°C, while the composition M_6C ranges from $Co_{3.2}W_{2.8}C$ to Co_2W_4C and is stable at lower temperatures (Garcia *et al*., 2019). The $M_{12}C$ and M_6C phases both have cubic structures but can be differentiated by XRD analysis. At lower temperatures M_6C remains a metastable phase and can undergo an *in situ* decomposition (M_6C➔ binder + $M_{12}C$ + WC) by

a sluggish reaction (Garcia *et al*., 2019). The formation of M_6C is likely to occur than $M_{12}C$ in commercial tungsten carbide alloys with a fast-cooling rate (Garcia *et al*., 2019). The amount and shape of η-phase in cemented carbide alloys is mainly stimulated by insufficient amounts of carbon in the system and the low cooling rate (Garcia *et al*., 2019). The η-phase can completely disappear during cooling for extremely low carbon deficiency. At higher carbon deficiency levels, η-phase is produced upon cooling from the sintering temperature (i.e., WC + liquid ➔ WC + η-phase + liquid) and nucleates at grain boundaries (Garcia *et al*., 2019).

Additional cooling into the solidus range might yield a peritectic decomposition of the η-phase (liquid + η + WC ➔ WC + binder) (Garcia *et al*., 2019). Although the decomposition of the η-phase is thermodynamically possible, from low to high carbon contents, the process is slow and therefore η-phase may remain after cooling. Furthermore, due to massive dendritic η-phase regions being formed across the material, this type of η-phase is particularly detrimental. Therefore, these low carbon contents are to be avoided in cemented carbide production, since the existence of large areas of brittle η-phase greatly diminishes the mechanical properties of the cemented carbide. With higher carbon deficiency levels, η-phase is present at the sintering temperature and tends to be retained after cooling. The finely dispersed particles of η-phase increase both in particle size and in volume fraction with an increase in carbon deficiency (Figure. 2.15, Garcia *et al*., 2019).

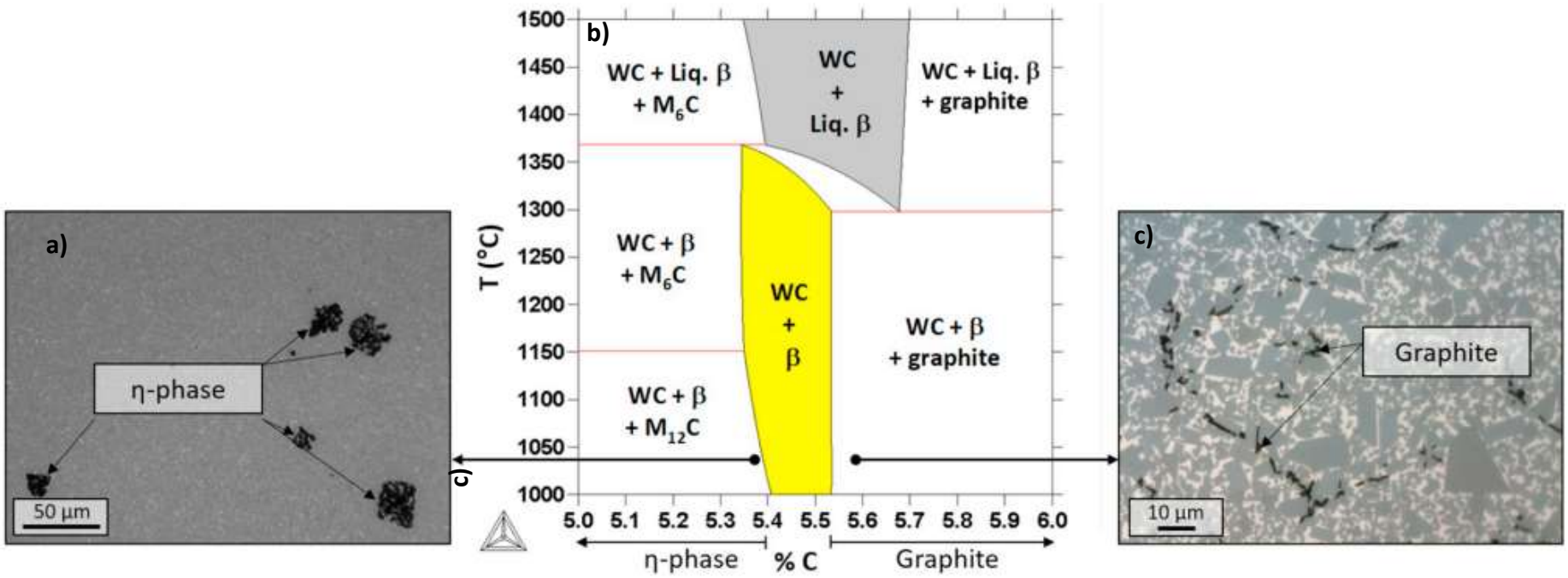

Figure 2.15 a) Micrograph showing η-phase, b) phase diagram showing the possible phases, and c) graphite formation in a WC-10%Co cemented carbide. (Garcia *et al.*, 2019).

2.10. Importance of additives on cemented carbides

Cemented carbides are undoubtably one of the strongest materials for industrial use, especially in mining and for cutting tools (Huang *et al*., 2007, Siwak *et al*., 2016). The use of SPS during cemented carbide production improves their mechanical properties even more compared to the conventional way of sintering. The challenge is implementing the process on a larger scale, as SPS has its own disadvantages which include the capital cost, only symmetrical shapes may be prepared, and it can only produce small component sizes. The hardness, strength and wear resistance of WC-Co cemented carbides can also be improved by decreasing the WC grain size to nanometre scale, but this does not stop grain growth. Therefore, the most successful way of controlling WC grain growth is the addition of a small amount of WC grain growth inhibitors, typically <1.0 wt% of metallic carbides to the starting powder mixture (Huang *et al*., 2007). However, other additives such as Cr_3C_2 and nickel can improve corrosion resistance and toughness without adversely affecting the hardness significantly

Generally, the minimisation of interfacial energy in cemented carbide is one of the driving forces for densification and grain growth during cemented carbide sintering. Due to the high level of disorder interfaces in ultrafine and nanocrystalline materials, the driving force for grain growth is profound, in a sense that a sample with an average grain size of about 10 nm can comprise 30 vol.% grain boundaries and interfaces (Farag *et al.,* 2018). It is common that grain growth modes vary depending on the temperature intervals corresponding to specific values of atomic mobility. This is common at temperatures close to the eutectic temperature of the material system (Farag *et al.,* 2018). Grain growth modes in WC-Co are largely influenced by four modes that are instrumental in WC-Co coarsening which includes: discontinuous grain growth, layer-by layer growth, continuous grain growth and coalescence of grains.

Ostwald (1967) theory and equation has over the years intensively described the continuous grain growth behaviour of precipitates in dilute solutions where small grains dissolve, using his famous empirical equations. Grain growth development during isothermal hold in cemented carbide in usually described by Equations 2.2 and 2.3 where G_0 = initial grain size,

K_0 = growth constant, n = grain growth exponent, T = temperature and R ideal gas constant (Farag *et al.,* 2018).

$$G^n - G_0^n = K\,(t - t_0) \quad \text{.....2.2}$$

$$K = k_0 e^{-Q/RT} \quad \text{.....2.3}$$

Figure 2.16 (a) and (b) (Farag *et al*., 2018) show the continuous grain growth at different sintering times, which ultimately changes the mean tungsten carbide grain size when applying Equation 2.2. When WC is sintered, facetted WC crystals with atomically smooth surfaces form in the hardmetal microstructure.

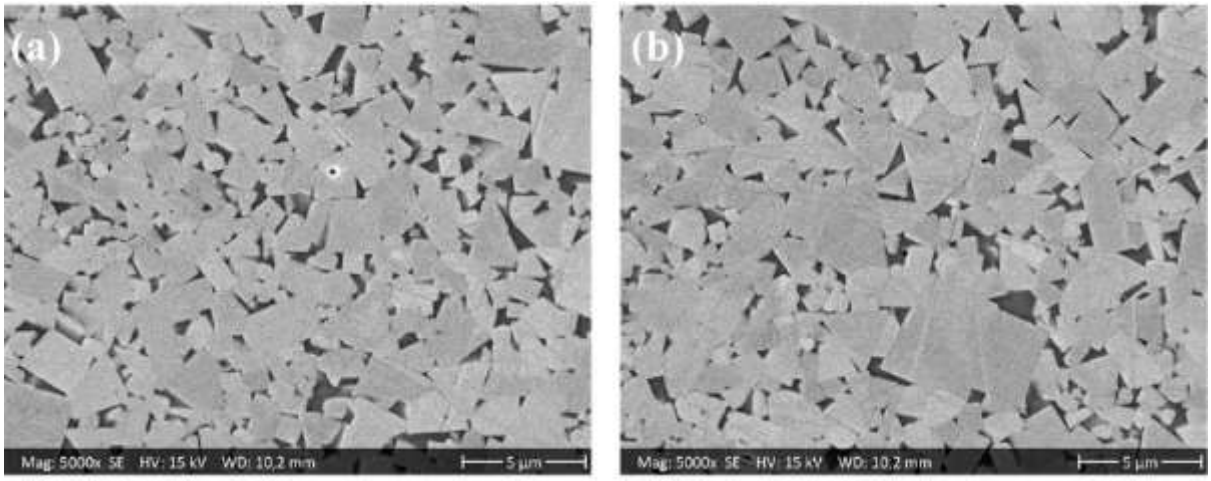

Figure 2.16 Microstructure of a WC-6wt.-%Co composite of a liquid phase sintered at 1400 °C (a) for 30 min and (b) for 240 min (Farag *et al.,* 2018).

Composites such as VC-Co, Fe-Cu or Mo_2C-Co usually form spherical and atomically rough interfaces which are preferable to atomically smooth surfaces that are usually formed in hardmetals due to tungsten or carbon atoms and their ability to form surface energy (Farag *et al.,* 2018). This results in low WC grain growth rates for hardmetals compared to other composite systems like VC-Co and Fe-Cu. The exponent n = 2 in Equation 2.2 thus denotes the interface-controlled growth rate of such faceted grains while n = 3 for diffusion-controlled systems.

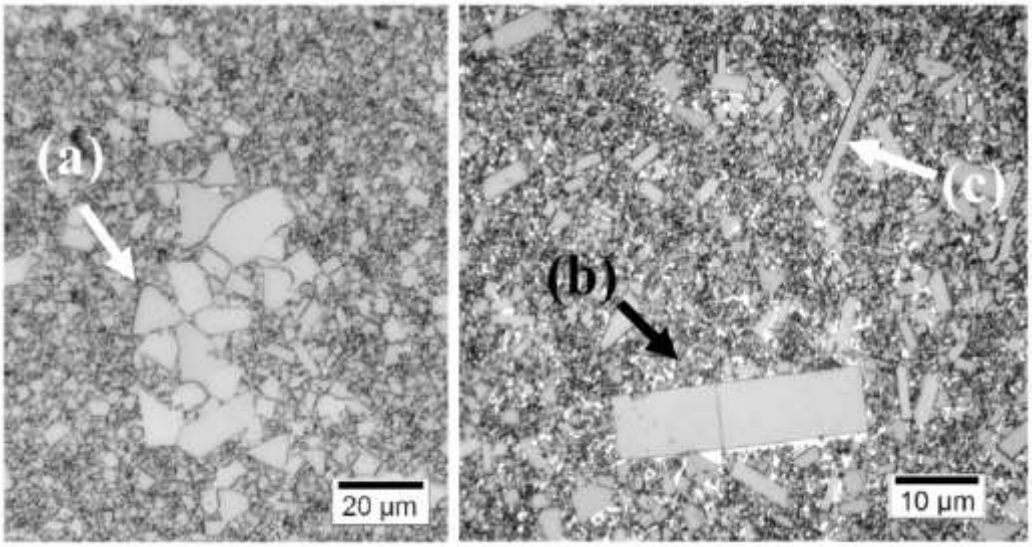

Figure 2.17 Micrographs of different DGG types. (a) WC-6wt%Co: Isotropic DGG through coarse grain contamination, (b) Isotropic DGG with an aspect ratio of approx. 4, (c) Anisotropic DGG with a high aspect ratio of approx. 10 in a WC-10wt%Co material (Farag *et al.,* 2018).

A different type of grain growth known as discontinuous grain growth (DGG), which exhibits as abnormal grain at the surface of carbide samples appears as nest-like clusters of grains that are larger than the average grain size (Figure 2.17). It is therefore believed that there is some correlation between the structure of the grain surface and abnormal grain growth (Cho *et al.,* 2004). Tungsten carbide grains can undergo a surface roughening transition if sintered at high temperatures or at low carbon contents.

In Figure 2.17 there is a distinctive difference between isotropic (a and b) and anisotropic grain growth (c). In both images there are large WC grains that appear in the microstructure, resulting in a bimodal grain size distribution, and large grains might lead to plate-like shapes with a high aspect ratio (Farag *et al.,* 2018). Abnormal and isotropic large grains usually are a result of coarse WC grains in the initial WC-Co powder, and anisotropic growth grains results from a defect in grain growth.

Research by Sommer *et al.* (2002) shows that such plate-like grains are formed before the formation of liquid phase and always consist of growth twins. Grain boundaries that are between grain twins are there to control the attachment and aggregation of new atoms onto WC grain surface. This therefore means that even fine grains can act as nuclei for abnormal grain growth (Farag *et al.,* 2018). In addition, this growth mode is prevalently encountered

with decreasing average grain size and effectively diminishes when the average grain exceeds a certain value, even if the grains are faceted.

Discontinuous grain growth can be triggered by physical or chemical irregularities within the green body in cemented carbides (Farag *et al.,* 2018). Physical irregularities such as high variance in the powder grain size, agglomerates of WC grains and other impurities that are picked up during manufacturing, incomplete powder milling, or the granulation process exacerbate grain growth. Chemical inhomogeneities are challenging to control due to their strong influence on the microchemistry of the green body during the liquid phase sintering process (Farag *et al.,* 2018). The excess of carbon has a significant influence on the grain growth of the surrounding grains, which results in the formation of isotopically large abnormal grains. An excess of W may lead to formation of η phase (Co_6W_6C or Co_3W_3C) which can cause twinning during recarburisation ($Co_3W_3+2C \rightarrow 3Co+3WC$) (Farag *et al.,* 2018).

The coalescence of grains in Figure 2.17 shows the aggregation of grains by migration and dissolving of particles in grain boundaries (Wang *et al*., 2008). For the grains to achieve this phenomenon, the crystal lattices of neighbouring grains must coincide, which can be done by grain rotations or by shifting the neighbouring grains. Therefore, the energetic barrier for coalescence is a function of the grain volume. Also, coalescence does not require long diffusion distances. It is, however, difficult to spot coalescence in cemented carbide microstructures; Figure2.18 shows a scarce microstructure of coalescence by Wang *et al*. (2008). More direct evidence of coalescence of WC grains was discovered by Kumar *et al*. (2006) where he demonstrated that certain low energy boundaries denoted by Σ2 coincidence site lattice boundaries, diminish during the sintering process due to their high mobility and even correlated the disappearance of such boundaries with the change in grain size.

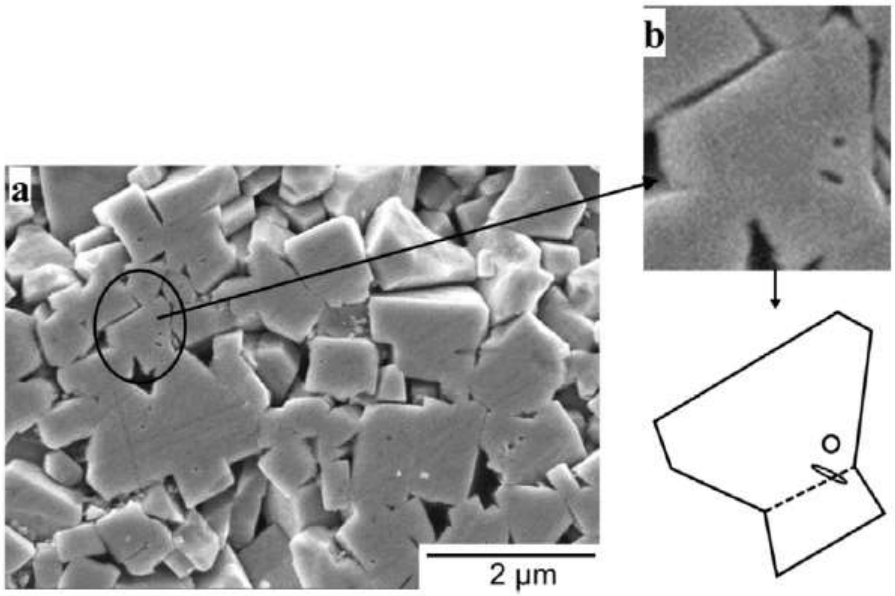

Figure 2.18 Illustration of coalescence of WC grains. (a) SEM image of a WC-10Co powder sintered at 1400°C. (b) Magnified SEM image of coalescent grain. The dashed line illustrates the eliminated grain boundary (Wang *et al*., 2008).

Wang *et al.* (2008) found that the cobalt phase can facilitate grain growth even at temperatures under the eutectic point. Wang *et al.* (2008) associated this phenomenon with an enhanced mass transport of W/C through the solid binder and discussed models of coalescence enhanced by solution/reprecipitation through Co thin films. It is important to note that the diffusion coefficient of W in solid Co at 1200°C is estimated at 3 x 10^{-15} m^2/s which is six orders of magnitude lower than that in the liquid Co-phase at 2 to 4 x 10^{-9} m^2/s at 1450°C (Allibert *et al.,* 2000; Lavergne *et al*., 2002). It is, however, difficult to believe that the observed disparity in the grain growth rates between binderless WC and WC-10wt%Co, especially in the solid phase, can be attributed solely to mass transport through the binder. Although WC grains are covered by thin films of Co during the powder milling process, it is unclear what happens to the Co film during coalescence. A possible reason might be that Co layers trapped within coalesced WC grains diffuse out of the coalescing boundaries (Farag *et al.,* 2018).

Another important grain growth type that affects cemented carbide is a layer-by-layer grain growth. A study by Zhong and Shaw (2011) in Figure 2.19 shows that WC grains can develop a stepped morphology at high sintering temperatures and they linked these observations to a 2D nucleation growth mechanism.

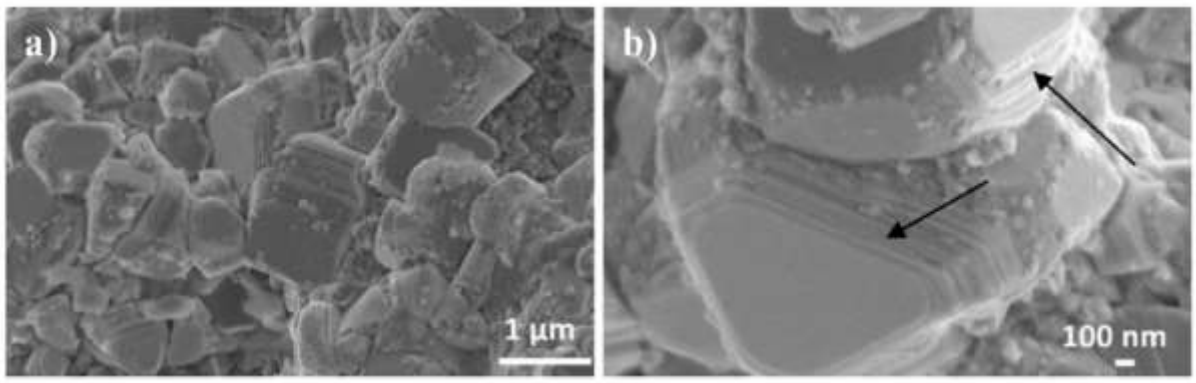

Figure 2.19 SEM images of WC-Co powder sintered at 1400°C for 2 h. (a) Overview of the sintered WC-Co powder. (b) Layered morphology of a WC grain (Zhong and Shaw, 2011).

Froschauer and Fulrath (1976) obtained similar results, but interestingly, rather for a WC-10wt%Co grade than WC-15wt%Co composite, however, no association to a new growth mode was made. As highlighted before, a huge energy barrier must be overcome for 2D nucleation to manifest on an atomically flat surface. At under-eutectic temperatures, only a small number of grains can fulfil the critical conditions to form seeds or ''islands'' triggering DGG. At elevated temperatures, such islands nucleate more easily and frequently.

2.11. Vanadium carbide as an additive

Vanadium carbide (VC) is normally added to cemented carbides in amounts not greater than 1 wt% and only as a grain growth inhibitor (Kieffer, 1960). However, during World War 2, vanadium carbide and nickel (VC-Ni) was developed in Germany and used in machining, because Germany was not allowed to import tungsten (Kieffer, 1960).

Not long after 1945, VC-Ni was replaced in Germany by the traditional WC-Co. The reason was both Co and Ni wet WC better than they do VC, and that WC is more soluble in Co and Ni than VC (Luyckx *et al*., 2001). When wetting is good, this leads to more shrinkage during sintering and less porosity in the final material (Morteza *et al*., 2013). Better solubility of vanadium in WC-Co leads to more compact carbide structures in the final material, through

dissolution and re-precipitation of the carbides during sintering (Pirso *et al*., 2014). During LPS, Nan *et al.* (2012) found that the dissolution of VC supresses the solution-precipitation of WC and reducing grain growth of WC particles during sintering. The non-uniformity of the additives results in a non-homogeneous distribution of WC solubility in the binder phase, and this causes the abnormal grain growth and subsequently results in non-uniform distribution of WC grain size in the microstructure of WC-Co. Generally, Cr_3C_2 and VC additives are the most effective grain growth inhibitors, and there is an increase in hardness when small additions of VC are introduced as shown in Table 2.2.

Table 2.2 Mechanical properties of WC-10wt%Co alloys sintered in HIP (Nan *et al*., 2012).

Properties	Density ($g\ cm^{-3}$)	Average grain size (nm)	Rockwell A hardness	Vickers hardness (MPa)
WC–10Co	14.44	950	91.8	1580
WC–0.4VC–10Co	14.20	380	93.5	1840
WC–0.8VC–10Co	14.16	330	93.7	1870
WC–0.4VC–0.4 Cr_3C_2–10Co	14.28	430	92.7	1670
WC–0.4VC–0.4 Cr_3C_2–10Co	14.32	400	92.1	–

A fine microstructure with a homogeneous grain size distribution is usually desired in WC–Co composites (Hyoung and Deug, 2003). Particularly, the presence of a few grains substantially larger than the average due to abnormal grain growth (AGG) is detrimental. To avoid AGG, other metal carbides such as TiC, TaC, NbC, and VC are added as a grain growth inhibitor (Choi *et al*., 2000). Abnormal grain growth during liquid-phase sintering occurs only when the grains are angular or faceted (Choi *et al*., 2000). When the grains are faceted, the solid–liquid interface structure is atomically smooth. This creates an increase of chemical potential. Consequently, ledge-generating sources such as two-dimensional (2-D) nucleation is necessary, which needs a driving force larger than a certain critical value (Hyoung and Deug, 2003). As a result, only a few large grains with enough driving force can grow. This process has been suggested as the mechanism of AGG (Choi *et al*., 2000). The role of VC as a grain growth inhibitor in WC–Co composites is being interpreted in view of the 2-D nucleation controlled coarsening process. The addition of VC effectively retards the coarsening process of WC grains but AGG still appeared after a prolonged heat treatment in samples that were

consolidated using traditional sintering methods other than SPS. It was predicted that the VC addition increases the energy barrier for 2-D nucleation by raising the edge energy (Choi *et al*., 2000). For the coarsening process controlled by the 2-D nucleation, the edge energy, ε, which produces the free energy change accompanying the formation of a ledge is a critical parameter. Although the change in edge energy is hard to determine quantitatively, it can be estimated qualitatively from the grain shape. The edge energy value is inversely proportional to the number of corners or faces of the equilibrium crystal. Therefore, the edge energy of spherical grains having infinite corners or faces is zero. Lee and Kim (2003) determined the role of VC during the sintering of WC–Co composite and to elucidate the mechanism of grain growth inhibition by observing the shape of WC grains where they concluded that when a small amount of VC is added to WC-Co, the coarsening rate of WC grains was reduced significantly and that the shape of WC grains in WC-Co specimens were truncated triangular prisms.

If the coarsening of angular WC grains with an atomically smooth interface structure occurs by 2-D nucleation and subsequent lateral growth of nuclei, the free energy change associated with nucleation is given by Equation 2.4 (Hyoung and Deug, 2003).

$$\Delta G = 2\pi R\varepsilon + h\pi R^2 \Delta G_v \quad \ldots\ldots\ldots\ldots\ldots\ldots\ldots 2.4$$

where R is the radius of the circular disk-shaped nucleus and h is the step edge height (Hyoung and Deug, 2003). The ε is the step edge free energy, which describes the amount of energy necessary to make a unit length of step edge and ΔG_v is the driving force for coarsening. For a grain of size r, the driving force is expressed by Equation 2.5.

$$\Delta G_v = 2\gamma\ (1/r - 1/r^*) \quad \ldots\ldots\ldots\ldots\ldots\ldots\ldots 2.5$$

where r* is a critical size that is neither dissolving nor growing. From Equation 2.4, the energy barrier for 2-D nucleation is calculated from Equation 2.6 (Hyoung and Deug, 2003).

$$\Delta G^*_{2D} = -\pi\varepsilon 2^2/h\Delta G_v \quad \ldots\ldots\ldots\ldots\ldots\ldots\ldots 2.6$$

Since the nucleation rate is proportional to exp $(-\Delta G^*_{2D}/kT)$, the coarsening rate will remain nearly at zero and increase sharply when ΔG_v exceeds a certain value (Hyoung and Deug, 2003). Therefore, it can be predicted that coarsening is only possible for a few grains that are larger than a certain critical size r_c, i.e., for the grains $r > r_c >> r^*$; AGG will occur under this

situation. Equation 2.4 indicates that a small change in ε may result in a large change in G^*_{2D}, and consequently a notable change in the coarsening process (Hyoung and Deug, 2003). The presence of defects or grain boundaries which lower G^*_{2D} by acting as heterogeneous nucleation sites greatly increased the coarsening rate (Lee *et al.*, 2002). The overall retardation of WC grain growth by VC addition has been shown to be the result of an increase in edge energy. Thus, Understanding the driving force of WC-Co with VC addition is not enough, it is therefore imperative to introduce the C-V binary phase diagram (Figure 2.20) which explicitly shows the formation of vanadium carbide (Hyoung and Deug, 2003).

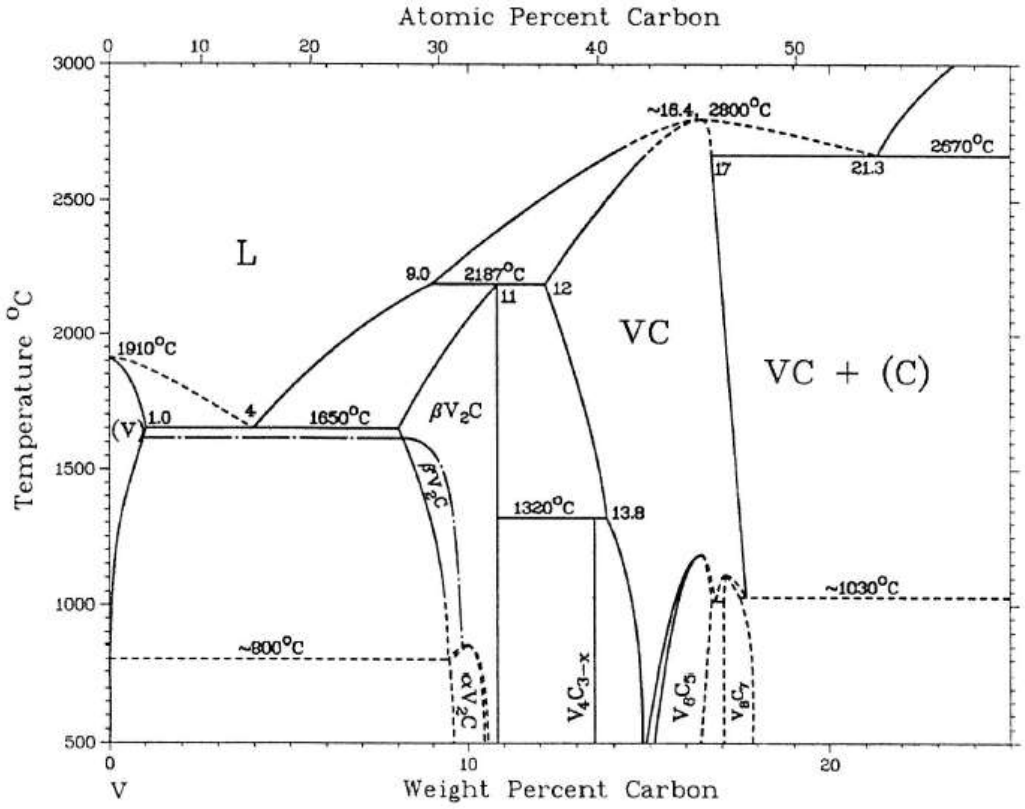

Figure 2.20 C-V binary phase diagram (Hyoung and Deug, 2003).

Vanadium carbide has two eutectic phase reactions, one at 4 wt% C and the other at 21.3 wt% C. Another special point is 2187°C where there is peritectic reaction for the formation of βV_2C by liquid and VC (Hyoung and Deug, 2003). The diagram also shows that a further decrease in temperature at 1320°C results in a peritectoid reaction between VC and βV_2C to forming V_4C_{3-x}. When V_4C_{3-x} is compared to V_2C and VC it can be considered as a line compound because of its near-stoichiometric range. The complex phase relations between

the two phases VC and βV_2C is due to the decrease in temperature which subsequently changes the two-phase fields (Hyoung and Deug, 2003). The formation of V_8C_7 occurs when the temperature decreases from 1100°C to 500°C between 17 and 18 wt% C this show an interesting congruent transformation phase VC at 16.4 wt% C along the same line. Formation of V_8C_5 starts at 1150°C and is linked to the congruent phase at 1100°C between 15 to 16.4 wt% C (Hyoung and Deug, 2003).

The effect of VC on WC-Co has been observed by Whitefield (2011), where the optimisation of WC-VC-Co was done to reduce the grain size of (W, V)C and improve the mechanical properties for a mining application. The samples were sintered using a laboratory type Sinter Hip Furnace (SHF) 6 V at 1390°C or 1410°C. He observed that the hardness of WC-VC-Co materials tended to be higher than a conventional WC-Co material and the toughness was improved (Whitefield, 2011). Also, the use of finer powders (<1 um) prevented the crack propagation and growth in samples with VC. The only failure that was observed was when the VC samples were exposed to silica environments where corrosion and abrasive conditions were experienced. Similar to the work done by Han *et al*. (2009) where WC-15wt%Co samples with and without VC were tested in three-point bend at 1000°C, it was found that WC-15wt%Co samples underwent a large plastic strain and drifting of Co binder, while samples with VC had restricted movement of Co and had no evidence of grain boundary sliding.

2.12. Chromium carbide as an additive in hardmetals

Chromium carbide (Cr_3C_2) plays an important role in cemented carbides (Luyckx *et al*., 2001). When there is an addition of Cr_3C_2 in cemented carbides, the average WC grain size decreases significantly. An excessive amount of Cr_3C_2 in cemented carbides may result in an increase in the average grain size (Sun *et al*., 2008).

Carbides that result in WC-Co having low mechanical properties can be explained in terms of the coalescence and re-precipitation of undissolved WC at grain boundaries (Luyckx *et al*., 2001; Morteza *et al*., 2013). During sintering, some dissolved atoms re-precipitate onto the undissolved carbide grains, which results in grain growth (Zackrisson *et al.,* 1998; Renqi *et al*., 2017). The mixture of more than one metal carbide in the powder can result in the formation

of a mixed carbide phase, either as homogenous grains or as grains with core-rim structures (Zackrisson *et al*., 1998). Coalescence involves grain boundary migration where grain growth is greater than growth by re-precipitation. A lower eutectic temperature and higher solubility are important for grain refinement in hardmetals binders, Table 2.3 (Upadhyaya, 2001). The Cr_3C_2 and VC additives can be easily dissolved in the cobalt binder at low temperatures, which is why they can successfully prevent WC grain growth.

Table 2.3 Eutectic temperatures for M_x-C_y-Co systems and solubility of the carbides in the cobalt phase (Upadhyaya, 2001).

Inhibitor compound, MC	Eutectic temperature, M_xC_y-Co (°C)	Solubility in Co binder at 1400°C (mol.% M_xC_y)
TiC	1360	1.5
ZrC	1360	6.0
HfC	1370	3.0
VC	**1330**	**10.0**
NbC	1380	6.0
TaC	1370	3.0
Cr_3C_2	**1245**	**12.0**

Figure 2.21 (Zackrisson *et al.,* 1998) shows a calculated phase diagram using system components Co, WC, Cr_3C_2, and C at constant amount of Co (10 wt%). At the sintering temperature, 1420°C, all Cr_3C_2 is dissolved in the liquid phase. During cooling after sintering there is a primary precipitation of M_7C_3 phase from the liquid if the Cr_3C_2 content is within approximately 3.5 to 7 wt%. This is the case for the 12 vol% (6 wt%) Cr_3C_2 material. At higher Cr_3C_2 contents there is a precipitation of the M_3C_2 phase. If the Cr_3C_2 content is lower than 3.5 wt% solid binder will precipitate first, but some M_7C_3 can still be precipitated from the liquid for Cr_3C_2 contents higher than 1 wt% (Zackrisson *et al.,* 1998). This is expected to occur in the 4 and 6 vol.% alloys (1.9 and 2.9 wt%, respectively). When all the binder has solidified there is a driving force for replacing the M_7C_3 phase with the M_3C_2 phase. However, this transformation will be very sluggish due to the coarse areas of M_7C_3 carbide formed due to precipitation from the liquid phase (Zackrisson *et al.,* 1998). The metallic mol fractions of the M_7C_3 phase at the solidus temperature according to the calculations are approximately 0.23 Co, 0.01 W and 0.76 Cr (Zackrisson *et al.,* 1998).

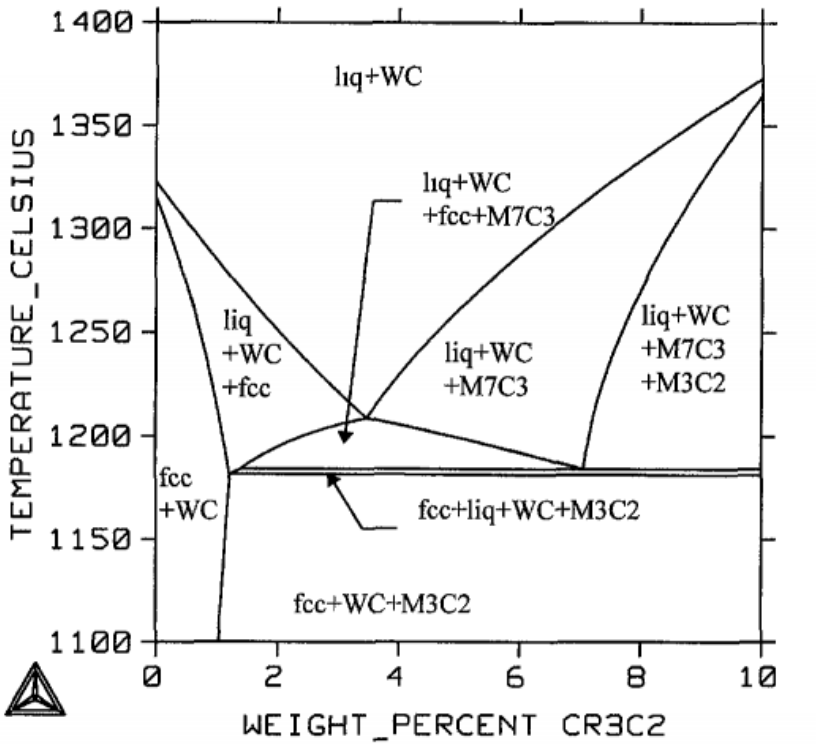

Figure 2.21 A calculated phase diagram using the system components Co, WC, Cr_3C_2, and C at constant amount of Co (10 wt%) and of C (0 wt%) (Zackrisson *et al.,* 1998).

The carbide inhibitors generally have low solubility in WC, and the grains usually do not grow to incorporate those impurity atoms (Zackrisson *et al.,* 1998). For chromium, the WC–Co interfaces have high concentrations or deposits of the inhibitor after sintering. The presence of inhibitors at the WC–Co interface affects the various adsorptions/desorption processes which occur at all WC grain boundaries and interfere with the overall grain growth. In addition, because the presence of the Cr_3C_2 inhibitor at the WC–Co interface prevents the transfer of the binder phase and stops the WC grains from growing, there is increased amounts of the single WC grains, which assures the normal growth of WC grain and decreases the abnormal grain growth. This occurs because at the sintering temperature the addition of Cr_3C_2 dissolves in the Co, which reduces the solubility of W and C particles in liquid Co, thereby the rate of WC grain growth is reduced.

The SPS process has the advantage of high heating rate with shorter sintering time, at comparatively lower sintering temperature, so the final sintered grain size is expected to be

much smaller than that in conventional sintering (Sivaprahasam *et al*., 2007). When combining the benefits of grain growth inhibitor additions and rapid sintering, it is possible to restrict the grain growth further; it can restrict the WC grain size to about 435 nm. The WC grain growth occurs by Ostwald ripening (1896) with dissolution of smaller WC grains and re-precipitation. The reduction in surface energy of the solid is attributed to the driving force which allows small grains to dissolve and large grains to grow (Park *et al*., 1996). Although this requires diffusion through the binder phase, the rate is controlled by interface kinetics due to the faceted morphology of the WC grains where growth occurs by a 2-dimensional nucleation or defect assisted process (Park *et al*., 1996). This growth is predominantly interface controlled (Wittmann *et al.*, 2002), and addition of refractory carbides Cr_3C_2 can alter the interface energy and interfere with the dissolution re-precipitation step. The addition of Cr_3C_2 as a small quantity has a little influence on the factors, except the interface energy in Equation 2.5 (Sun *et al*., 2007). Equation 2.5 shows that with decreasing interfacial energy, γ, the average grain size of WC grain sizes is reduced when the other factors are invariable.

$$\bar{r}^3 - r_0^3 = 3/2 \times (D_\gamma \Omega^2 C_\infty)/RT \times t \quad \text{.....2.7}$$

where: $\bar{r}$ = average grain size at equilibrium state (nm), r_0 = grain size (nm), D = diffusion coefficient of solute atom (m^2/s), γ = specific interfacial energy (J/m^2), C_∞ = average solubility of solute (mol l^{-1}), Ω = mole volume (m^3/mol), T = temperature (K), and t the sintering time (s).

Sun *et al*. (2008) showed interesting insights on the effect Cr_3C_2 had on WC-11Co consolidated by SPS at 1200°C with a holding time of 5 minutes and a constant pressure of 40 MPa. As the Cr_3C_2 content was increased, the grain size of WC-11Co decreased until the minimum grain size was reached at 0.6 wt% Cr_3C_2 (Figure 2.22 (a)) and increased again at 0.8 wt% Cr_3C_2. The hardness followed a similar tread as expected (Figure 2.22 (b)), with a peak at 0.6 Cr_3C_2.

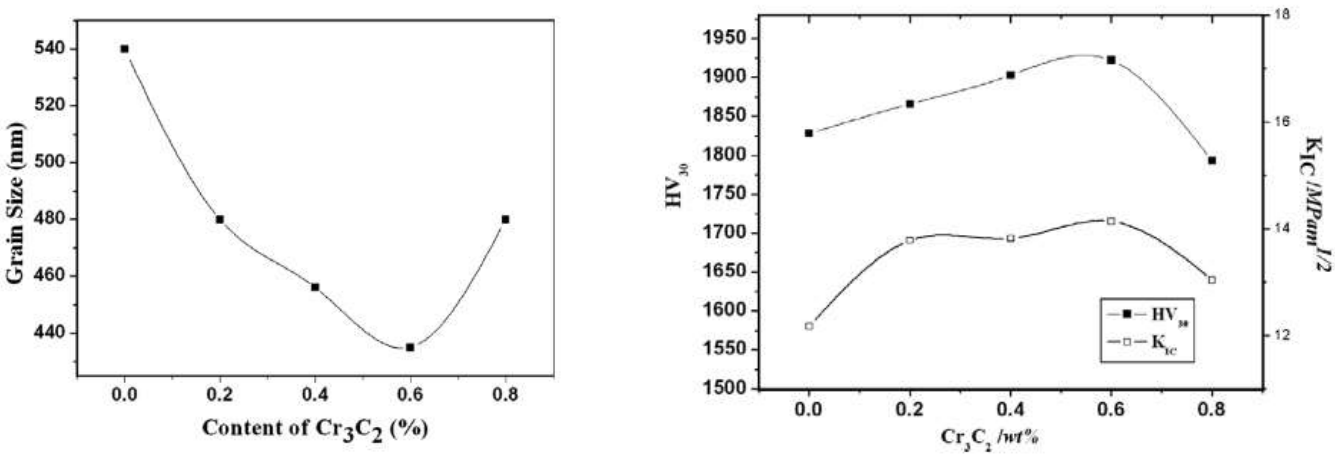

Figure 2.22 (a) Effect of Cr_3C_2 content on grain size on WC-11Co carbides consolidated by SPS, and (b) hardness of WC-11Co with Cr_3C_2 content (Sun *et al*., 2008).

2.13. Combined additions of Cr_3C_2 and VC

Bonache *et al*. (2011) investigated the effect of VC and Cr_3C_2 in WC-12Co on mechanical properties of samples consolidated by SPS at 1100°C and 80 MPa to obtain full densification and fine grain size. Two base samples were prepared, WC–12wt%Co mixture of nanocrystalline powders with WC grain size of 30–80 nm obtained by the spray conversion process and WC–12wt%Co mixture ultrafine powders with WC grain size of 100–250 nm obtained by vapour phase synthesis. A high densification in samples with additives was due to the limitation of the phenomena of diffusion and migration of Co. They achieved the desired grain sizes and full densification. The grain size of a base sample was reduced from an average grain size of 216 ± 12 nm to an average grain size of 154 ± 10 nm with density of 98.95 ± 0.11 and VC was more effective than Cr_3C_2 that had grain size of 207 ± 10 µm with a relative density of 99.74 ± 0.10.

Morteza (2013) investigated the effect of Cr_3C_2 and VC additives to WC-10 wt% Co on mechanical properties. Both VC and Cr_3C_2 were effective grain growth inhibitors, and they improved mechanical properties significantly. There was an increase in hardness as grain growth inhibitors were introduced, but at a higher temperature there was a slight reduction in hardness (Figure 2.23 (Morteza *et al*., 2013)).

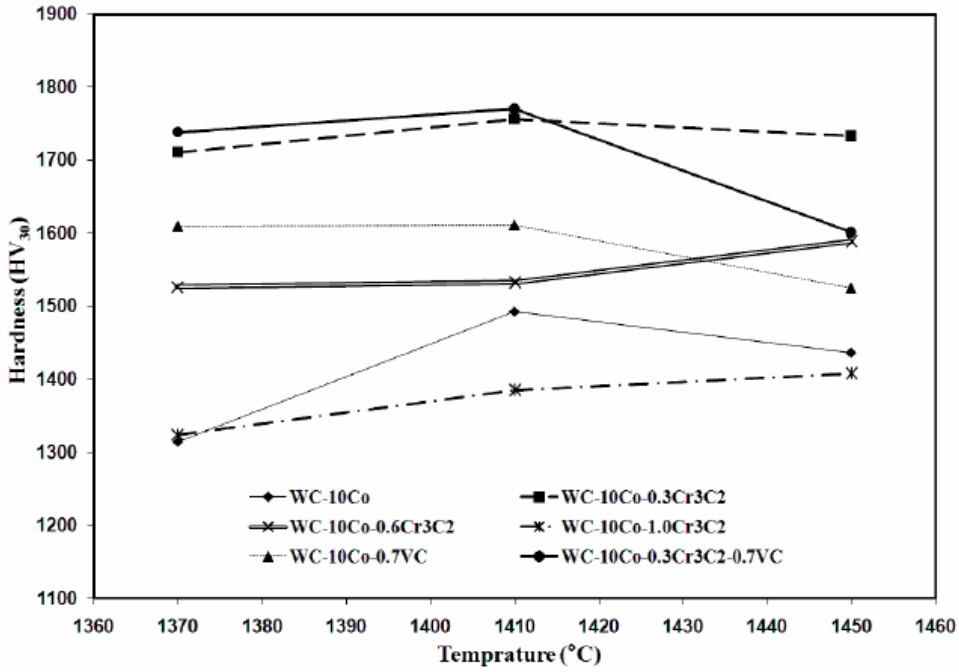

Figure 2.23 Hardness of samples at different sintering temperatures (Morteza *et al*., 2013).

The WC-10Co-0.3Cr_3C_2-0.7VC sample had higher hardness (1770 HV_{30}) compared to the control sample WC-10Co (1600 HV_{30}) (Morteza *et al*., 2013). This agreed with the decrease in grain size (Table 2.4) where WC-10Co-0.3Cr_3C_2-0.7VC had grain sizes of 0.45 ± 0.21 µm, while WC-10Co had 0.89 ± 0.41 µm grains. The grain size of WC-Co-Cr_3C_2 tended to increase as the composition of Cr_3C_2 was added to the control sample.

Table 2.4 Grain sizes of WC alloys obtained at 1410°C (Morteza *et al*., 2013).

Compositions (wt%)	Average grain size (µm)
WC-10Co	0.89 ± 0.41
WC-10Co-0.3 Cr_3C_2	0.53 ± 0.23
WC-10Co-0.6 Cr_3C_2	0.53 ± 0.30
WC-10Co-1.0 Cr_3C_2	0.64 ± 0.33
WC-10Co-0.7VC	0.62 ± 0.28
WC-10Co-0.3 Cr_3C_2 -0.7VC	0.45 ± 0.21

2.14. Ruthenium as an additive in WC-Co

An investigation of the effect of ruthenium additive in WC-Co done by Shing (2001) found the mechanical properties of WC-10wt%Co to have increased with ruthenium content. Ruthenium provides good wear resistance, and it is also a weak grain growth inhibitor compared to Cr_3C_2 and VC (Shing *et al*., 2001). Figure 2.24 shows the effect of Ru content on mechanical properties of WC-10Co-Ru.

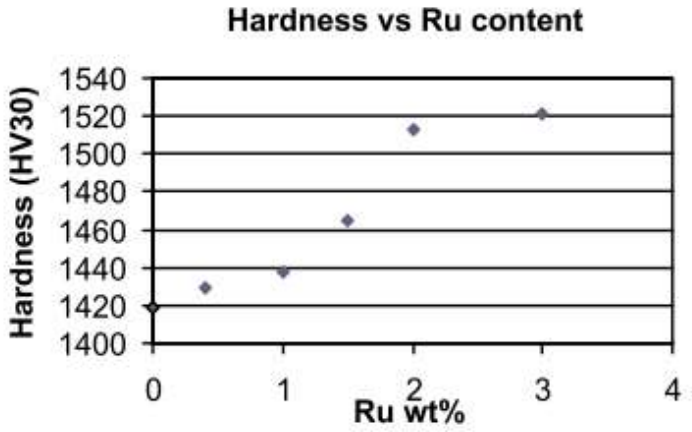

Figure 2.24 Effect of Ru content on the hardness of WC-10wt%Co (Shing *et al*., 2001).

The mechanical properties and advantages of Ru additions in WC-Co are due to it being a grain growth inhibitor for conventional WC-Co, the strengthening of the binder phase and the resistance to chemical attack (Shing *et al*., 2001). Ruthenium additions can also provide for flexural strength and hardness in hardmetals. When ruthenium is added to cobalt, it changes crystal structure from fcc to hcp at different Co/Ru ratios and temperatures: when the ratio of Co to Ru is 90:10, the transformation happens at 420°C, when the Co to Ru ratio is 80:20 the transformation happens at 900°C, and when the ratio is 70:30 the transformation happens at 1050°C (Penrice, 1987). Therefore, only a small amount of ruthenium is needed to produce the hexagonal structure.

Cemented carbides are not only subjected to wear processes in mining applications, but also experience chemically aggressive environments; corrosion can play a major role in the

degradation of their surfaces and can significantly accelerate wear (Human and Exner, 1996). In long-life applications, the corrosion properties of cemented carbides can have a large influence on overall material performance (Potgieter *et al*., 2014). When Potgieter *et al*. (2014) investigated the corrosion behaviour of WC-Co-Ru alloys in aggressive chloride media, they found that when increasing Ru additives in WC-10wt%Co from 0.4 to 4 wt% Ru, they observed an increase in corrosion resistance of the materials. Although the effect was not as prominent as when stainless steel had Ru added. A drastic decrease in corrosion rate was more for samples containing 2 and 3 wt% Ru when compared to the alloys with relatively low Ru additives. The sample with VC (4 wt% VC) had less effect in corrosion resistance in synthetic mine water than samples with similar Ru additives. Although corrosion resistance is not a prime requirement of hardmetals, this property is very important in its industrial uses (Scholl *et al*., 1992). Since the cobalt binder phase is the most susceptible to corrosion in acidic and neutral media, it follows that improvement of the corrosion resistance of the binder will have a major influence on the overall corrosion resistance (Wentzel *et al*., 1997). In principle, Co-based cemented carbide does not passivate. Aggressive media preferentially attack the binder while the tungsten carbide itself remains immune (Sutthiruangwong and Mori, 2003). After dissolution of the binder, there remains a skeleton of tungsten carbide (WC) at the surface (Sutthiruangwong and Mori, 2003). Corrosion attack proceeds predominantly at locations where the WC phase has fallen out after localised initiation of corrosion has taken place (Potgieter *et al*., 2014). The investigation by Hochstrasser *et al*. (2007) comparing WC-Co hardmetals in acidic, neutral, and alkaline solutions revealed a steady corrosion rate that decreased with increasing solution pH. At room temperature, cemented carbides show an excellent resistance in basic and neutral aqueous solutions (Potgieter *et al*., 2014). Strong acid solutions such as hydrochloric and sulphuric acid can cause severe corrosion and material degradation. The presence of aggressive chloride ions in the electrolyte solution could cause increasing corrosion rates.

Potgieter *et al.* (2014) investigated the corrosion behaviour of tungsten carbide with ruthenium as the additive in a chloride medium and found that an increasing amount of Ru improved the corrosion resistance of all the alloys, although the effect was not as dramatic as that observed with stainless steels containing Ru that were placed in corrosive media (Potgieter *et al*., 2014). Potgieter *et al*. (2014) added up to 3 wt% Ru to WC-Co alloys, finding

that additions up to 2 wt % improved the corrosion resistance, but further increases of Ru exhibited very little further improvement. Nevertheless, the decrease in corrosion rate in sodium chloride and synthetic mine water was large for the two alloys containing the highest amounts of Ru (2 and 3 wt%) compared to the other alloys, especially the base alloy without any Ru. All the alloys evaluated experienced more corrosion in sodium chloride alone than in the synthetic mine water solution, which consisted of a mixture of chloride and sulphate salts, albeit at lower amounts (Potgieter *et al*. 2014). The alloy containing VC had a lower corrosion resistance in synthetic mine water than that with a similar amount of Ru. The improvement in corrosion resistance of WC-Co alloys was attributed to the stabilising effect of Ru on fcc Co. Potgieter *et al.* (2014) found that ruthenium was more effective than VC in increasing corrosion resistance of WC-Co alloys. Better corrosion and mechanical properties are therefore anticipated by adding both Ru and VC in cemented carbides.

Improving the hardness of the binder phase by modification also helps to improve fracture toughness of the overall alloy, and for a Co binder, fracture toughness decreased with hardness (Wentzel *et al*., 1997). Chipise *et al.* (2018) investigated the effect of Ru on WC-VC-Co alloys and found that hardness increased with increased Ru additions due to a combination of decreased grain size and increased solid solution strengthening with improved corrosion and wear resistance (Chipise *et al*., 2018 and 2017). Ruthenium additions generally compromised fracture toughness, although there was improvement for some compositions, this is because hardness increased with increasing Ru additions in all alloys due to a combination of decreased grain size and increased solid solution strengthening. They also found that ruthenium additions were more effective in improving hardness when substituting Co than when replacing WC, which is expected since Co is softer than WC.

2.15. Grain Size and Binder Content

The effect of grain size on mechanical properties of cemented carbides has been studied from nano-grains to extra coarse grains (Figure 2.25 (b) (Sandvik, 1998)). Tungsten carbide (WC) grains had an inversely proportional relationship, i.e., decreasing WC grain size resulted in increased hardness, compressive and bending strength, with the opposite effect on impact, rupture and fracture toughness. Thus, it is important to know which grain size one desires for

applications, because WC grain size can be used to determine the potential applications (Figure 2.25 (a) (Sandvik, 1998)).

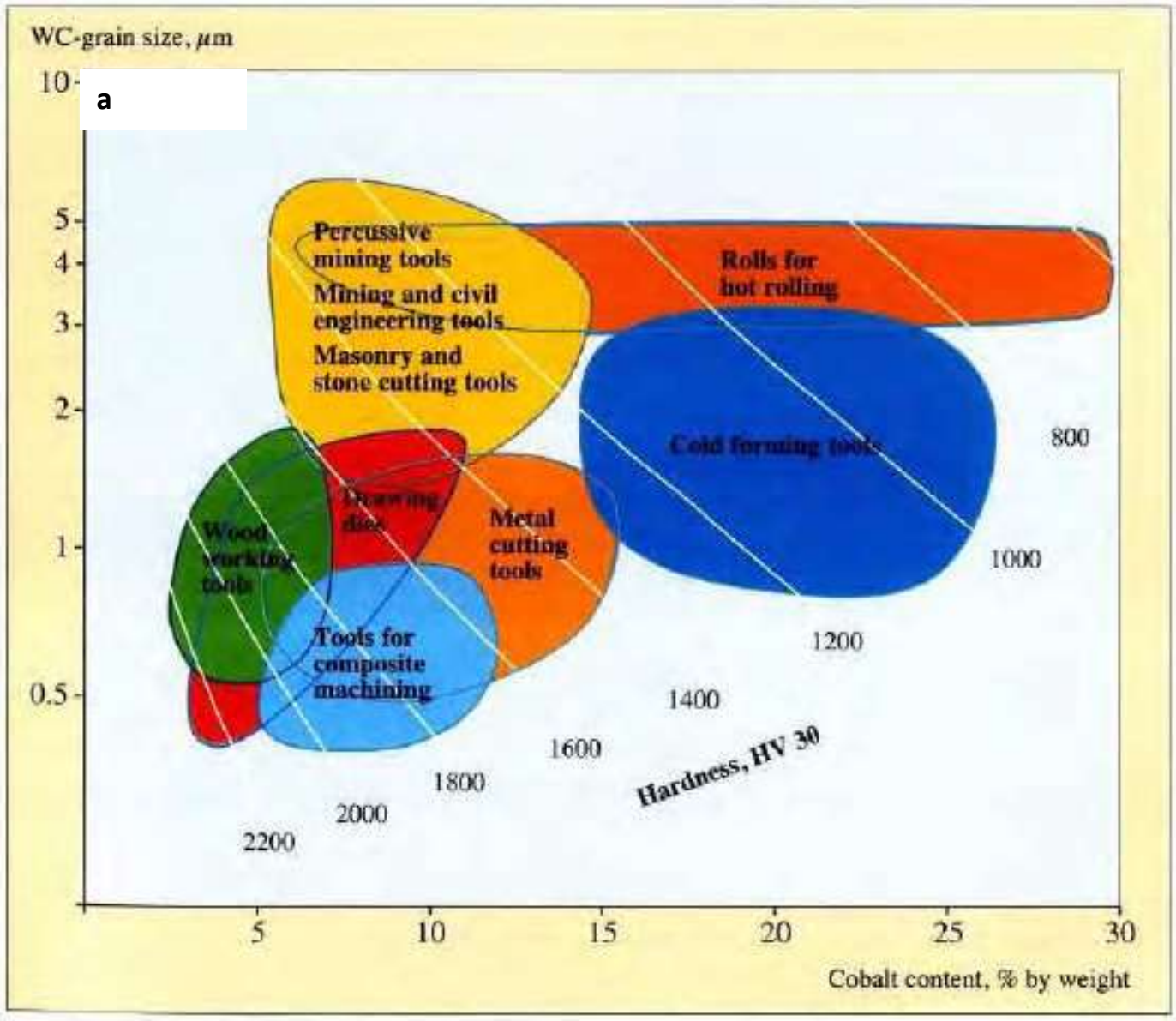

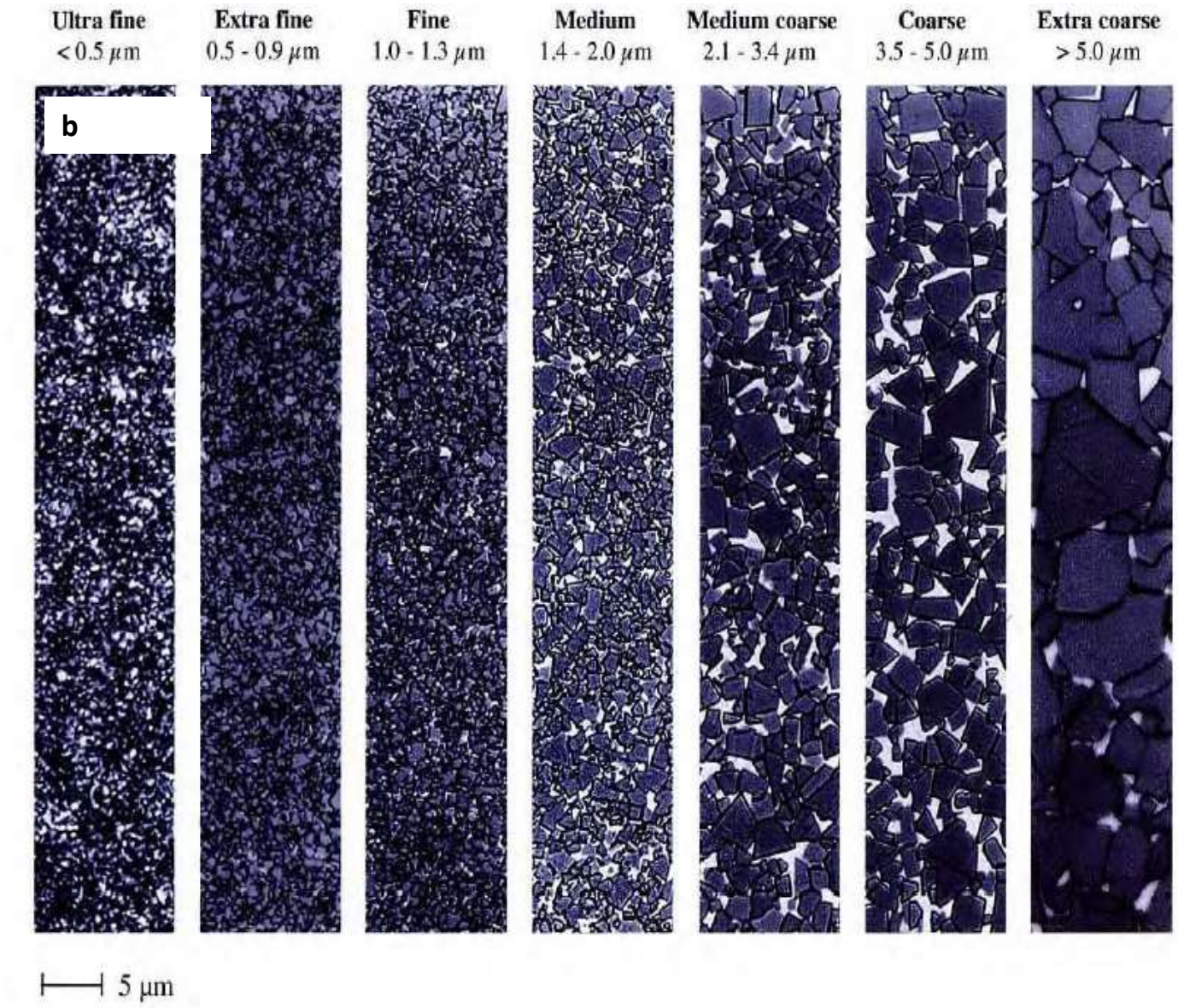

Figure 2.25 (a) Application of Cemented carbides according to WC grains and Co content, (b) classification of WC grain size (Sandvik, 1998).

2.16. Material characterisation and analysis

2.16.1. Average grain size analysis

The average grain size plays an important role in cemented carbides and their mechanical properties (Sandvik, 1998). According to the Hall-Petch equation (Hall, 1951), reduction of grain size produces stronger materials at ambient temperatures. This is due to the average number of grain boundaries that must be passed by dislocations in permanent deformation, where grain boundaries act as barriers to dislocation movement and slow down the

deformation rate. There are different ways to calculate the average grain size of a material, through line intercept or computer software that has algorithms which can successfully calculate the average grain size using the same principle. Since reducing the average grain size of a cemented carbide increases hardness, it is for this reason there have been several studies focused on grain refinement in cemented carbide and other materials in general (Wei *et al*., 2015). In cemented carbides, the reduction of WC grain size to below 1 µm provides a large increase in hardness and wear resistance due to improved erosion and abrasion resistance, transverse rupture strength, and compressive strength.

The superior mechanical properties of cemented carbides allow them to replace the traditional high-speed steels for applications requiring higher hardness and wear resistance (Fernandes *et al.,* 2011). They have also taken over applications such as metal cutting, metal forming, and wear resistant parts. There are several ways used to describe the average grain size of cemented carbides but, there are three main classifications that describe the hardmetals depending on the WC grain size which include (Figure 2.26) (Upadhyaya, 2001):

- Submicron grains, where WC grains are between 0.5 µm to 1µm,
- Ultrafine grains, where WC grains are < 0.5 µm, and
- Nanograins, where WC grains are between 10nm to 9 nm or less.

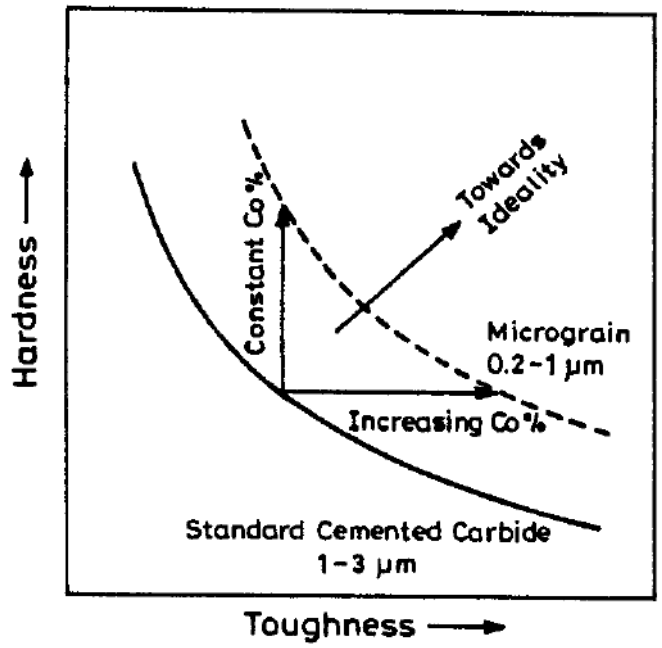

Figure 2.26 Comparison of conventional and micro-grained cemented carbides (Upadhyaya, 2001).

2.16.2. Contiguity and binder mean free path

Contiguity is described as the measure of the number of WC/WC contacts in the WC skeleton (Garcia *et al*., 2019). Many of the unique properties of cemented carbides are due to the formation of the WC skeleton, and its occurrence makes the simple rule of mixture predictions invalid for cemented carbides (Garcia *et al*., 2019). Exner and Fischmeister (1966), Roebuck and Bennett (1986) and Golovchan and Litoshenko (2003) all performed studies of WC contiguity (Table 2.5) and its relationship to the volume fraction of binder and in some cases, also to WC grain size. They found that, although hardness and toughness can be used to measure the mechanical properties of cemented carbides, contiguity and mean free path have a relationship with mechanical properties. The hardness of a material has a linear relationship with contiguity.

Similarly, the mean free path of the binder can be described as a function of average WC grain size and volume fraction of binder, as shown by Gurland (1958), Underwood (1970) and Roebuck and Bennett (1966). The volume fraction of binder is in turn proportional to the Co content (Table 2.6).

In summary, most properties of cemented carbides can be predicted by the Co content and/or the average WC grain size. The hardness and toughness may be described as a function of average WC grain size and Co composition (Garcia *et al*., 2019). Contiguity and mean free path are complementary variables and may be used to predict the mechanical properties. These relationships are empirical in nature and most often do not consider scatter due to WC grain shape, and width of the particle size distribution (Golovchan *et al*., 2003), bi-modal or multi-modal distributions, as well as any other carbide phases that may appear in the microstructure (Garcia *et al*., 2019).

Table 2.5 Contiguity formulae.

Reference	**Contiguity formula**
Exner and Fischmeister (1966)	$C = 0.074\ V_{Co}^{-1}$
Roebuck and Bennett (1986)	$C = 0.85 - 1.80V_{Co}$
Golovchan and Litoshenko (2003)	$C = 1 - V_{Co}^{0.644} \exp(0.391\sigma_{WC}/d_{WC})$

Based on Gurland's theory (1958) of particle contact, Warren and Waldron (1968) suggested that in the majority of hardmetals, the carbide phase exists as a continuous skeleton both during and after sintering. Contiguity is therefore a quantitative measure of the skeleton formation, which is defined as the ratio of grain boundary surface (WC/WC interface) to total surface (WC/WC + WC/Co interface).

Table 2.6 Equations of mean free path.

Reference	**Mean free path formula**
Gurland, 1958	$\lambda = d_{WC}(1 - C)^{-1}V_{Co}(1 - V_{Co})^{-1}$
Underwood, 1970	$\lambda = d_{WC}V_{Co}(1 - V_{Co})^{-1}$
Roebuck and Bennett, 1986	$\lambda = d_{WC}(0.1 + 2V_{Co})$
V_{Co} is the volume fraction of Co binder, d_{WC} is the average WC grain size and σ_{WC} (Table 2.4) corresponds to the standard deviation of the average WC grain size (d_{WC}).	

2.17. Mechanical Properties

2.17.1. Hardness

Hardness is defined as the material's resistance to localised plastic deformation, indentation or penetration (Sandvik, 1998). Hardness can be a good measure of the material's surface properties like scratch, abrasive or indentation resistance (Sandvik, 1998). Hardness of cemented carbides decreases with increased in cobalt content (Figure 2.27 (Sandvik, 1998)).

Cemented carbides are generally hard, strong and tough and have a good wear resistance. The combination of hard, strong WC phase with a tough, wear resistant binder phase gives the physical and mechanical properties of the carbides (Sandvik, 1998). Apart from reducing grain size to improve mechanical properties of cemented carbides, other methods to improve the properties include the binder modification. The partial substitution of Co binder with other binder inhibitor materials has been instrumental in improving properties in recent years.

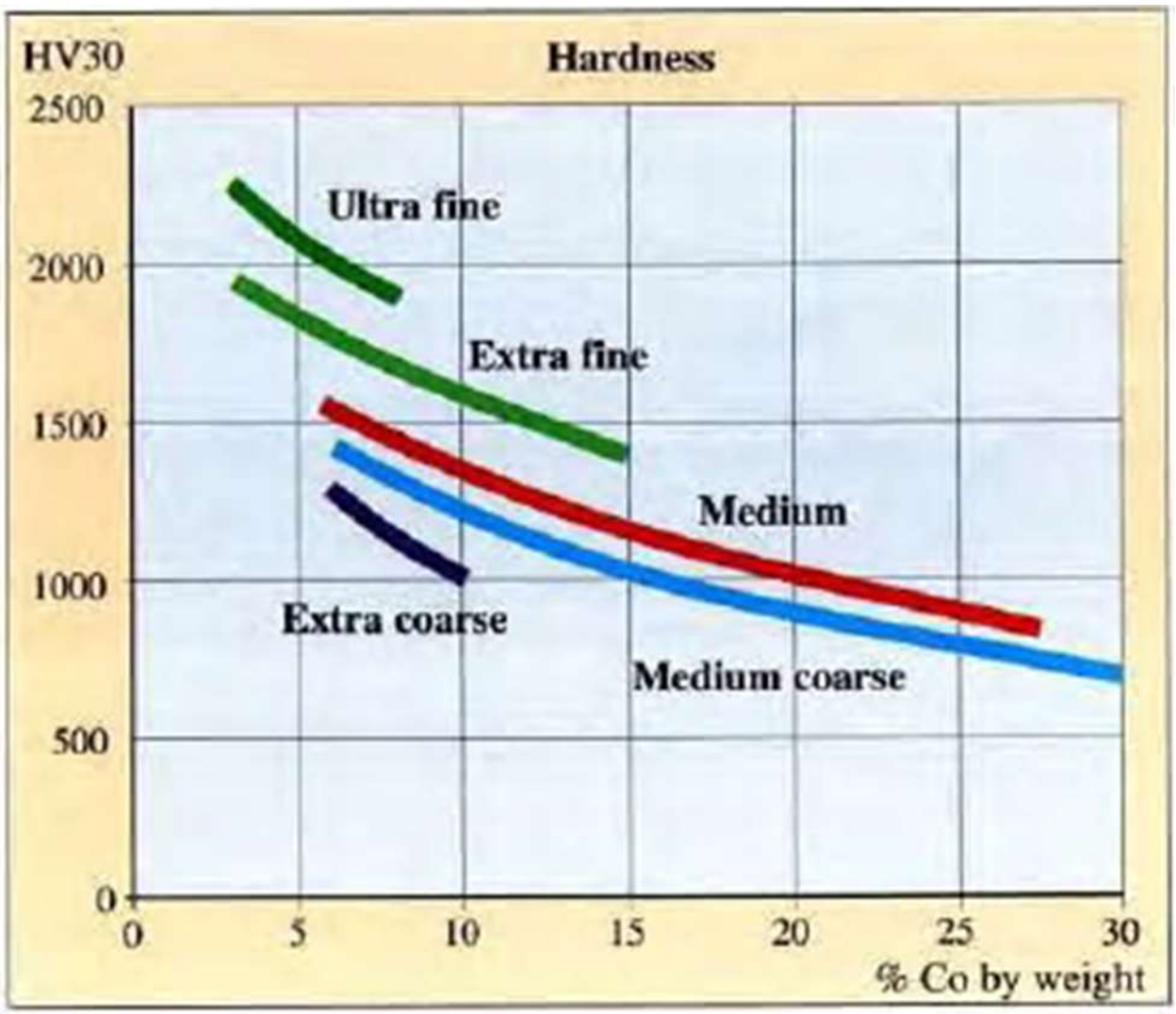

Figure 2.27 Hardness as a function of Co content for different WC grain sizes (Sandvik, 1998).

One of the applications of cemented carbides include cutting tools, which can reach a temperature of up to 1000°C. At such temperature it is important for alloy strength to control the tools performance, which is why the knowledge of mechanical properties and the effect of temperature on strengthening of cemented carbide is important (Table 2.7). The deformation mechanism and microstructural changes at high temperature have been investigated by many authors under different test conditions that have included bending, tension, compression and creep (Han *et al*., 2009). Han *et al*. (2009) investigated the effect of deformation mechanisms of WC-15wt%Co at high temperatures with and without VC additions. Three samples of WC-15wt%Co were fractured in three-point-bending at 1000°C with some samples doped in VC (Table 2.7). Samples of 30 x 4.5 x 1.2 mm^2 in size were

subjected to a bending test in an Instron-type high rigidity testing machine in a vacuum of 10^{-3} Pa with a tungsten heater. The crosshead speed was 1.7 $x10^{-6}$ m/s with a deformation velocity of the tensile surface of v = 7 $x10^{-3}$/s.

Table 2.7 Properties of the three WC–15wt%Co alloys investigated (Han *et al*., 2009).

Property	Grade A	Grade B	Grade C
Co volume% (V_{Co})	23.74	23.59	23.44
VC content (wt%)	0	0.4	0.8
d_{WC} (μm)	1.30 ± 0.33	0.35 ± 0.04	0.30 ± 0.04
Contiguity	0.20	0.19	0.20
λ (μm)	0.50	0.13	0.12
HV (GPa) (P = 50 N)	13.6 ± 0.2	16.3 ± 0.13	16.6 ± 0.14
Strain at fracture (%)	2.9	4.3	4.7

After sample preparation, Han *et al.* (2009) then did metallographic examination for the purpose of crack identification, cobalt concentration investigations and general microstructural observations to look for trends and deformation patterns that might be similar to the plastic deformation in cutting tools observed by Östberg (2005). The investigation has proven that the strain at 1000°C was due to fracture and cobalt movement. It was also expected that WC grain movement and deformation of WC grains would influence the strain, but in the work by Han *et al*. (2009) the contribution of cracks to the total strain was at most 10%. Therefore, the total strain was mostly due to plastic deformation and binder movement. The indication that there was cobalt drifting in the Han *et al.* (2009) investigation was due to the three components where cobalt layers on the surfaces with long and thin parallel streaks of cobalt layers in between WC grains, and the Co/W ratio on fracture surfaces was observed to be higher on the side of compression (Figure 2.28) than on the tensile side, while Co/W ratio on the fracture sides higher on tensile than on compression side and the Co pockets, widening of Co layers and de-bonding of WC/WC interface.

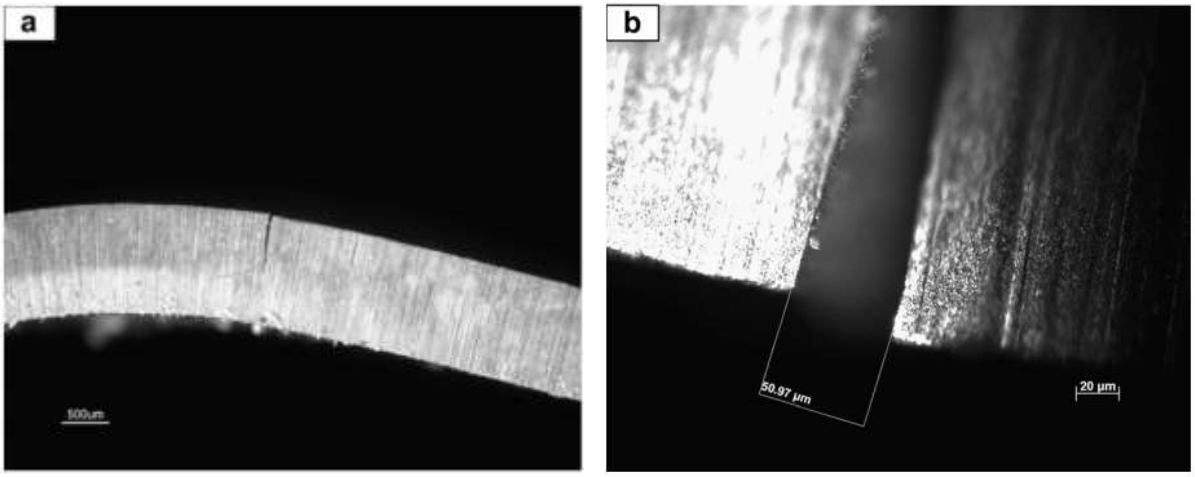

Figure 2.28 (a) Stereomicrograph showing macrocracks on one side surface of Grade C. (b) Reflected light micrograph: crack opening width measurement on one side surface of Grade C, showing a macrocrack wider than 50 ⌠m (Han *et al.*, 2009).

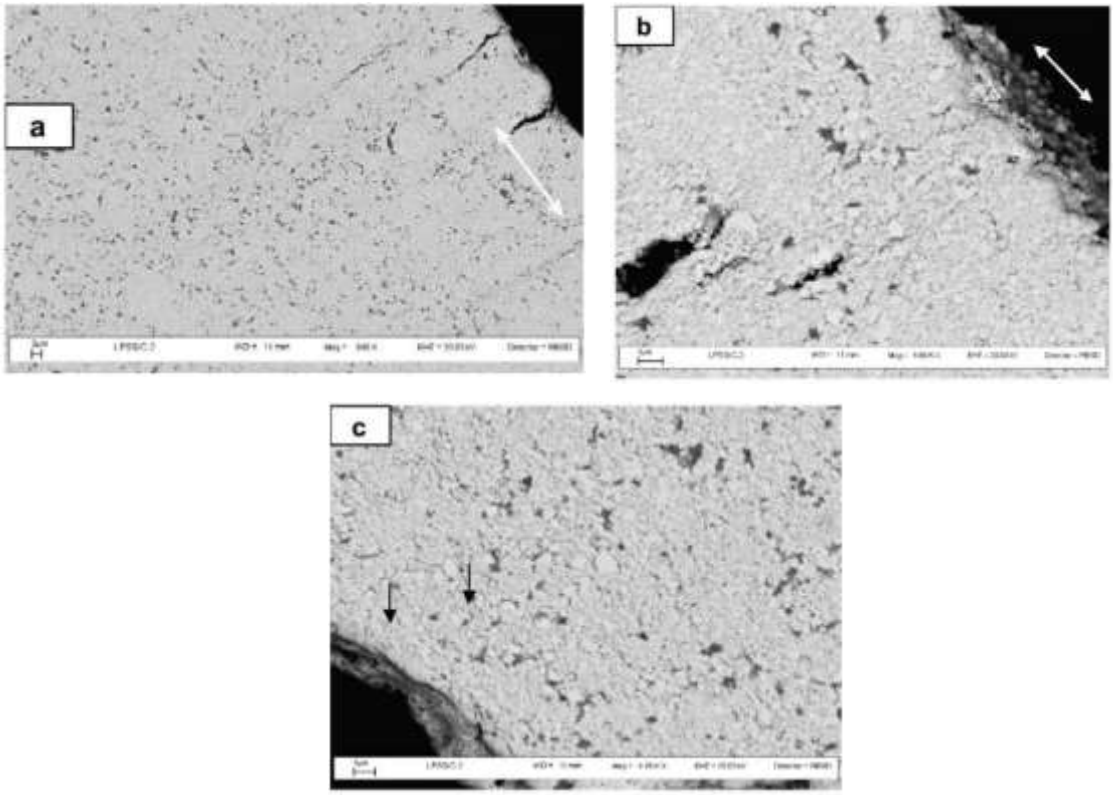

Figure 2.29 FESEM micrographs of (a) and (b) areas near the tensile surface and (c) an area near the compressive surface of Grade B (Han *et al.*,2009).

The drifting of cobalt binder confirms the results by Östberg (2005), as shown by Han *et al.* (2009). This was particularly true in the case of strained cobalt features as shown in Figure 2.29. The contribution of cracks in Grade A (Table 2.7) was less than that of VC grades, but plasticity of Co during fracture in Grade A was eminent. This was due to the large mean free

path in Grade A which allowed Co movements. It was observed that in grades with VC, cobalt movement was restricted with the expectation that grains could slide over each other more easily on account of their smaller size, which must have contributed to the higher level of strains in Grade A. The contiguity of tungsten carbide in Grades A, B and C is 0.20, which is not high enough to have a continuous WC skeleton. Therefore, Co carried more stress, deformed and grains moved with it, sliding over each other. Generally, at lower temperatures grain boundaries produce more strength, but are weak at higher temperatures. Grain boundary sliding is one of the dominant fracture mechanisms and generally occurs at temperatures higher than $0.4T_m$ and is always accompanied by grain boundary migration and dislocation movement. Östberg (2005) described high temperature deformation in cemented carbides as a gradual transition from brittle to plastic deformation, where the deformation initiation point is dislocation movements in the cobalt binder phase, followed by gradual increased grain boundary sliding that is facilitated by Co diffusion and dislocation climb in combination with dislocation movements and slip in the hard phase. Han *et al.* (2009) observed the wide spaces between WC grains which confirmed the results obtained by Östberg (2005), when he found that 10% of the WC grain boundaries were separated and infiltrated by Co.

The wide spaces were perpendicular to the applied tensile stress. Östberg (2005) explained that since it is generally energetically favourable for WC grains to form two WC/Co boundaries instead of two free surfaces, the cobalt diffusion into the boundary occurs simultaneously with WC grain decohesion. Further movement of the WC grains is facilitated by fully or partly infiltrated cobalt, which is why grain boundaries will often slide. The round WC grains in Grade A (Table 2.6) resulted from dissolution of WC in cobalt which increased with temperature. This was due to the tensile stresses producing stress concentration that caused the Co binder phase to wedge itself against the boundary and within a certain radius the stress field becomes energetically encouraging for dissolution of the hard phase grains. Han *et al.* (2009) concluded that in his investigation there was enough evidence that WC-Co grades with 15 wt% Co and grain sizes from 0.3 to 1.3 μm underwent large plastic strains when bend tested 1000°C and that the strains can be accounted for by cracking, Co drifting and movement of WC grains. His investigation has provided direct evidence that additions of VC to WC-Co cause the presence of steps on the WC grains. The steps were previously only visible by TEM, but

the fracture surfaces showed the steps to be visible because (V, W)C particles formed along the WC boundaries, weakened the WC-Co interfaces and made easy paths for fracture propagation.

2.17.2. Fracture toughness

Fracture toughness is defined as the material's resistance to fracture. When materials are exposed to static or dynamic loads, stresses build within the material. The material's strength and deformability are therefore crucial. Normally, these properties are important when dealing with shock loading. Toughness of the material can be determined in different ways, the most common for hardmetals being Palmqvist's (1962) method which tends to overestimate the material's toughness while Shetty's method (1985) underestimates toughness (Upadhyaya, 2001).

The toughness of cemented carbide is dependent on the binder content and carbide grain size (Sandvik, 1998). An increase in cobalt binder (Figure 2.30) results in a greater toughness. However, different cemented carbides have different toughness behaviours.

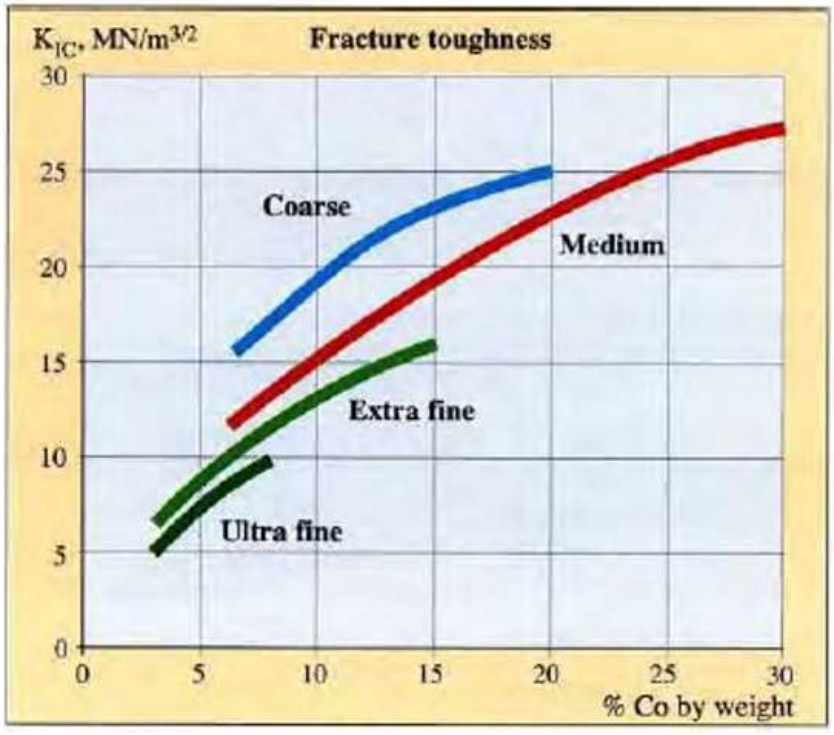

Figure 2.30 Fracture toughness as a function of Co content (Sandvik, 1998).

The relationship between residual surface stresses and Palmqvist cracks can be confusing. In a review of quantitative and non-destructive measurements of residual stresses by James and Buck (1980), they suggested that microcracks generated by conventional hardness indentations may be used to measure residual stresses in brittle materials. The presence of surface stress was investigated in WC-Co by studying the effect of cyclic compression on WC-Co by subjecting the material to cyclic compression stresses for different numbers of cycles. Luyckx and Vekinis (1986) investigated the relationship between the crack length of Palmqvist and residual surface stresses in WC-Co by conducting two sets of experiments where samples were subjected to compression stresses ranging from 3.0 to 5.5 GPa while keeping the number of cycles constant at N=100. The second experiment kept compression stress at σ = 4.5GPa while cycles were varied from 1 to 150. Luyckx and Vekinis (1986) found that the length of the Palmqvist cracks and tensile stress in Co decreased with increasing compressive pre-stress and with increasing number of compressive cycles, while WC compressive stress increased (Figure 2.31). Usually the tensile stresses are positive and compressive are negative, but in the study they found that $\Delta l/l_0$, $(\Delta\sigma/\sigma_0)_{Co}$ and $(\Delta\sigma/\sigma_0)_{WC}$ were all negative, where $(\Delta\sigma/\sigma_0)_{WC}$ = fractional change in residual stress in WC and $(\Delta\sigma/\sigma_0)_{Co}$ = residual change in Co, and $\Delta l/l_0$ = length of Palmqvist cracks.

The results by Luyckx and Vekinis (1986) in Figure 2.31 show a one-to-one correspondence between $\Delta\sigma/\sigma_0$ and $\Delta l/l_0$ below a limit stress, which was expected to vary with stress conditions, and below a limit number of cycles, which was low compared with the number of stress cycles undergone by average cemented carbide components. When they compared Figure 2.31 a) and b), the curves $\Delta\sigma/\sigma_0$ vs $\Delta l/l_0$ from the two experiments were different. This indicated that the relationship between Palmqvist crack length and residual surface stresses depends on the conditions of precompression. This suggests that other factors, besides the changes in residual stresses, contribute to the shortening of the Palmqvist cracks. Palmqvist crack lengths, therefore, cannot provide quantitative information on residual surface stresses. In conclusion, changes in Palmqvist crack lengths can only provide rough indications of changes in residual surface stresses and only within relatively narrow conditions

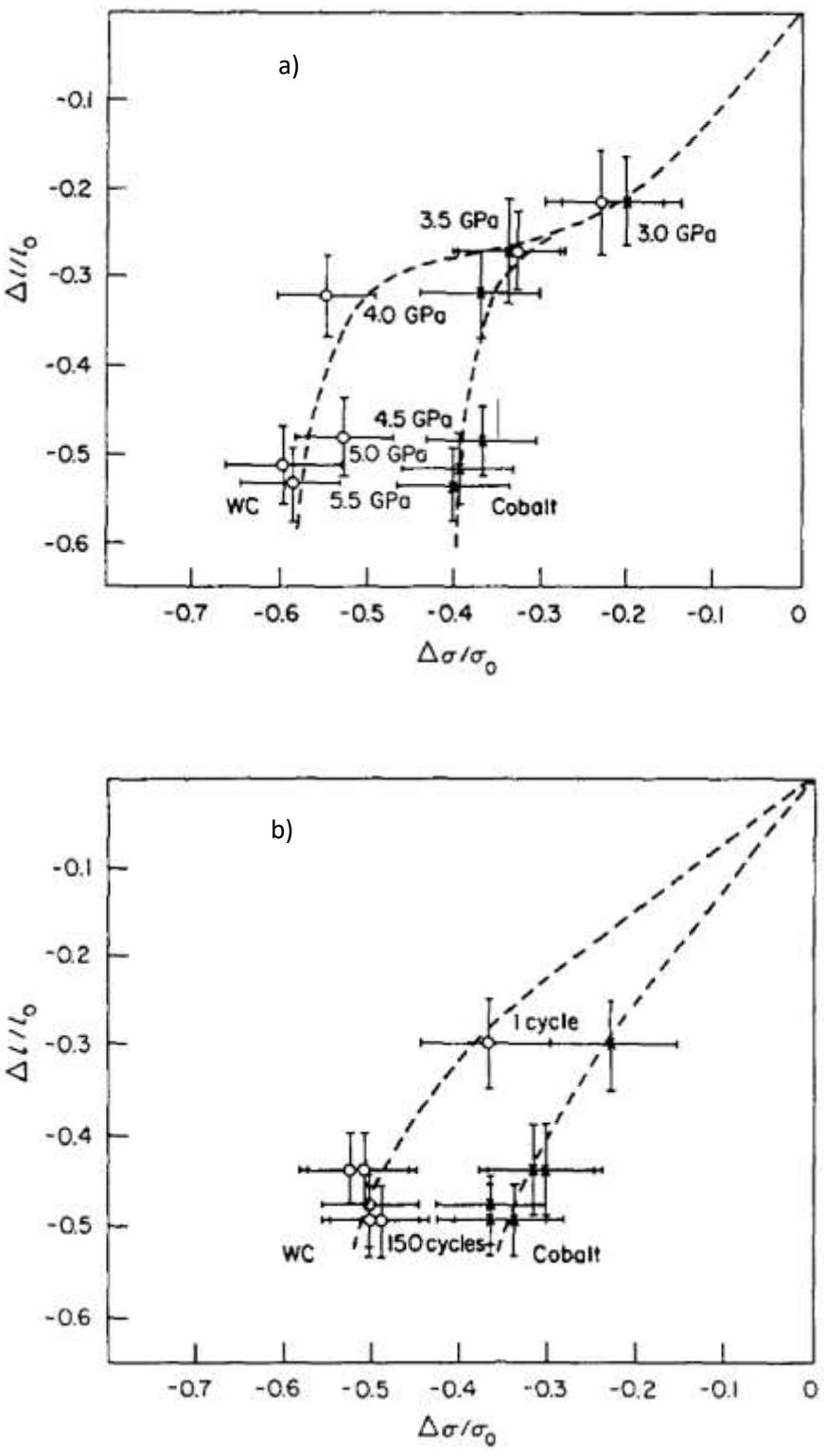

Figure 2.31 a) $\Delta\sigma/\sigma_0$ vs $\Delta l/l_0$ for N=100 and cyclic compressive stress from zero to a maximum of 3.0 to 5.5 GPa b) $\Delta\sigma/\sigma_0$ vs $\Delta l/l_0$ for σ =4.5 GPa and N = 1 to 150 (Luyckx and Vekinis, 1986).

Siwak (2021) investigated the mechanical behaviour of SPS prepared WC-6wt%Co alloyed with Cr_3C_2, TaC-NbC, TiC, and VC. He sintered all his materials at a temperature of 1200°C with 400°C heating and cooling rate and 80 MPa constant pressure for 5 minute holding time.

Table 2.8 Sample composition with microstructural properties of WC-6wt%Co by Siwak (2021).

Series Number	Composite Designation	Microstructure Parameters of SPSed WC-Co Cemented Carbides			
		f_{Co}, vol%	d_{WC}, nm	C_{WC}, -	λ_{Co}, nm
1	WC-6Co	10.12	416	0.81	5.06
2	WC-6Co-0.5Cr_3C_2	10.06	284	0.74	1.25
3	WC-6Co-1Cr_3C_2	9.99	-	-	-
4	WC-6Co-0.5TaC-NbC	10.10	204	0.69	2.88
5	WC-6Co-1TaC-NbC	10.07	-	-	-
6	WC-6Co-0.5TiC	10.02	226	0.75	2.22
7	WC-6Co-1TiC	9.91	-	-	-
8	WC-6Co-0.5VC	10.04	244	0.78	3.98
9	WC-6Co-1VC	9.96	-	-	-

Siwak (2021) observed that although samples sintered at higher temperature and pressure will have smaller WC grain size. The Co binder mean free path, λ_{Co}, is normally sensitive to alloying. The mean free paths varied in the range of 1.25 - 5.06 nm regardless of the consistency of Co volume fraction. Similarly, carbide contiguity was seen not to have a significant change. The significant effect was observed in samples with Cr_3C_2. A general decrease in hardness as mean free path(Figure increase was observed.

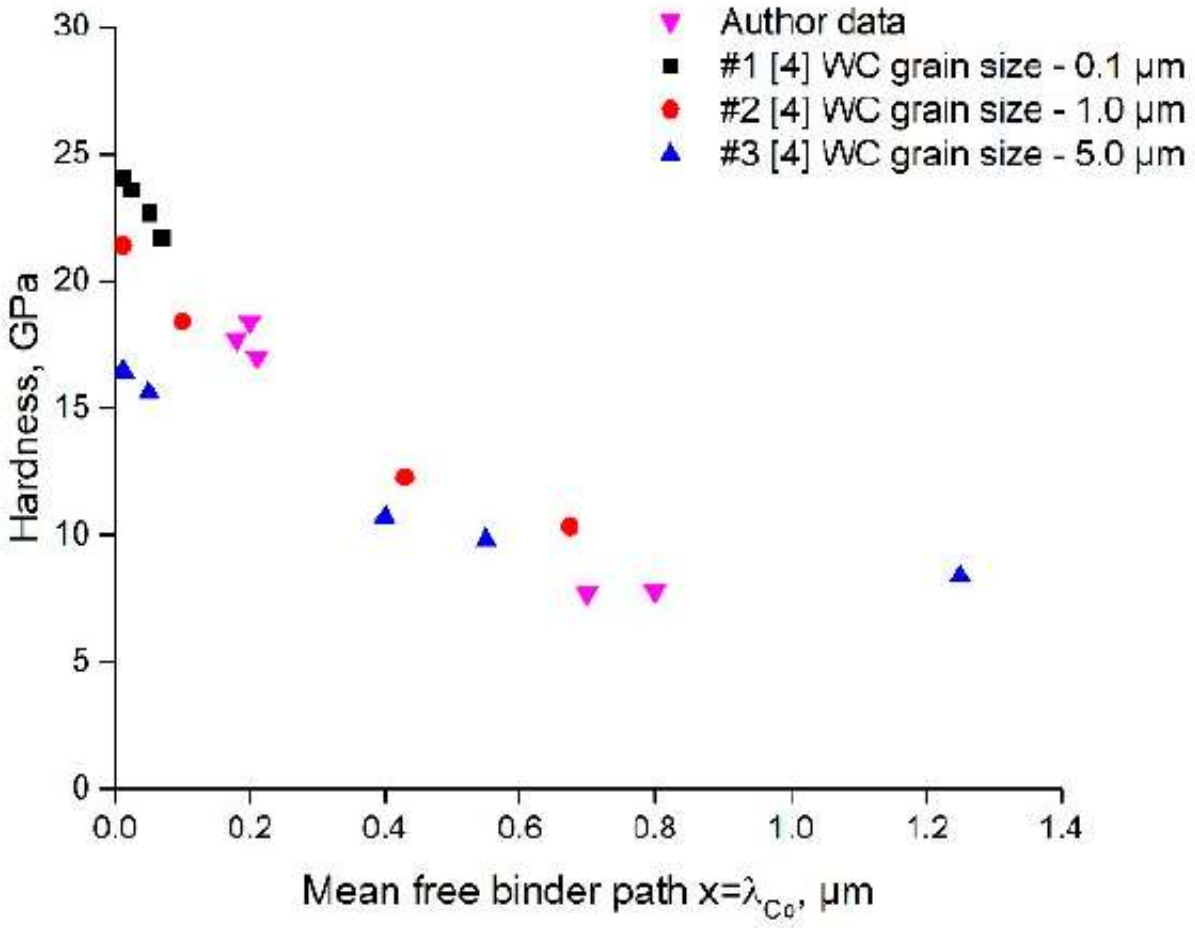

Figure 2.32 Hardness vs mean free path for three WC grain size and WC-6wt%Co by Siwak (2021).

Chapter Three

3. Experimental procedure

This chapter describes the experimental procedure that was followed to produce WC-10wt%Co samples with ruthenium, chromium carbide (Cr_3C_2) and vanadium carbide (VC) as additives, using spark plasma sintering (SPS) and the tests that were carried out to evaluate metallurgical and physical properties of the alloyed materials were: particle size analysis, density test, microstructure analysis, fracture toughness and hardness.

3.1. Starting powders

All materials were obtained from the suppliers indicated in Table 3.1.

Table 3.1 Specification of the starting powders.

Materials	Particle size (µm)	Crystal structure	Purity (%)	Source
WC	0.8	Hexagonal	99.8	Treibacher Industrie AG
Co	2	Hexagonal	99.8	Sigma-Aldrich Chemistry
VC	<2	Cubic	99.9	Sigma-Aldrich Chemistry
Ru	74 (-200 mesh)	Hexagonal	99.9	Sigma-Aldrich Chemistry
Cr_3C_2	43 (-325 mesh)	Orthorhombic	99.9	Sigma-Aldrich Chemistry

Table 3.2 List of consumables and chemicals used in the project.

Consumables and Chemicals	Source
96% Pure Ethanol	Wits, School of Chemistry
SPS Graphite Die Set with Punches	SGL Carbon, South Africa
SPS Carbon Cloth	SGL Carbon, South Africa
SPS graphite foil	SGL Carbon, South Africa
Polishing Diamond Suspension (9 ,6, 3 and 1 µm)	IMP Scientific Materialography
Grinding and Polishing Discs	Struers, USA
Mounting Polyfast	Struers, USA

3.1.1. Particle size analysis

A Mastersizer 2000 was used to measure particle size after the samples were ball-milled for 8 hours in a planetary ball-mill. The Mastersizer 2000 uses the Fraunhofer model and Mie theorem to obtain accurate sizes of the particles (Siwak *et al*., 2017). The Fraunhofer model predicts the scattering pattern of a known solid or cloudy disc-like particles passed through a laser beam. This model cannot work on its own, since not all particles are cloudy and have a disc-like shape and some may be transparent. Thus, the Mie theorem works in conjunction with the Fraunhofer model because it can accurately predict the light scattering behaviour of all materials. The Mie theorem predicts the way light is scattered by particles and the way light propagates through or is absorbed by the particles. Therefore, if the density, refractive index and absorption of the samples are known, the light scattering can be accurately predicted.

The Mastersizer has three district steps when measuring samples:

- **Sample preparation** where the sample powders are dispersed and mixed with distilled water to avoid agglomeration which will negatively affect the data analysis.
- **Pattern analysis** where the measurements are made. The detector array is made up of multiple detectors which accumulate light scattering from different angles and stores them. A single detector array takes snapshots of over 2000 pictures of the light scattering pattern passing through the analyser beam at a time and averages these results.
- **Malvern software** then uses the Fraunhofer model and Mie theorem to analyse and calculate the results and display them in a form of a graph.

The as-received powders (Table 3.1) were dispersed in distilled water and mixed using the ultrasonic probe for 5 minutes to break up any agglomerates. A few drops of the mixture were poured into the particles size analyser for measurements.

3.1.2. Powder Morphology

The powder morphology was determined by scanning electron microscopy using backscattered electron (BSE) and secondary electron (SE) modes to produce images.

Backscattered electron images are produced by the interaction of the incident beam of electrons with the samples and some of the electrons from the beam interact with the specimen and emit backscattered electrons (Borgh *et al*., 2013). The energy of backscattered electrons is directly proportional to the atomic number, and this is observed as differences in contrast.

3.2. Milling and mixing

The powders of WC, Co, Ru, Cr_3C_2 and VC were mixed in different proportions (Table 3.3) with ethanol (97% alcohol) and milled using a Fritsch PULVERISETTE 6 milling machine to reduce the particle size. The powders were mixed in a stainless-steel milling bowl with an inside diameter of 7 mm, a zirconia oxide lining and ~ 0.78g of tungsten carbide milling balls. The powders and milling balls were carefully weighed to achieve a 4:1 ball-to-powder ratio. Milling was done at a speed of 300 rpm for 8 hours to break up the agglomeration of the particles. Powders were then dried using a rotary evaporator for 30 minutes at 80°C.

Table 3.3 Sample compositions (wt%).

Alloy series	WC	Co	Ru	VC	Cr_3C_2
WC-10Co	90	10	-	-	-
WC-10Co-0.2VC	89.8	10	-	0.2	-
WC-10Co-0.2 Cr_3C_2	89.8	10	-	-	0.2
WC-10Co-0.2Ru	89.8	10	0.2	-	-
WC-10Co-0.4VC-Cr_3C_2	89.6	10	-	0.2	0.2
WC-10Co-0.4Ru-Cr3C2	89.6	10	0.2	-	0.2
WC-10Co-0.4Ru-VC	89.6	10	0.2	0.2	-
WC-10Co-0.6Ru-VC-Cr_3C_2	89.4	10	0.2	0.2	0.2

3.3. Sintering

After the mixing and milling, a Mastersizer 2000 was used for particle size analysis. The samples were then dried using a Heidolph rotary evaporating machine at 80°C with 120 rpm speed for 30 minutes to evaporate all ethanol that was present during the mixing and milling. The powders were then sintered using a SE-607 spark plasma sintering machine (FCT; Germany). The powder was poured into a cylindrical graphite die with an inner diameter of

20 mm and a height of 5 mm. The SPS process was done under vacuum for 20 minutes with a holding time of 5 minutes to provide a clean atmosphere and evaporate impurities from the high surface area powder starting material. The pressure was set to 50 MPa and the temperature used was 1150°C. The heating and cooling rate were 200°C per minute. The temperature, time and pressure were selected to try and produce sintered materials and a short time, as compared to the conventional way which took more than 24 hours to produce. These parameters were selected after reviewing the work done by Siwak *et al.* (2017) and Regi *et al.* (2017) which were closely related to the current project.

3.3.1. Optimisation of SPS Process

Obtaining full densification during the spark plasma sintering process is important, since fully densified materials provide superior mechanical properties. The effect of SPS temperature and time on densification of the base alloy (WC-10Co) was investigated, with the aim of achieving good densification (>99%).

3.3.1.1 Optimisation of sintering temperature

After milling, the WC-10Co powder was sintered at 1000°C, 1150°C, 1250°C and 1450°C. This was done to identify a temperature that would produce full densification with the holding time of 5 min at 50 MPa.

The sintering profile in Figures 3.1 to 3.4 shows how WC-10wt%Co base was sintered, with the aim of obtaining best sample density (>99%). Before sintering, powders were inserted in an SPS die set which was placed in the SPS chamber, then put under vacuum and heated to a temperature of 450°C at a rate of 200°C/minute. The temperature was then held at 1000°C for the first sample (Figure 3.1). The same composition sample was then sintered at 1150°C (Figure 3.2). The temperature was then increased to 1250°C (Figure 3.3) where the sample was held and finally, the last sample was held at 1450°C (Figure 3.4) for 5 minutes and subsequently cooled to 450°C at a rate of 200°C/min. The applied pressure was kept constant at 50 MPa throughout the process.

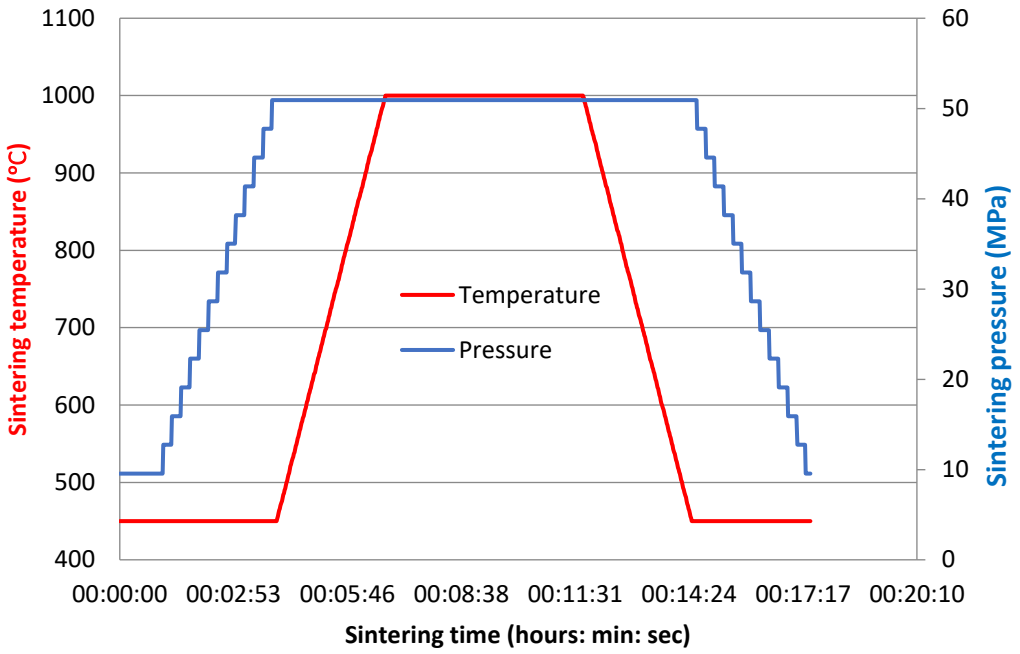

Figure 3.1 SPS profile for production of WC-10Co (wt%), sintered at 1000°C.

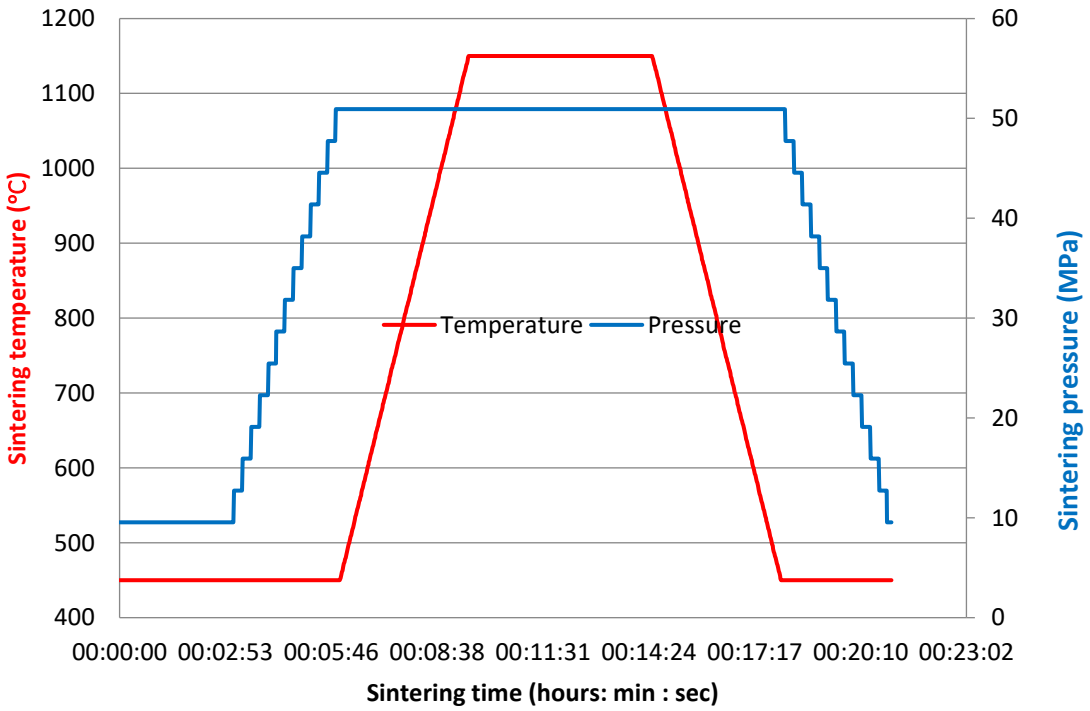

Figure 3.2 SPS profile to produce WC-10Co (wt%), sintered at 1150°C.

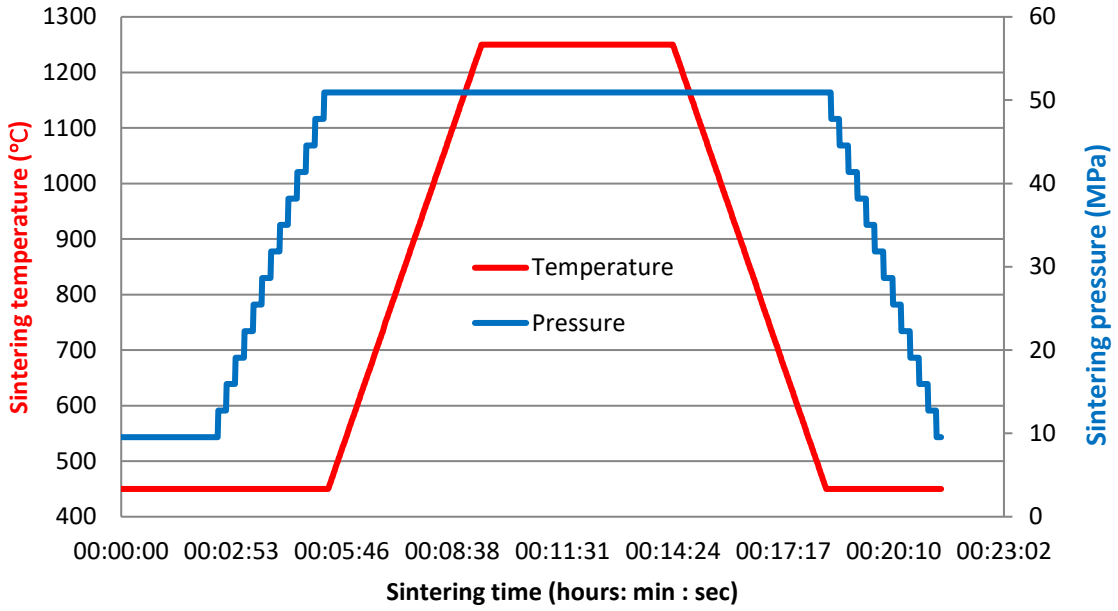

Figure 3.3 SPS profile for production of WC-10Co (wt%), sintered at 1250°C.

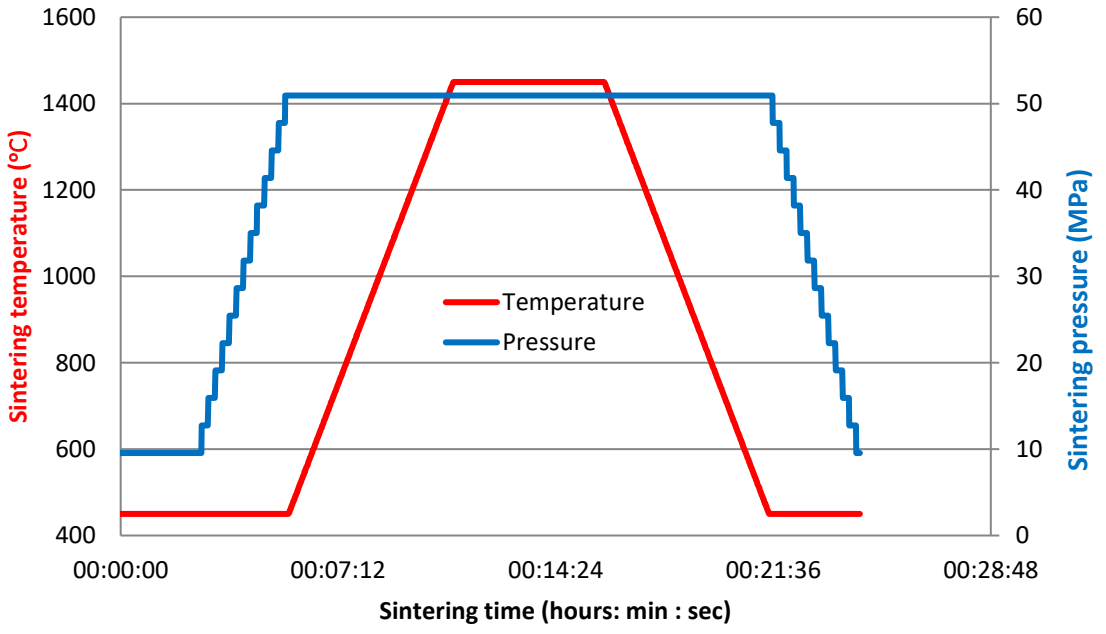

Figure 3.4 SPS profile for production of WC-10Co (wt%), sintered at 1450°C.

3.3.1.2. Optimisation of sintering dwell-time

Since full densification was not achieved when the base material was sintered at 1000°C, 1150°C, 1250°C and 1450°C, sintering dwell time was then increased to 8 minutes, keeping pressure constant at 50 MPa (Figures 3.5 and 3.6).

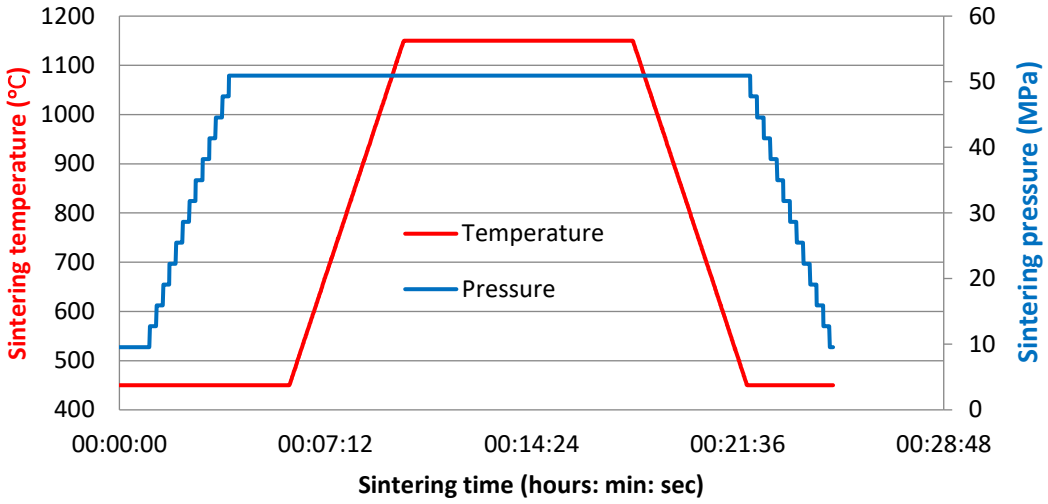

Figure 3.5 SPS profile for production of WC-10Co (wt%) at 1150°C.

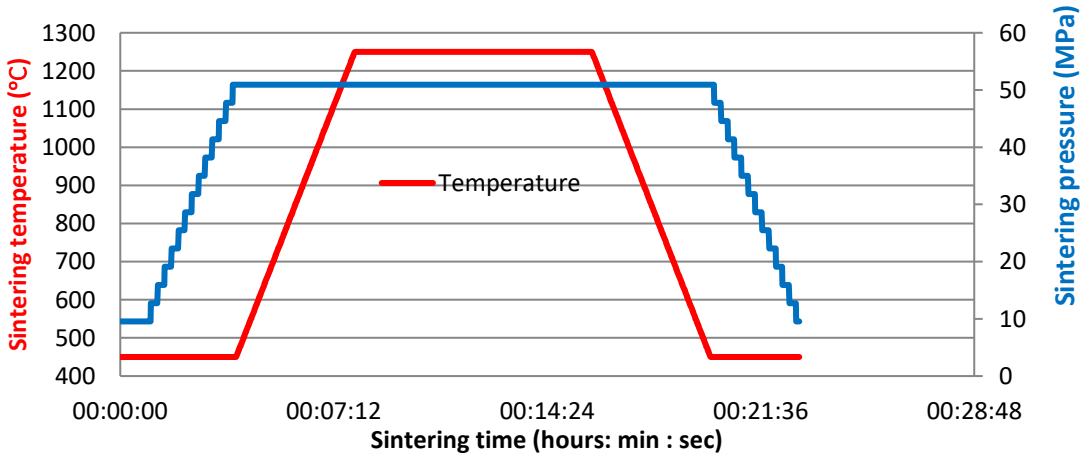

Figure 3.6 SPS profile for production of WC-10Co (wt%) at 1250°C.

When sintering time was increased from 5 to 8 minutes, keeping pressure constant (50 MPa), there was an increase in density. Two sintering temperatures were investigated, 1150°C and 1250°C, and the resultant density was 99.3% and 99.5%.

3.4. Density testing and porosity

The density of the sintered samples was measured using a Shimadzu Scalerite AY120 scale with a density suspension and reporting system, which uses Archimedes' principle according to ASTM 311-08. Open porosity was determined according to ASTM 373-88. To facilitate the accurate determination of the open porosity, three weights were determined for each sample: dry mass (W1), wet mass (W2) and suspended mass (W3). Three samples from each batch of sintered samples were boiled in distilled water for 5 hours to eliminate bubbles from the sample surfaces. After boiling, the samples were weighed in air to obtain the wet mass (W2), and then suspended in distilled water to obtain the suspended mass (W3). After weighing, the samples were dried in a furnace at 100°C for 3 hours to eliminate all the moisture. Thereafter, the samples were then weighed in air to obtain the dry mass (W1). The volume percentage open porosity was determined from Equations 3.1 - 3.4:

$$\text{True volume} = \frac{W1-W3}{\rho w} \quad \text{.....Equation 3.1}$$

$$\text{True density} = \frac{W1-\rho w}{W1-W3} \quad \text{.....Equation 3.2}$$

$$\text{Bulk density} = \frac{W1-\rho w}{W2-W3} \quad \text{..... Equation 3.3}$$

$$\text{\% porosity} = \frac{W2-W1}{W2-W3} \times 100 \quad \text{..... Equation 3.4}$$

where:

*W*1 = dry weight (g),

*W*2 = wet weight (g),

*W*3 = suspended weight (g),

$\boldsymbol{\rho}_w$ = density of water (g/cm^3)

Theoretical density was determined the using Equation 3.5:

$$\boldsymbol{\rho}_{\text{Total}} = \sum\left(\frac{m_i}{\rho_x}\right)^{-1} \quad \text{..... Equation 3.5}$$

where ρ_{Total} =total density of mixtures, m_i = composition of mixtures and ρ_x = density of an individual composition.

3.5. Metallographic preparation

The samples were prepared for metallography using the following process. The samples were cut, ground and then polished to a mirror finish using successively finer diamond polishing pastes. The etched surface was checked for porosity after which the samples were etched using Murakami's reagent to reveal the microstructure.

3.5.1. Hot mounting

The primary purpose of mounting specimens is for convenience in handling specimens of difficult shapes or sizes during the subsequent steps of preparation and examination (Renqi *et al*., 2017). A secondary purpose is to protect and preserve sharp edges or surface defects during preparation. Specimens may also require mounting to accommodate various types of automatic devices used in laboratories or to facilitate placement on the microscope stage. An added benefit of mounting is the ease with which a mounted specimen can be identified by name, alloy number, or laboratory code number for storage by scribing the surface of the mount without damage to the specimen. Small specimens generally require mounting so that the specimen is supported in a stable medium for grinding and polishing. Samples were cut in half to show the cross-sectional area and surface area followed by mounting at a temperature of 200°C with a force of 3N (305.8g). Mounting for each sample took 7 minutes in a mounting press using Bakelite.

3.5.2. Grinding and polishing

The samples were ground using plates of 220 and 1200 µm grit with water as a lubricant (Figure 3.7 and Table 3.4). The 220 µm grit was used to level the surface and remove all the graphite that remained after the sintering process and 1200 µm was used to achieve a smooth

surface. The surface was then polished using Aka-Allegran 3 µm polycrystalline diamond suspension followed by an Aka-Poly 1 µm polycrystalline diamond suspension to obtain a mirror finish surface (Table 3.4). Polished samples were then washed with running water and etched using Murakami's reagent (10g $K_3[Fe(CN)_6]$ + 10g KOH + 100ml water) for 2-3 min followed by a rinse with running water (Table 3.4).

Table 3.4 Preparation method for metallographic analysis.

Process	Steps	Disk size and cloth	Lubricant	Speed (rpm)	Load (N)	Time (min)
Grinding	1	220	Water	300	60	7 - 10
	2	1200	water	300	60	7 - 10
Polishing	1	Aka-Allegran 3 µm	Aka-Poly + 3 µm	150	30	3 - 5
	2	Aka- Allegran 1 µm	Aka-Poly + 1 µm	150	30	3 - 5

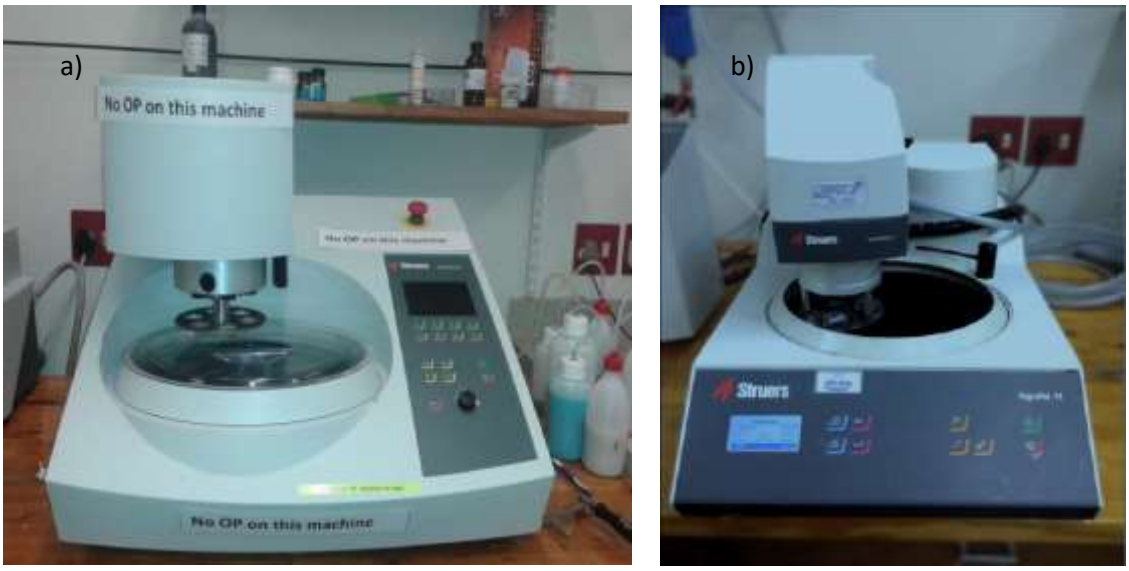

Figure 3.7 Photographs of (a) grinding, and (b) polishing machines from Struers.

The purpose of etching is to optically reveal microstructural features such as grains and phases. Etching selectively alters these microstructural features based on composition, stress, orientation and crystal structure, so that they can be differentiated.

3.6. Microstructural analysis

3.6.1. Light microscopy

The unetched and etched samples were analysed using an Olympus (GX41) light microscope. Light microscopy was used to check for possible scratches on the mirror surface of fully polished samples, and to observe features like porosity.

3.6.2. Scanning Election Microscopy (SEM)

The SEM was used to characterise the microstructure of the sintered alloys. Micrographs were taken using the scanning electron microscope using the back scattered electron mode, Zeiss FE-SEM (Gemini). Uniform sampling was done, and the overall 8 images were acquired by SEM in the backscattered mode. The accelerating voltage was fixed at 20 kV. Five to six analysis were done for each magnification 5.00 kx, 10.00 kx and 50.00 kx. Each contrast in a sample was thoroughly analysed and the overall composition of each sample was analysed at a low magnification.

3.6.3. Carbide grain size (d_c)

The grain size of the samples was calculated using a linear intercept method. To determine the average grain size, 35 lines were randomly drawn on the SEM micrographs. The number of carbide grains crossed by each line was counted and recorded, and the Heyn grain size was then calculated, using Equation 3.6.

$$d_c = L/N \quad \text{..... Equation 3.6}$$

where:

L = length of the intercept line, and

N = the number of carbide grains crossed.

3.6.4. Carbide contiguity (C)

Contiguity is a measure of the degree of contact between carbide grains, and can be calculated using Equation 3.7:

$$C = \frac{2(N)_{\alpha\alpha}}{2(N)_{\alpha\alpha}+2(N)_{\alpha\beta}} \quad \text{……Equation 3.7}$$

where:

C = contiguity,

$N_{\alpha\alpha}$ = average number of intercepts per unit length of test lines with the traces of carbide-carbide grain boundaries, and

$N_{\alpha\beta}$ = average number of intercepts in carbide- binder interface.

3.6.5. Binder mean free path (λ_{Co})

The mean binder free path is described as the thickness of the cobalt layer and depends on the particle size and cobalt content. The mean free path is calculated using the experimentally determined parameters in Equation 3.8 Exner, H. and Fischmeister, F. (1966).

$$d_{Co} = \frac{1}{1+C}\ d_{WC}\ \frac{V_{Co}}{V_{WC}} \quad \text{……..Equation 3.8}$$

where:

d_{Co} = mean binder free path

V_{WC} = volume fraction of carbide phase, and

C = contiguity of the carbide phase.

The binder volume fraction was determined from Equation 3.9:

$$V_{Co} = \frac{wt\ \%\ Co}{Density\ of\ Co}\ X\ \frac{Density\ of\ Sample}{Mass\ of\ Sample} \quad \text{…….. Equation 3.9}$$

3.7. Mechanical properties

3.7.1. Vickers hardness tests

The Vickers hardness (HV) was measured on all samples using a 30 kg load and three indentations per sample. The average hardness per sample was calculated to obtain the overall hardness of the material. The crack lengths from the tip of each indentation were measured to calculate the fracture toughness (K_{IC}) of the material using the Palmqvist equation (1962). Light microscopy picture scaling algorithms that are embedded within the microscope software were used to measure crack lengths created during hardness testing to calculate the fracture toughness.

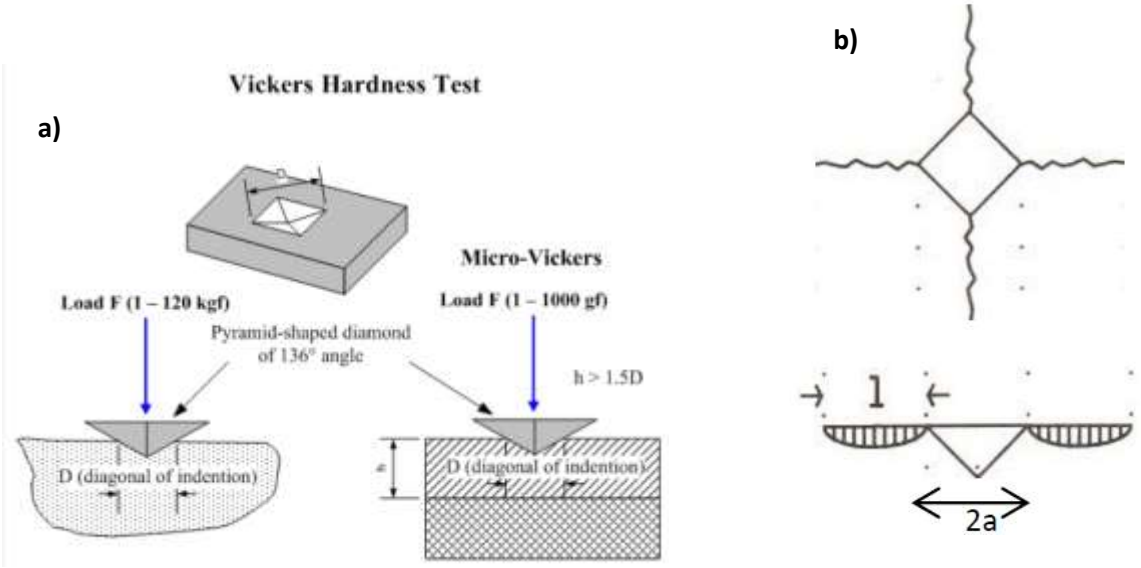

Figure 3.8 (a) Vickers Diamond Pyramid Hardness Indenter and (b) indentation showing crack geometry of Palmqvist cracks (Palmqvist, 1962).

In performing the hardness test, the load was applied smoothly without impact and held in contact with the sample surface for 10 to 15 seconds as shown in Figure 3.8. After removal of the load, both impression diagonals were measured, and the average value was used to calculate HV by means of Equation 3.10:

$$HV = \frac{2L.Sin\left(\frac{\alpha}{2}\right)}{d^2} = \frac{1.8544L}{d^2} \quad \text{..... Equation 3.10}$$

where:

d = mean diagonal (mm),

L = Load (kgf),

α = face angle (136°).

In general, HV is determined by referring to tables of HV for each possible load and diagonal measurement. Most equipment manufacturers supply a set of tables with the instrument, and these tables are also found in ASTM Specification E92.

3.7.2. Fracture toughness tests

Fracture toughness was calculated using the Palmqvist crack lengths from the Vickers hardness indentations (Figure 3.8 b) and the length calculation algorithm software in the Olympus (GX41) light microscope, Equation 3.11:

$$K_{IC} = 0.15x \left(\frac{HV_{30}}{\sum l}\right)^{\frac{1}{2}} \quad \text{..... Equation 3.11}$$

where:

K_{IC} = fracture toughness ($MPa.m^{1/2}$),

HV_{30} = hardness, and

l = crack length (mm).

Chapter Four

4. Results

This chapter focuses on the results obtained from the different techniques and compared them against each other.

4.1. Starting powder morphology

The images of the starting powders are shown in Figure 4.1. The as-received WC powders had different shapes and size distributions which are further specified below.

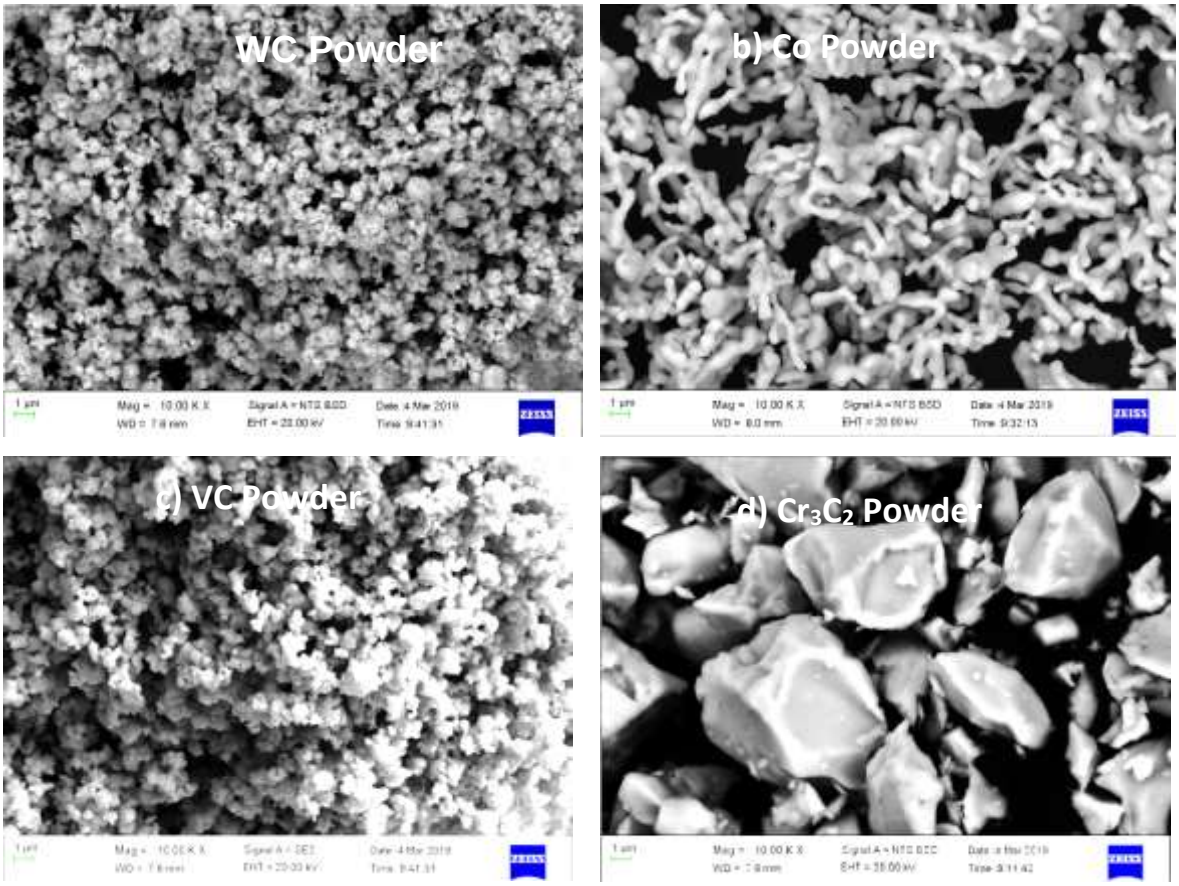

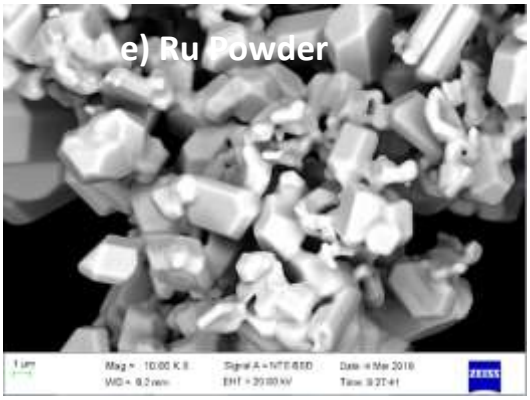

Figure 4.1 SEM-BSE images of as-received a) WC, b) Co, c) VC, d) Cr_3C_2 and e) Ru powder showing different morphologies and particle sizes.

The as-received VC powder had agglomerated particles that were fine and round, while the Cr_3C_2 and Ru powder had angular particles that were different in size from the Ru powder which was shiny and bright in colour with smooth surfaces. The XRD patterns for the as-received powders are shown in Figures 4.2 - 4.6. The Co particles were elongated and irregular in shape and only two peaks were observed for Cr_3C_2 between 2θ = 45° and 50°, Figure 4.3.

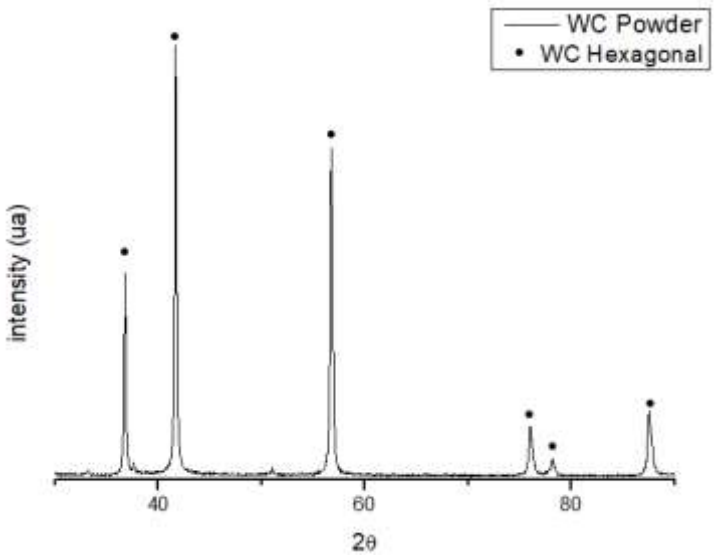

Figure 4.2 X-ray diffraction pattern of the as-received WC powder.

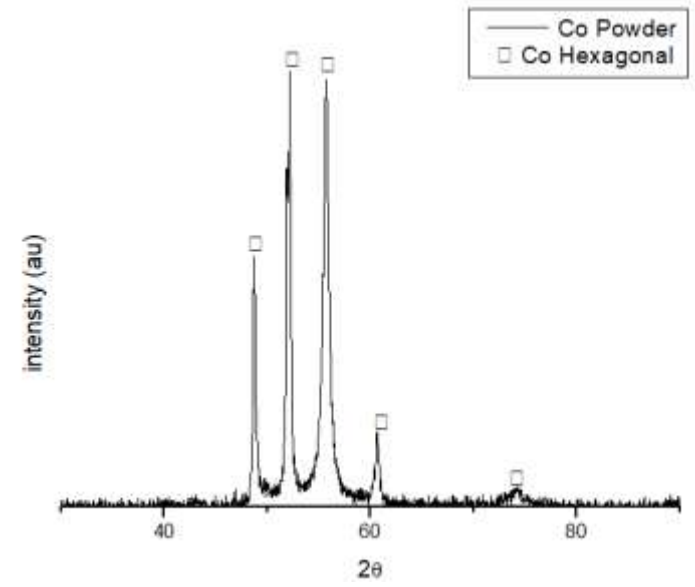

Figure 4.3 X-ray diffraction pattern of the as-received Co powder.

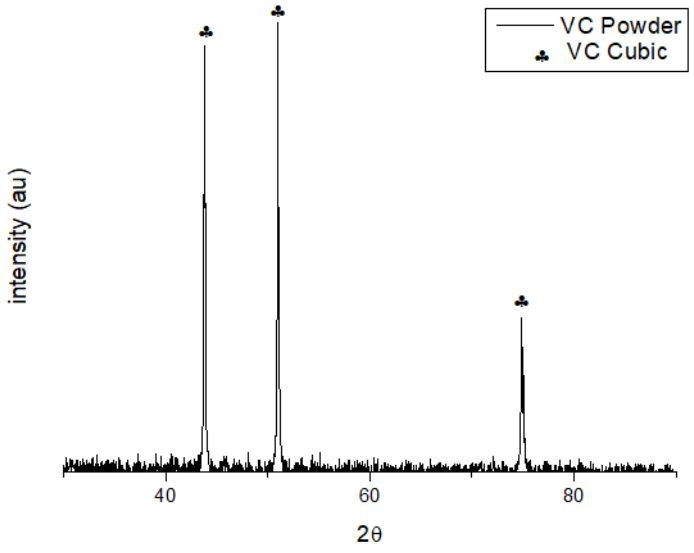

Figure 4.4 X-ray diffraction pattern of the as-received VC powder.

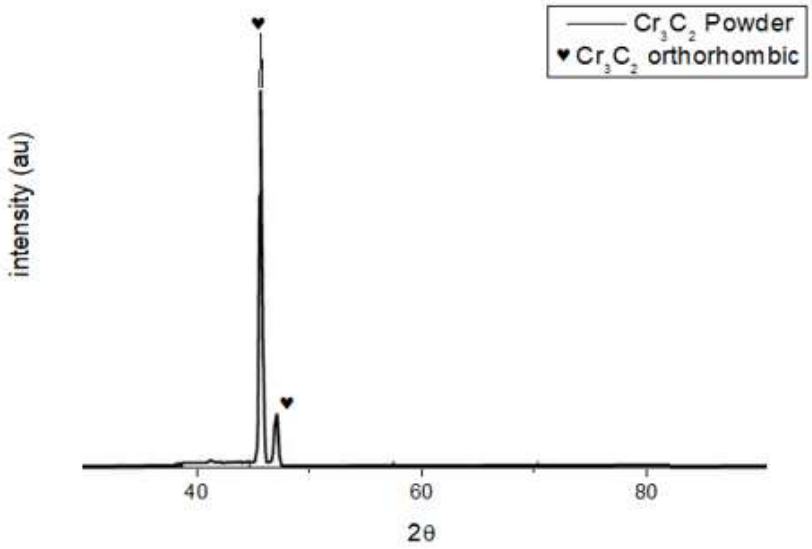

Figure 4.5 X-ray diffraction pattern of the as-received Cr_3C_2 powder.

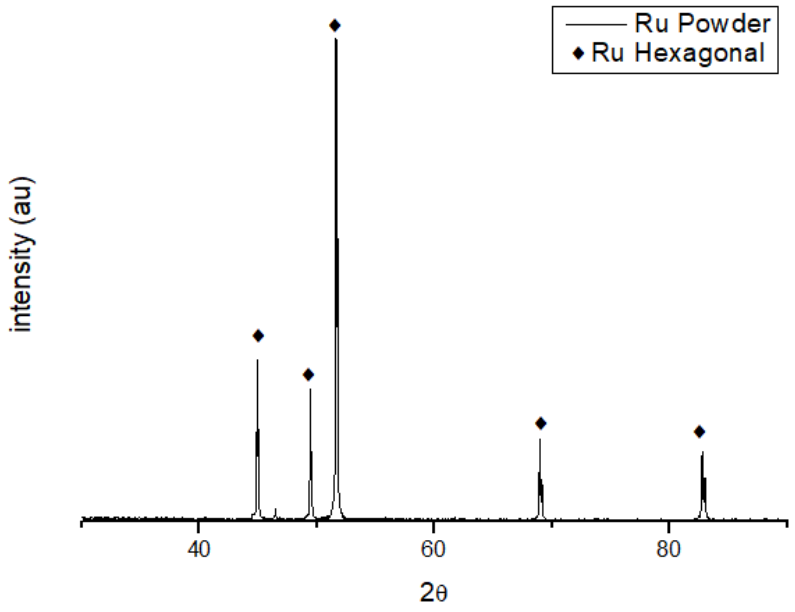

Figure 4.6 X-ray diffraction pattern of the as-received Ru powder.

4.2. Particle size analysis

The particle size distribution graphs for the as-received powders are shown in Figures 4.7 - 4.11 with $d_{0.1}$, $d_{0.5}$ and $d_{0.9}$. The $d_{0.1}$, $d_{0.5}$ and $d_{0.9}$ particle size values indicate the percentage of particles in the sample analyses that fall within 10%, 50% and 90%. The as-received WC powder had an average particle size of 0.15 µm with the small peak at 2 µm that shows that WC was agglomerated. The cobalt powder particle average size was 8 µm with a slight agglomeration peak at 80 µm. Similar results were observed for VC (average 1.9 µm) and Cr_3C_2 (average 30 µm). The ruthenium powder displayed a different pattern with a wide and double peak at 20 µm. This was due to ruthenium being a mixture of small and large particles (Figure 4.11). The particle size distribution curve (PSDC) of Cr_3C_2 displayed similar results to the Ru powder. Table 4.1 shows the particle sizes of all the starting powders.

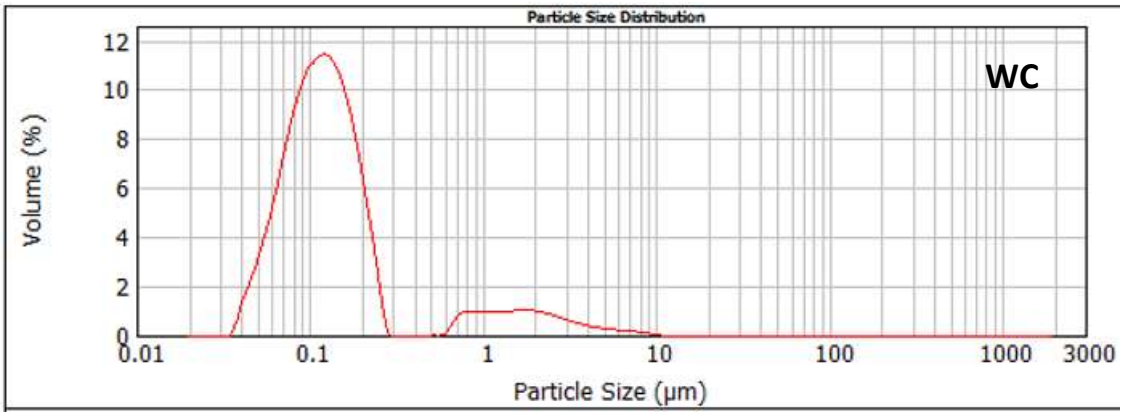

Figure 4.7 Particle size of the as-received WC powder.

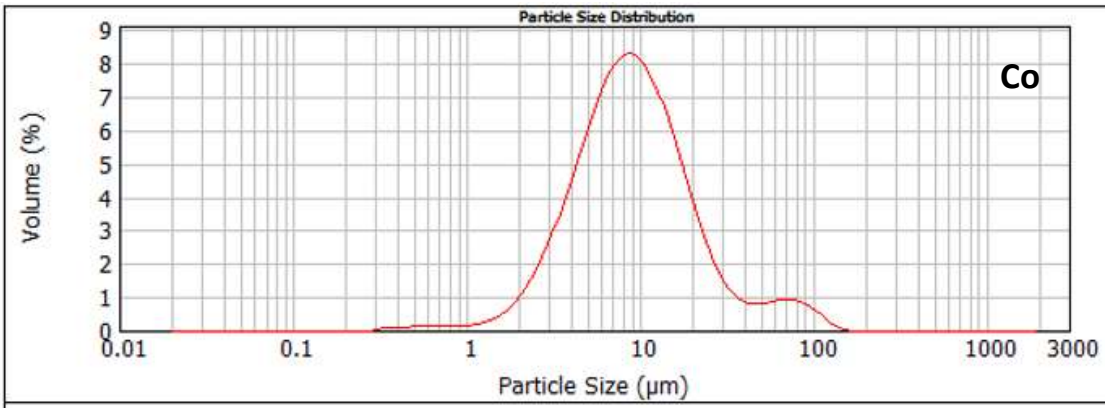

Figure 4.8 Particle size of the as-received Co powder.

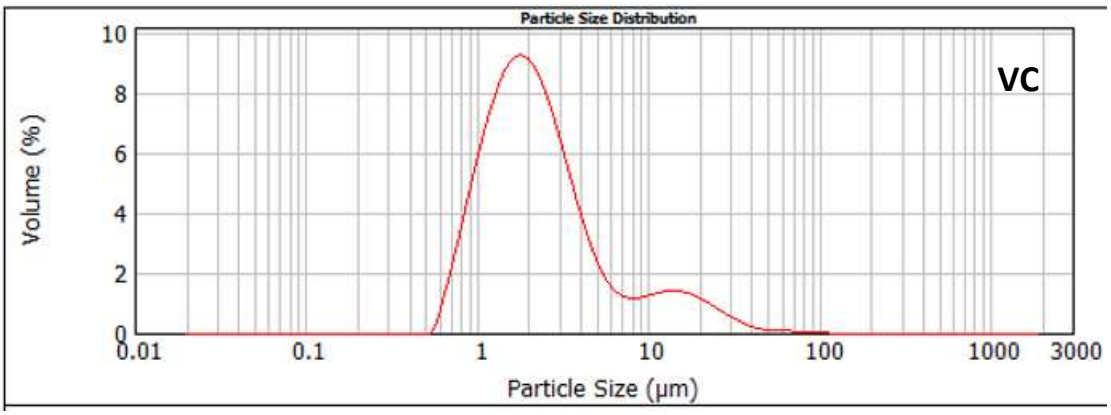

Figure 4.9 Particle size of the as-received VC powder.

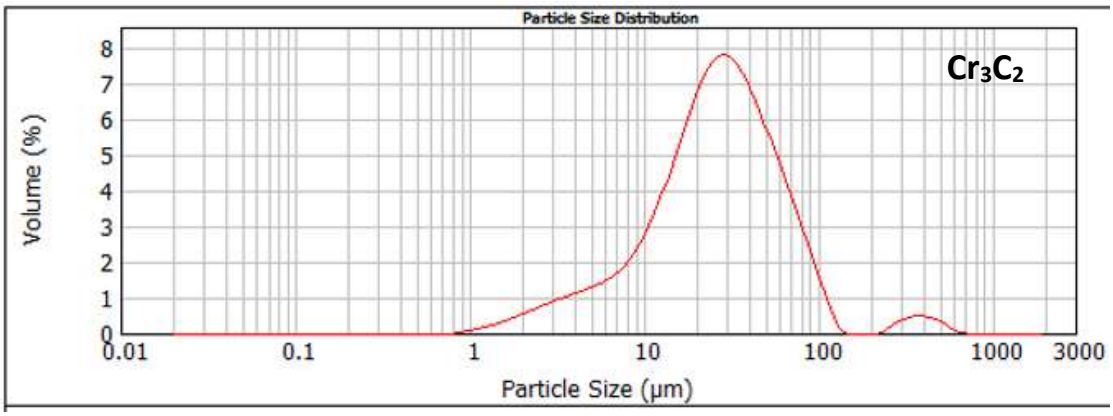

Figure 4.10 Particle size of the as-received Cr_3C_2 powder.

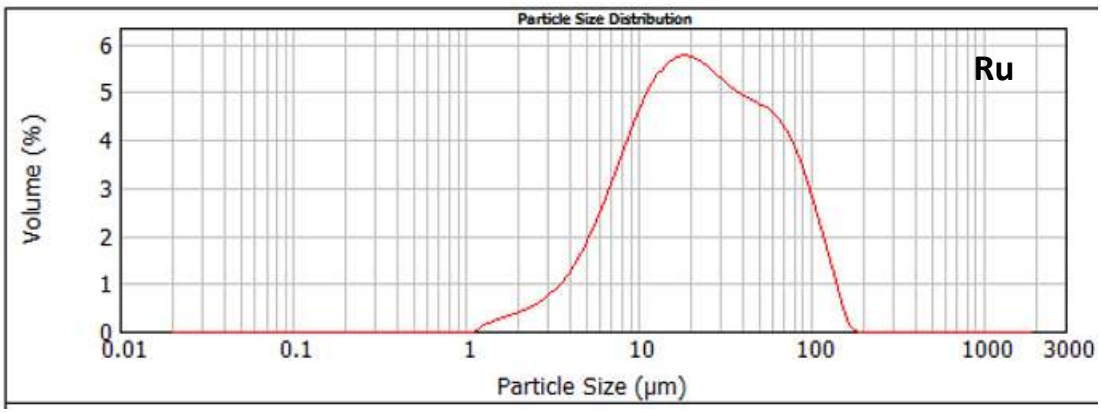

Figure 4.11 Particle size of the as-received Ru powder.

Table 4.1 Measured average as-received particle sizes (µm).

Powder	$d_{0.1}$	$d_{0.5}$	$d_{0.9}$	Mean
WC	0.06 ± 0.01	0.12 ± 0.12	0.84 ± 0.34	0.15 ± 0.02
Co	3.46 ± 0.06	8.96 ± 0.54	25.75 ± 1.03	8 ± 1.02
VC	0.98 ± 0.28	2.06 ± 0.09	9.47 ± 0.12	1.9 ± 1.57
Cr_3C_2	6.94 ± 1.05	26.91 ± 1.06	70.81 ± 2.78	30 ± 2.15
Ru	6.46 ± 0.98	23.04 ± 1.48	80.76 ± 2.45	20 ± 2.04

4.3. Characterisation of the mixed powders

4.3.1. Powder morphology

The morphologies of the powder mixtures were determined using SEM-BSE. The images were also used to confirm the particle size analysis results. The image of the milled WC-10Co powder is shown in Figure 4.12.

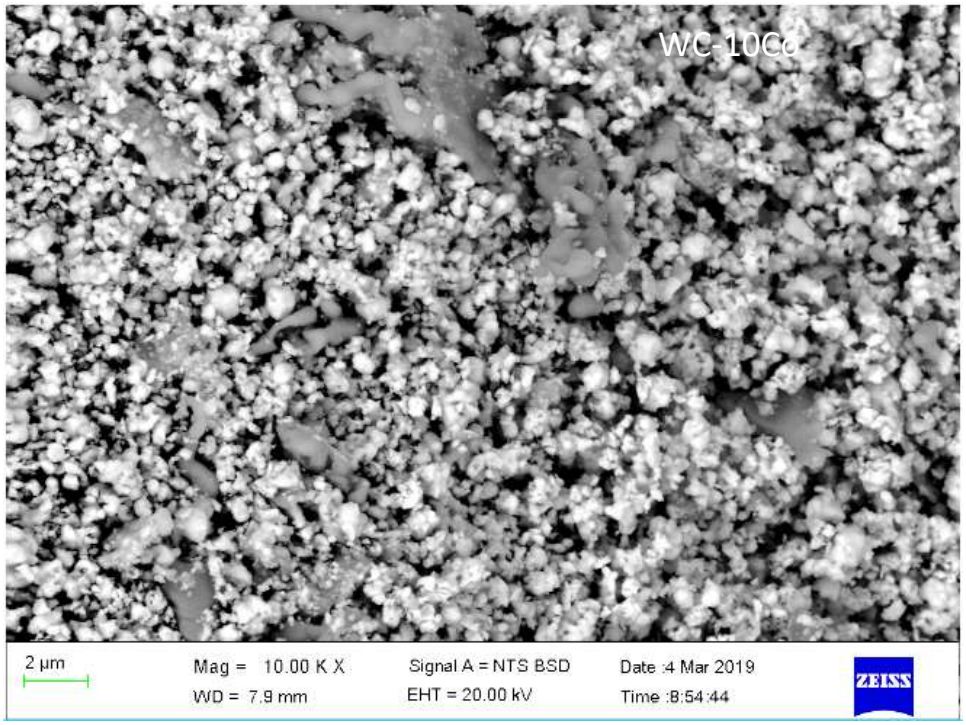

Figure 4.12 SEM-BSE image of WC-10Co milled powder, showing Co (dark contrast) and WC (light contrast).

4.4. Particle size analysis of the powder mixtures

The size distributions of the powder mixtures of the samples are shown in Figures 4.13 – 4.20 with $d_{0.1}$, $d_{0.5}$ and $d_{0.9}$ given in Table 4.2 with their average values that were used to describe the particle size distribution. The particle size distributions of the mixed powders (Figures 4.13 to 4.20) have a second peak, starting around 1 µm and extending to around 3 µm, which is due to agglomeration of fine powders as well as the large Co particles still present in the base powder.

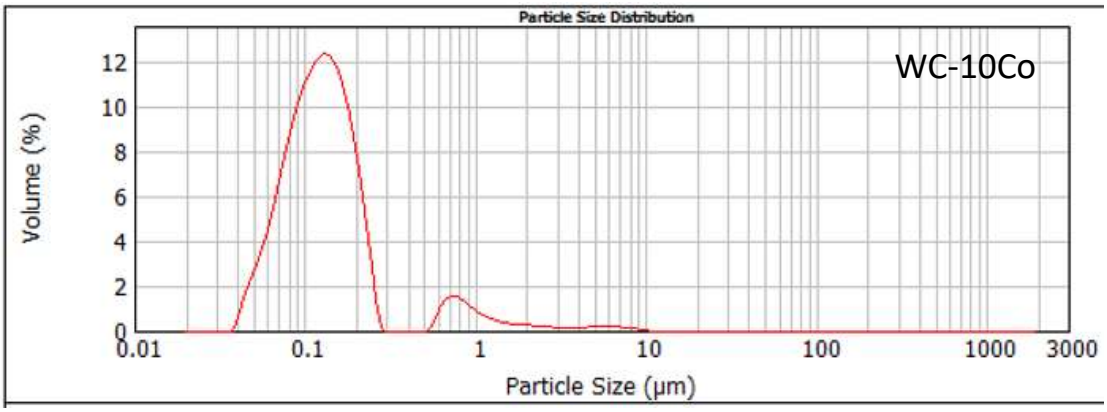

Figure 4.13 Particle size distribution of WC-10Co.

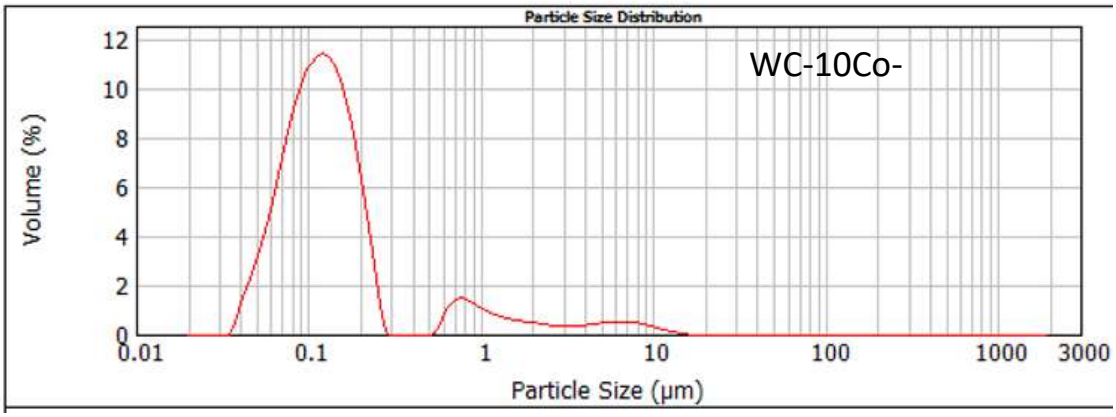

Figure 4.14 Particle size distribution of WC-10Co-0.2VC.

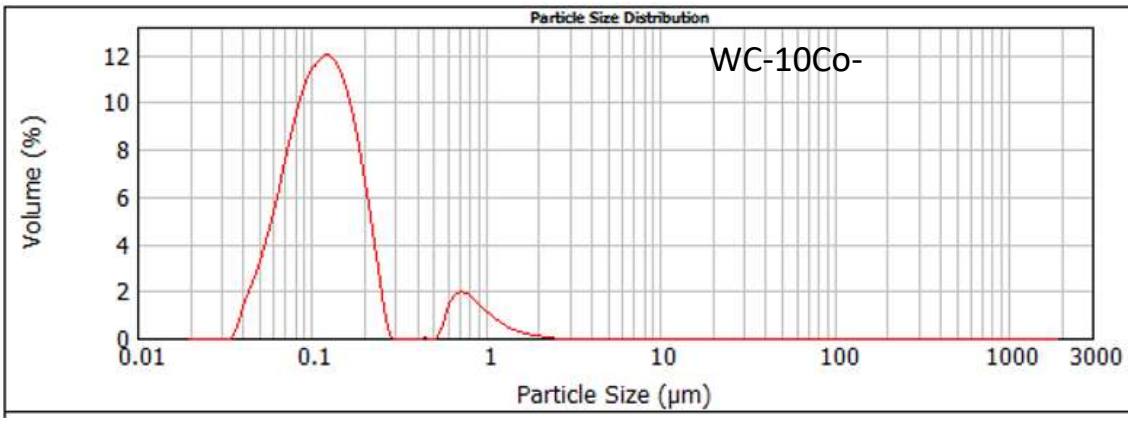

Figure 4.15 Particle size distribution of WC-10Co-0.2Cr_3C_2.

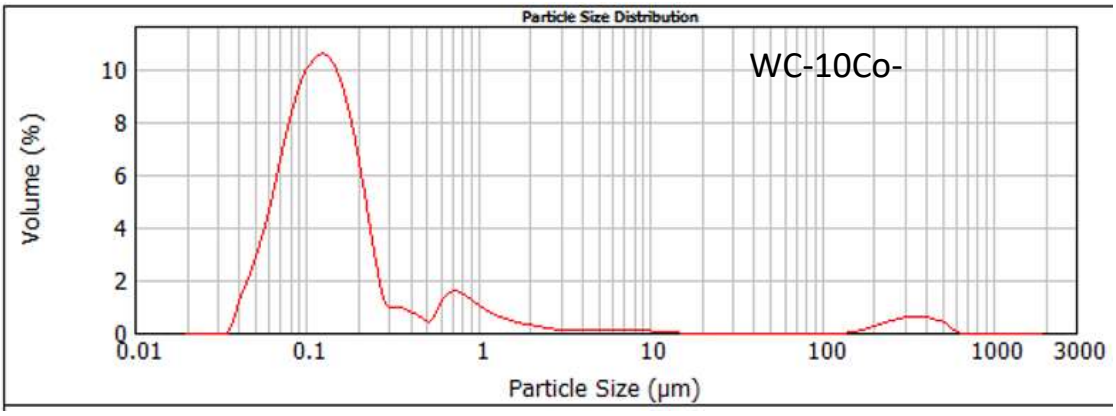

Figure 4.16 Particle size distribution of WC-10Co-0.2Ru.

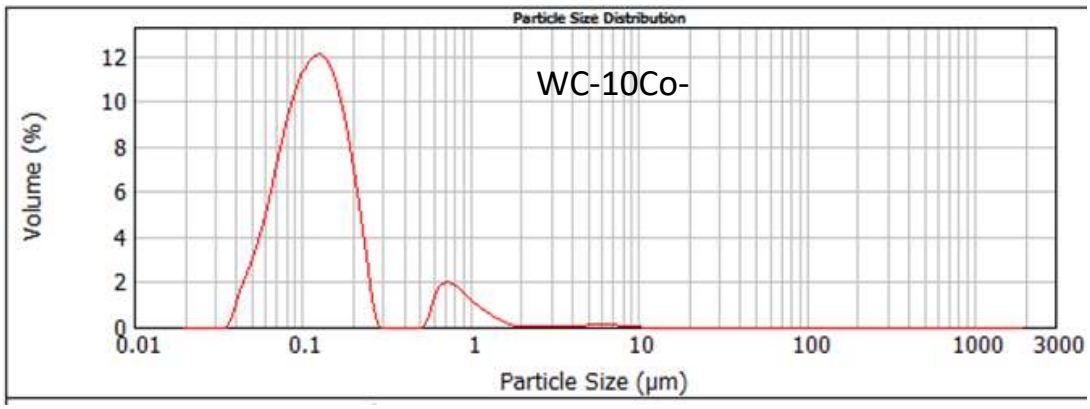

Figure 4.17 Particle size distribution of WC-10Co-0.2VC-0.2Cr_3C_2.

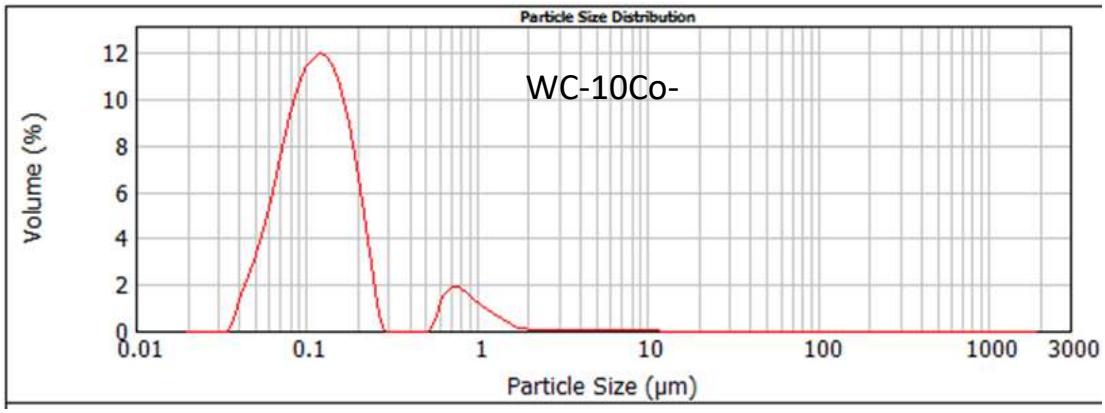

Figure 4.18 Particle size distribution of WC-10Co-0.2Cr_3C_2-0.2Ru.

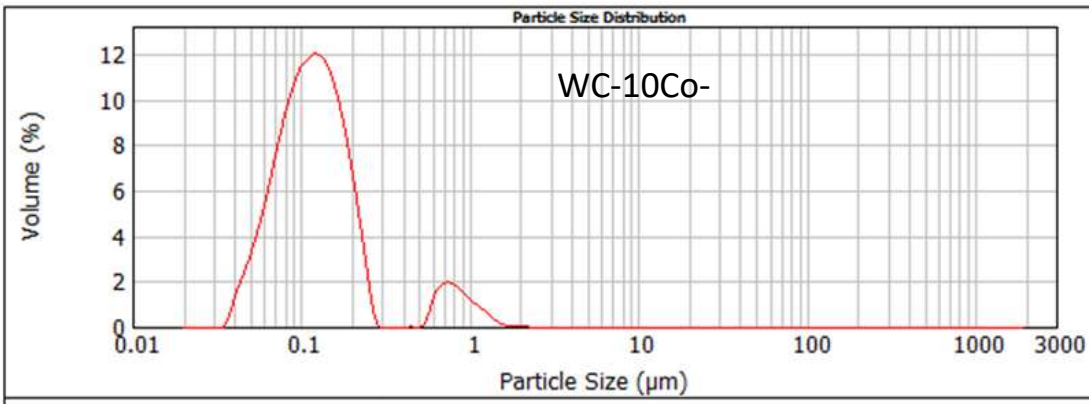

Figure 4.19 Particle size distribution of WC-10Co-VC-0.2Ru.

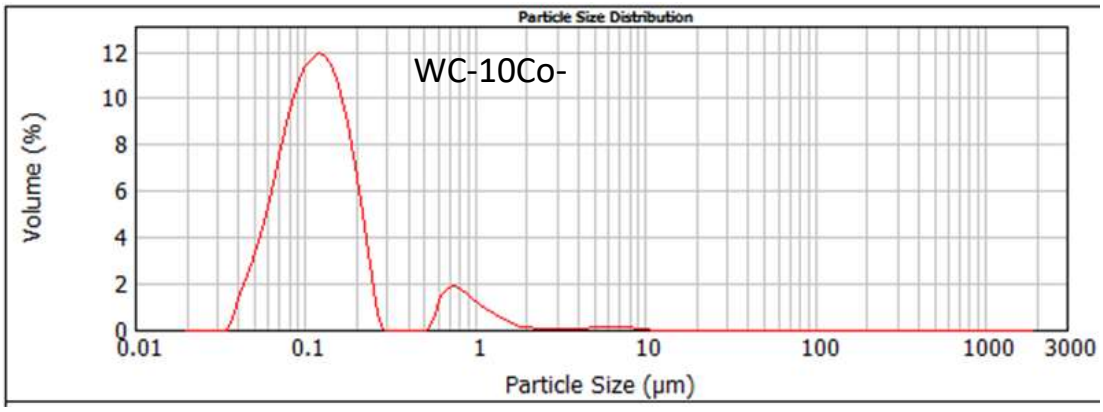

Figure 4.20 Particle size distribution of WC-10Co-0.2VC-0.2Cr_3C_2-0.2Ru.

Table 4.2 Average particle sizes of the alloys.

Powders	$d_{0.1}$	$d_{0.5}$	$d_{0.9}$	Average
WC-10Co = base	0.07 ± 0.01	0.13 ± 0.02	0.24 ± 0.02	0.15 ± 0.06
base + 0.2VC	0.06 ± 0.01	0.12 ± 0.08	0.79 ± 0.07	0.32 ± 0.04
base + 0.2Cr_3C_2	0.06 ± 0.01	0.12 ± 0.04	0.23 ± 0.06	0.14 ± 0.05
base + 0.2Ru	0.07 ± 0.02	0.13 ± 0.06	0.76 ± 0.03	0.32 ± 0.06
base + 0.2VC+0.2Cr_3C_2	0.06 ± 0.01	0.12 ± 0.02	0.24 ± 0.02	0.14 ± 0.04
base + 0.2Cr3C2+0.2Ru	0.06 ± 0.02	0.12 ± 0.03	0.23 ± 0.01	0.14 ± 0.03
base + 0.2V+-0.2Ru	0.06 ± 0.02	0.12 ± 0.03	0.24 ± 0.01	0.14 ± 0.03
base + 0.2VC+0.2 Cr_3C_2 + 0.2Ru	0.06 ± 0.01	0.12 ± 0.03	0.24 ± 0.02	0.14 ± 0.03

4.5. Cemented carbide alloy characterisation

4.5.1 Microstructure analysis

The microstructures of the areas analysed by EDX for the base WC-10Co powders are given in Figures 4.21 – 4.22. Figure 4.21 shows the as-received Co binder and WC powders before milling, and Figure 4.22 shows the SEM micrograph of WC-10wt%Co after milling.

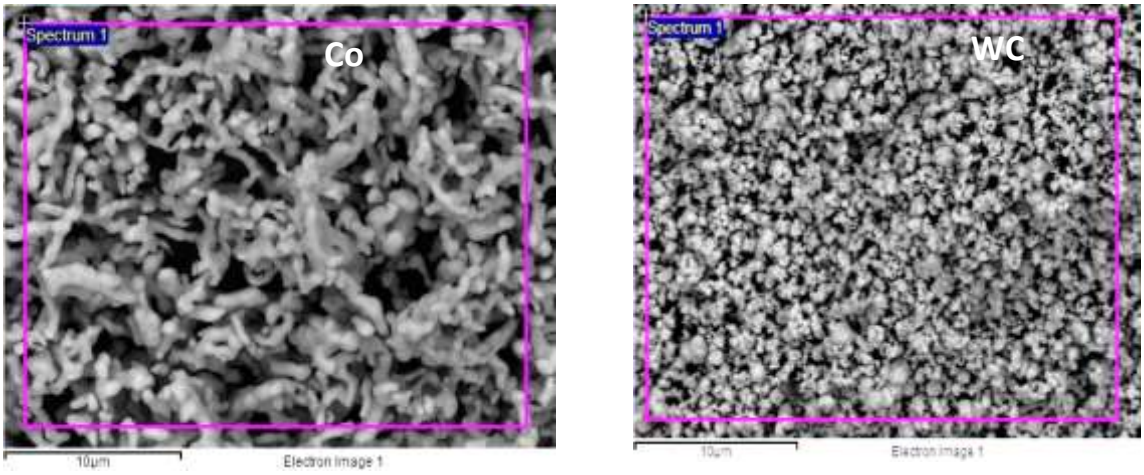

Figure 4.21 SEM-BSE images of Co and WC powders showing where a typical EDX analysis was done.

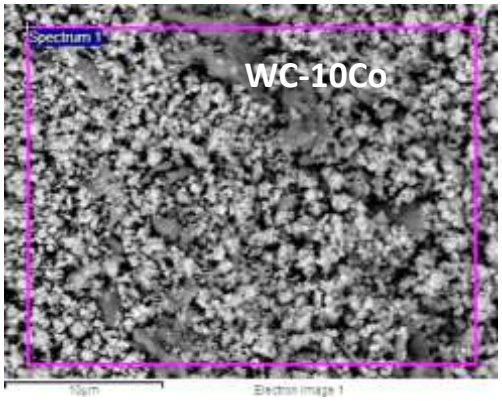

Figure 4.22 SEM-BSE image of the mixed and milled WC-10Co powder showing where a typical EDX analysis was done.

Table 4.3 SEM-EDX analysis of WC, Co and base WC-10Co powders.

Elements	WC-10Co (wt%)	Co (wt%)	WC (wt%)
W	75.2 ± 2.9	-	84.6 ± 2.8
Co	9.6 ± 0.7	98.6 ± 1.9	-
C	15.3 ± 0.7	-	12.9 ± 0.8
O	-	1.4 ± 0.2	2.5 ± 0.3

The micrographs of the WC-10Co powders sintered at different temperatures are shown in Figure 4.23. The lighter areas are the WC grains, and the dark areas are the cobalt binder. In the images of the samples sintered at 1000°C and 1150°C the black areas are porosity.

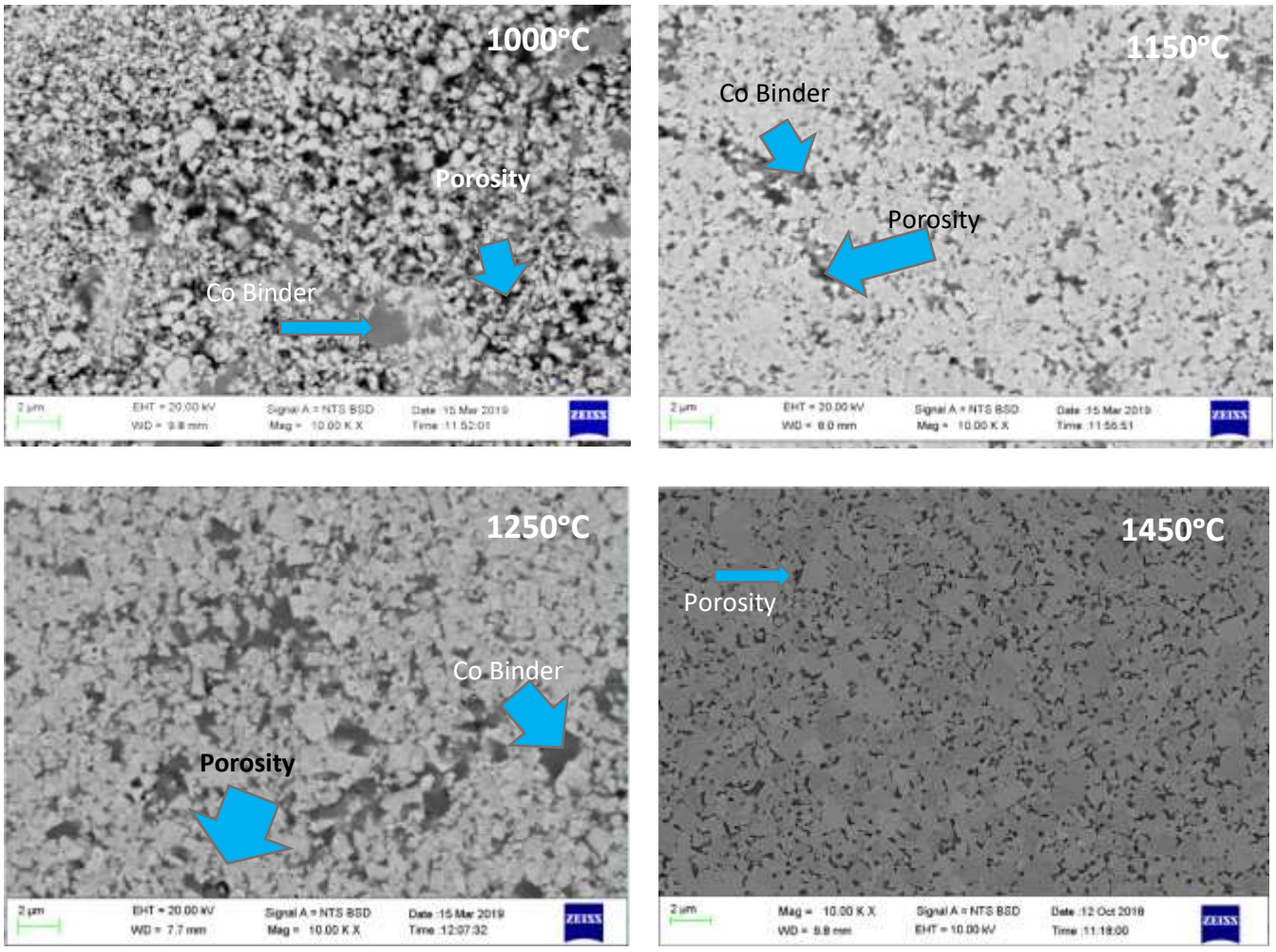

Figure 4.23 SEM-BSE images of WC-10Co sintered at 1000°C, 1150°C, 1250°C and 1450°C with a holding time of 5 minutes and a pressure of 50 MPa: WC (light contrast), Co (dark contrast).

Microstructures of the samples sintered for 8 minutes are shown in Figure 4.24. Increasing sintering time improved density by 61.6% (9.18 g/cm^3 to 14.88 g/cm^3) and reduced the grain size by 63.2% (0.87 µm to 0.55 µm) (Tables 4.4 and 4.5), with 1450°C having larger grain sizes. There were still spherical particles that were not properly sintered for the WC-10Co sintered at 1000°C. This was shown by its relative densification of 63%. Samples sintered at 1150°C and 1250°C had smaller grain sizes (between 0.76 µm and 0.87 µm) with good cobalt binder distribution, but their density could be improved to at least >99% relative density.

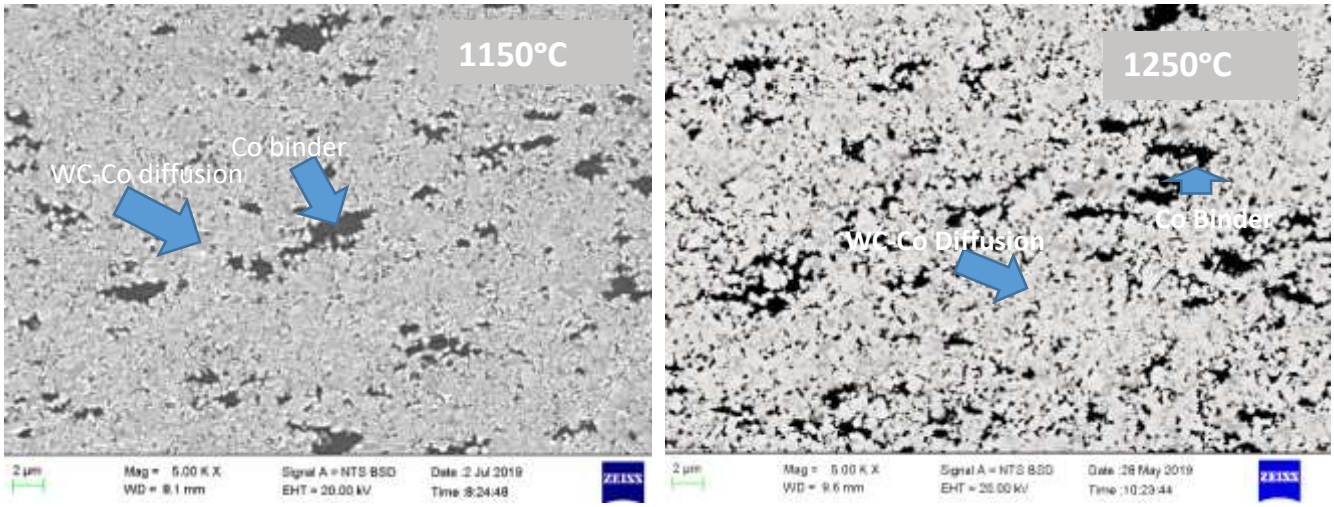

Figure 4.24 SEM-BSE images of WC-10Co sintered at 1150°C and 1250°C with a holding time of 8 minutes and a pressure of 50 MPa: Co (dark contrast) and WC (light contrast).

Figure 4.24 shows samples with some large pools of Co, especially for the sample sintered at 1150°C. The sample sintered at 1250°C had a better Co distribution, but the WC grains were larger, and both good phase distribution and fine WC grain size are needed. This shows that temperature is one of the parameters that improves sintering and distribution of carbides, cobalt distribution and grain size are important for good microstructures.

4.6. Mechanical properties

4.6.1. Hardness tests

The WC-10Co sample sintered at 1000°C had a low hardness (183 ± 5 HV_{30}) because it was not properly sintered (Table 4.4). The WC-10Co base materials that showed higher hardness values were sintered at 1150°C (1526 ± 8 HV_{30}) and 1250°C (1543 ± 7 HV_{30}). Fracture toughness of the base sample sintered at 1000°C was not measurable because the cracks around the hardness indentation were not visible. Increased sintering temperature increased the hardness and thus decreased fracture toughness (Table 4.4). The mechanical properties of the alloys sintered for 8 minutes are given in Table 4.5 and show a significant increase in relative density and hardness.

When the sintering time was increased to 8 minutes, the density of the base alloy increased from 96% to 99.3% for the alloy sintered at 1150°C, and from 97% to 99.5% for the alloy sintered at 1250°C. Material sintered at 1450°C had 102.4% relative density was likely due to the binder phase evaporating off at the sintering temperature and thus giving a higher WC content to the final material, hence an apparent above 100% density for the nominal compositions. There was no need to do further samples at 1000°C and 1450°C as these sintering temperatures gave less good results.

Table 4.4 Mechanical properties of the WC-10Co alloys (5 minutes dwell-time).

Sintering temperature (°C)	**Theoretical density (g/cm^3)**	**Experimental density (g/cm^3)**	**Relative density (%)**	**Hardness (HV_{30})**	**Fracture toughness, K_{1c} ($MPa.m^{1/2}$)**	**Average grain size (μm)**
1000	14.53	9.18	63.2	183 ± 5	Not measurable	Not measurable
1150	14.53	13.94	96	1526 ± 8	9.81 ± 0.99	0.87 ± 0.05
1250	14.53	14.08	97	1543 ± 7	9.61 ± 0.87	0.76 ± 0.03
1450	14.53	14.88	102.4	1586 ± 9	9.64 ± 0.96	0.55 ± 0.03

Table 4.5 Mechanical properties of the sintered WC-10Co samples (8-minute dwell-time).

Sintering temperature (°C)	**Theoretical density (g/cm^3)**	**Experimental density (g/cm^3)**	**Relative density (%)**	**Hardness (HV_{30})**	**Fracture Toughness K_{1c} ($MPa{\cdot}m^{1/2}$)**	**Average grain size (μm)**
1150	14.53	14.43	99.3	1564 ± 35	21.9 ± 1.04	0.52 ± 0.03
1250	14.53	14.46	99.5	1523 ± 38	9.80 ± 0.96	0.86 ± 0.04

4.7. Densification of cemented carbide alloys

4.7.1. Density of the alloys

The densities of the alloys sintered at 1150°C for 8 minutes are given in Table 4.6. The relative density of alloys was in the expected range (>99%). The aim of the project was to

determine the effectiveness of additives in 0.2%, optimise sintering temperature, time and pressure was to obtain the best single temperature, time and pressure to use when making samples with the additives. Since the sintering temperature of 1150°C gave the best overall mechanical properties it was selected, even though it had some Co pools. However, having the Co pools meant that the effect of additives on Co pool reduction could be ascertained.

Table 4.6 Densities of sintered alloys at 1150°C for 8 minutes dwell time and 50 MPa.

Sample	Alloy Composition	Theoretical Density (g/cm^3)	Experimental Density (g/cm^3)	Relative Density (%)
1	**WC-10Co**	14.53	14.43	99.3
2	**WC-10Co-0.2VC**	14.48	14.33	99.0
3	**WC-10Co-0.2Cr_3C_2**	14.49	14.37	99.2
4	**WC-10Co-0.2Ru**	14.52	14.43	99.4
5	**WC-10Co-0.2VC-0.2Cr_3C_2**	14.45	14.32	99.1
6	**WC-10Co-0.2Cr_3C_2-0.2Ru**	14.49	14.39	99.3
7	**WC-10Co-0.2VC-0.2Ru**	14.48	14.33	99.0
8	**WC-10Co-0.2VC-0.2Cr_3C_2-0.2Ru**	14.44	14.31	99.1

4.8. Microstructural characterisation

4.8.1. SEM analysis

The images of the un-etched samples are shown in Figure 4.26 and the etched samples are shown in Figure 4.27. The un-etched micrographs clearly show the Co pools, and the etched micrographs show three different contrasts indicating different phases were present. The Co pools became smaller when the grain growth inhibitors were added to the base composition. The SEM-EDX analyses of the cemented carbide alloys are shown in Table 4.7, and some of the errors were below the accuracy capabilities of the instrument. However, given that the grains were fine, it was difficult to obtain good analyses, and signals from other phases must have been collected as well. This is shown by the high amount of W that occurred in every phase, not just in the light WC phase, and the high amounts of Co which appear in the light phase. Table 4.8 shows the mean grain size, WC contiguity and binder mean free path for samples sintered at 1150°C, for 8 minutes at 50 MPa.

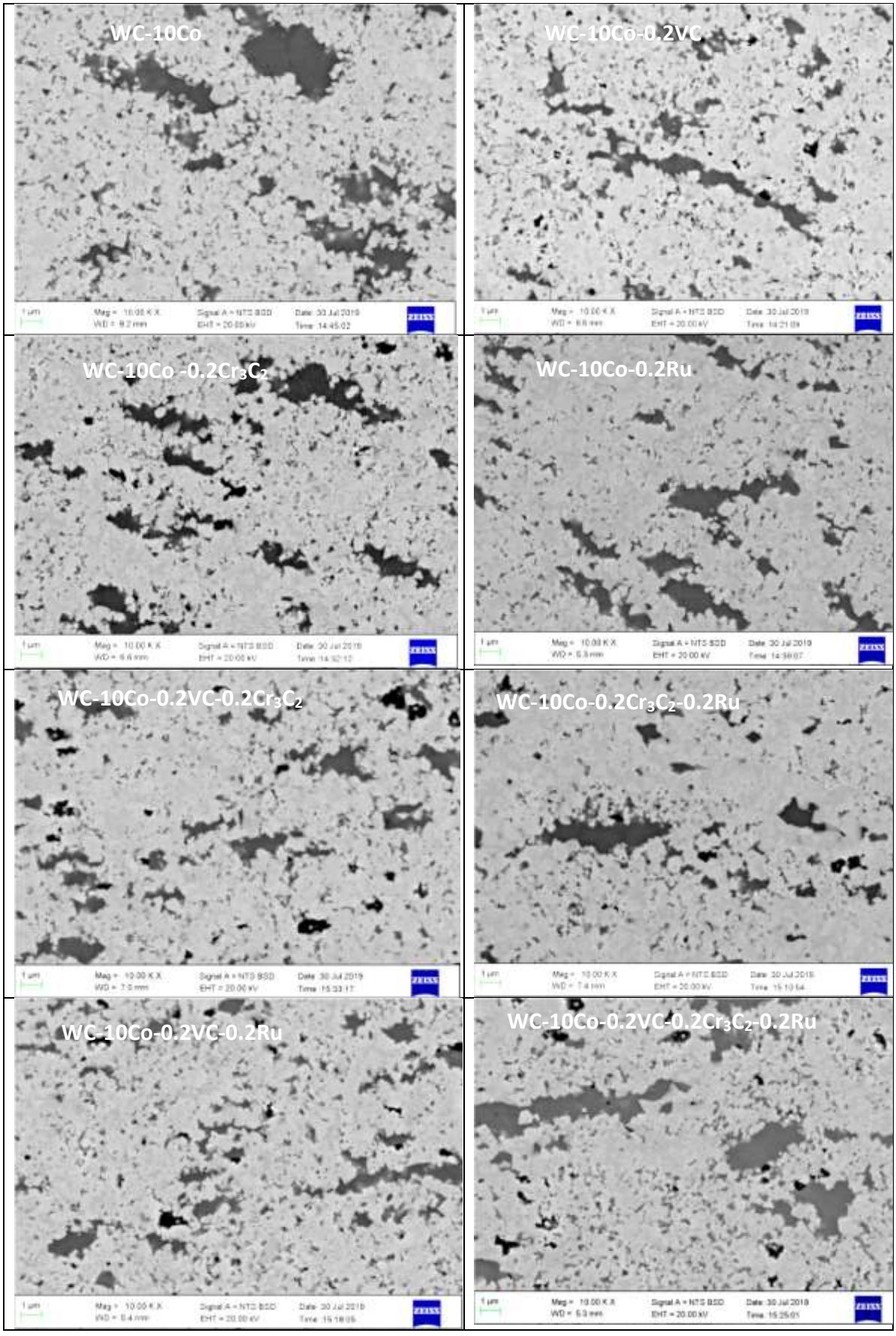

Figure 4.25 SEM-BSE images of un-etched WC-10Co alloys sintered at 1150°C, for 8 minutes at 50 MPa with 0.2 – 0.6 wt% additives: WC (light contrast), Co (dark contrast).

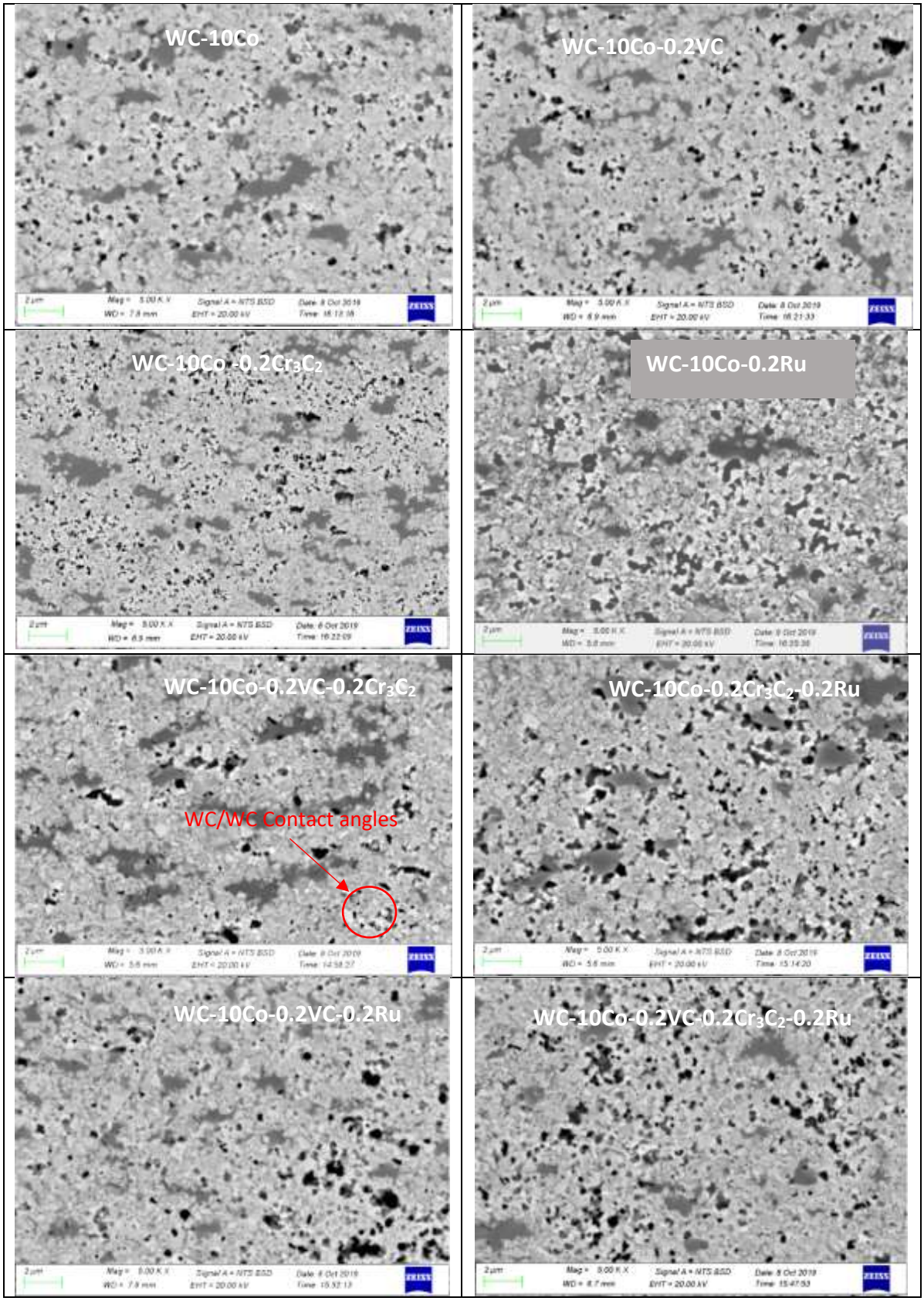

Figure 4.26 SEM-BSE images of etched WC-10Co alloys sintered at 1150°C, for 8 minutes at 50 MPa showing WC (light contrast) and Co (dark contrast).

Table 4.7 EDX analyses of the cemented carbide alloys.

Additives	Contrast	Composition (wt%)							Total
		W	C	Co	V	Cr	Ru	O	
Base alloy (WC-10Co)	Light	82.7±11.2	4.3±0.4	13±4.2	-	-	-	-	100
	Dark	21.1±2.4	16.3±3.1	62.6±15.2	-	-	-	-	100
	Overall	78.5±22.1	10.8±5.2	10.7±1.4	-	-	-	-	100
0.2 VC	Light	82.7 ± 0.3	14.3 ± 0.9	3.0 ± 10	-	-	-	-	100
	Medium	74.1±11.3	14.3±2.8	11.3±8.5	0.4±0.02	-	-	-	100
	Dark	21.6 ± 1.8	16.4 ± 1.8	61.9 ± 0.5	-	-	-	-	100
	Overall	72.7±21.3	16.3±9.3	10.8±3.7	0.2±0.04	-	-	-	100
0.2 Cr_3C_2	Light	77.3±0.9	14.9±2.1	7.8±2.0	-		-		100
	Medium	76.2±5.0	15.5±2.1	8.3±2.0	-	-	-	-	100
	Dark	28.3±2.4	13.5±0.8	38.2±2.3	-	19.9±1.8	-	-	100
	Overall	73.6±12.4	14.8±4.5	11.3±2.4	-	0.31±0.2	-	-	100
0.2 Ru	Light	97.5±3.2	15.2±1.5	5.5±1.4	-	-	-	-	100
	Medium	76±0.8	15±1.8	9.1±1.1	-	-	-	-	100
	Dark	43.2±13	12.8±3.6	43.4±11.2	-	-	0.6±0.2		100
	Overall	75.2±2.6	14±2.3	10.1±2.5	-	-	0.7±0.5	-	100
0.2 VC + 0.2 Cr_3C_2	Light	80.7±1.7	15.1±1.0	4.2±0.7	-	-	-	-	100
	Medium	76.1±6.0	14.3±2.7	8.7±2.3	-	0.9±0.0	-	-	100
	Dark	41.4±5.4	11.3±1.3	44.8±3.1	1.4±1.2	1.0±0.5	-	-	100

Additives	Contrast	Composition (wt%)							Total
		W	C	Co	V	Cr	Ru	O	
	Overall	72.6±2.8	16.7±1.1	10.0±2.2	0.5±0.1	0.4±0.09	-	-	100
0.2 Cr_3C_2 + 0.2 Ru	**Light**	64.2±2.5	28.2±1.7	3.7±1.3	-	-	-	3.9±0.0	100
	Medium	53.6±8.7	30.5±1.9	15.8±7.2	-	-	-	-	100
	Dark	25.5±3.3	21.6±2.5	40.8±6.6	-	1.4±0.4	-	-	100
	Overall	76.2±2.9	13.2±2.2	10.0±0.8	-	0.3±0.07	0.28±0	-	100
0.2 VC + 0.2 Ru	**Light**	80.8±2.3	13±1.7	6.1±1.3	-	-	-	-	100
	Medium	66.3±11.2	16.8±1.4	16.3±9.1	-	-	0.45±0.2	-	100
	Dark	29.6±7.3	22.5±4.0	46.6±4.2	1.2±0.8	-	2.9±1.4	-	100
	Overall	80.3±1.1	8.6±0.7	10.3±0.4	0.4±0.2	-	0.49±0.53	-	100
0.2 VC + 0.2 Cr_3C_2 + 0.2 Ru	**Light**	68.2±11.2	15.6±7.3	16.1±1.5	-	-	-	-	100
	Medium	56.4±2.3	16.6±4.7	25.9±1.5	-	0.3±0.11	2.6±0	-	100
	Dark	40.8±8.3	19.1±4.2	38.9±5.6	0.9±0.8	0.37±0.05	0.3±0.2	-	100
	Overall	79.3±4.3	9.2±1.5	10.7±3.7	0.29±0.06	0.32±0.3	0.27±0.07	-	100

Table 4.8 Mean grain size, WC contiguity and binder mean free path for samples sintered at 1150°C, for 8 minutes at 50 MPa.

Alloy	Mean carbide (d_{WC}) grain size (μm)	WC contiguity	Binder mean free path (μm)
Base (WC-10Co)	2.50 ± 0.39	0.17 ± 0.002	0.80 ± 0.04
Base + 0.2VC	2.48 ± 0.38	0.18 ± 0.004	0.76 ± 0.05
Base + 0.2Cr_3C_2	2.47 ± 0.32	0.20 ± 0.004	0.76 ± 0.04
Base + 0.2Ru	2.46 ± 0.30	0.18 ± 0.003	0.78 ± 0.05
Base + 0.2VC+0.2Cr_3C_2	2.47 ± 0.33	0.18 ±0.003	0.79 ± 0.04
Base + 0.2Cr_3C_2 +0.2Ru	2.47 ± 0.33	0.19 ± 0.003	0.78 ± 0.04
Base + 0.2VC+0.2Ru	2.49 ± 0.31	0.18 ± 0.004	0.79 ± 0.04
Base + 0.2VC+0.2Cr_3C_2 +0.2Ru	2.50 ± 0.40	0.17 ± 0.002	0.78 ± 0.03

4.8.2. SEM fracture study

Figure 4.28 shows the Palmqvist cracks created after Vickers hardness testing. The cracks deviated around the WC particles (indicated by arrows).

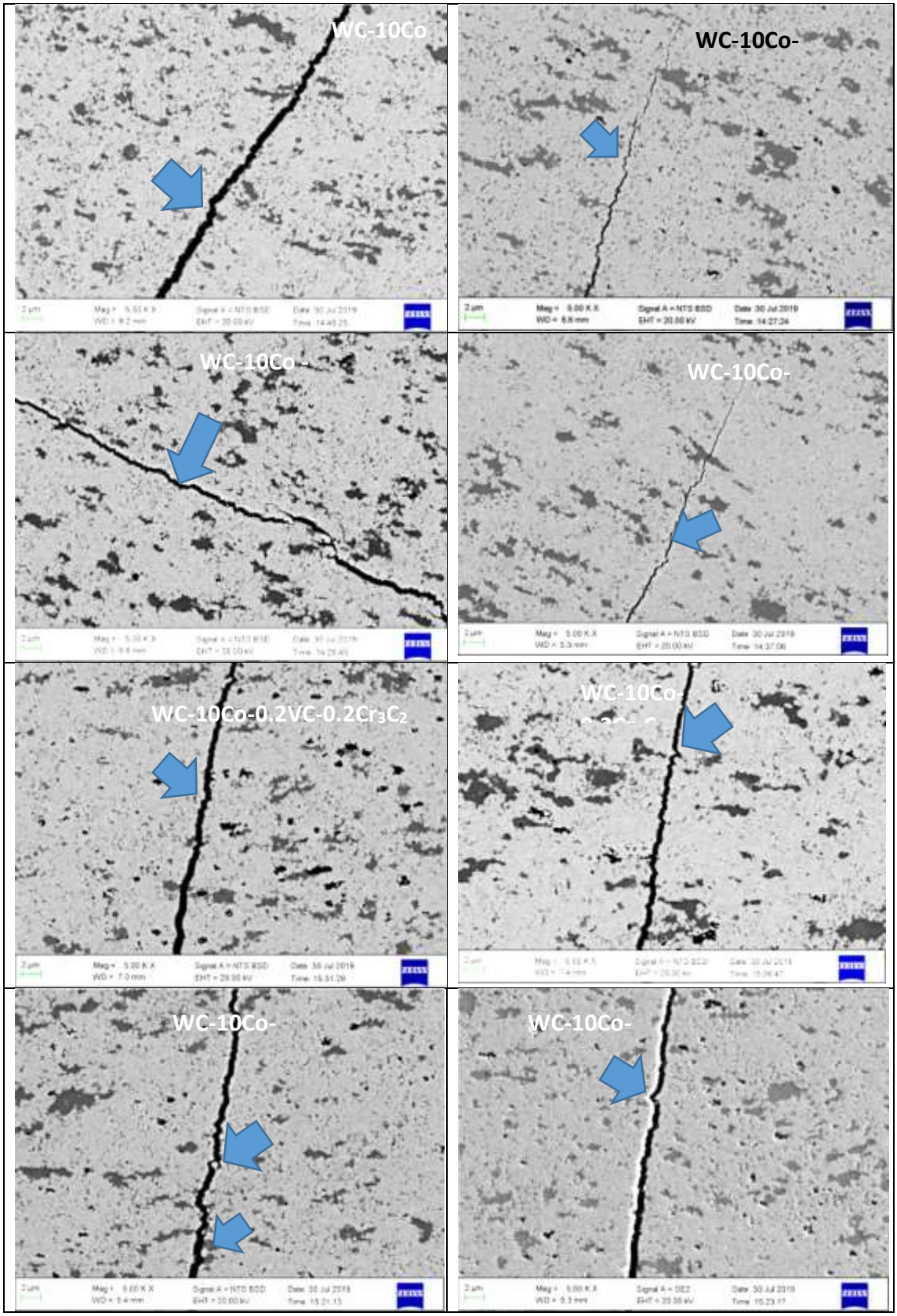

Figure 4.27 SEM-BSE images of un-etched WC-Co alloys sintered at 1150°C, for 8 minutes at 50 MPa showing the Palmqvist cracks deviating around WC (arrows).

4.8.3. Phases present in WC-10Co alloys

X-ray diffraction was done on the sintered samples to identify their crystal structures and phases present (Figures 4.29 – 4.36).

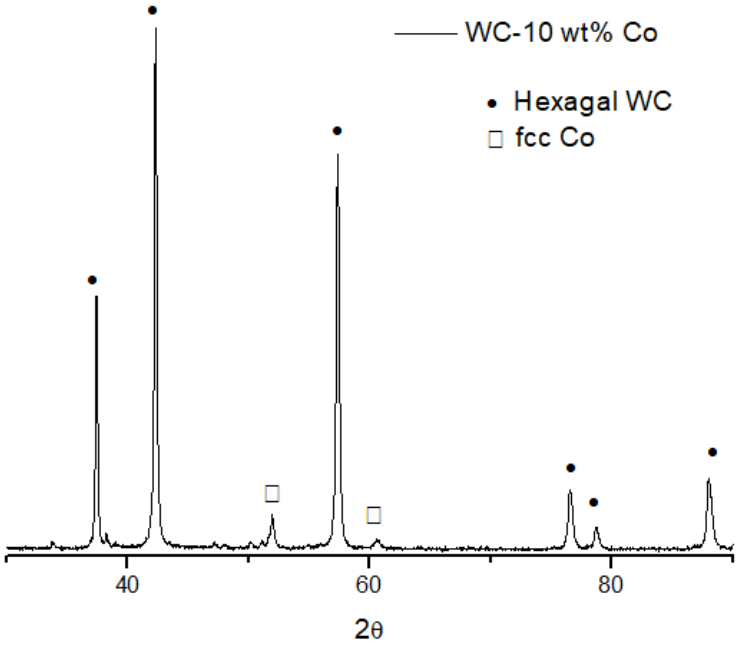

Figure 4.28. X-ray diffraction pattern of the WC-10Co sample sintered at 1150°C, for 8 minutes at 50 MPa.

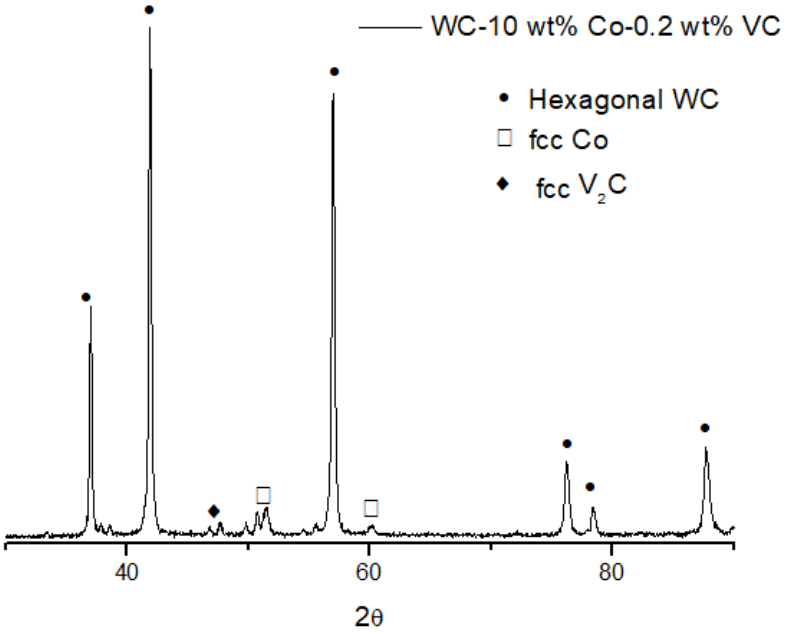

Figure 4.29 X-ray diffraction pattern of the WC-10Co-0.2VC sample sintered at 1150°C, for 8 minutes at 50 MPa.

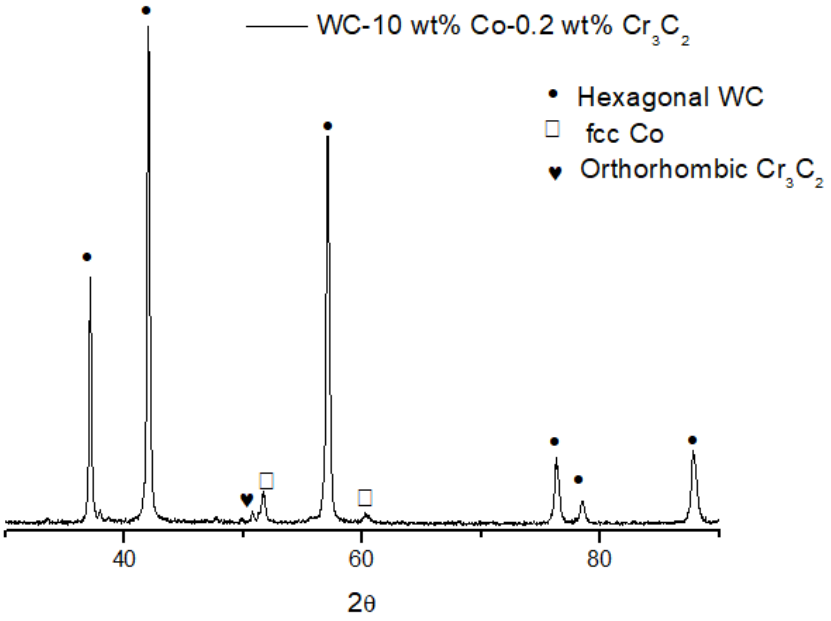

Figure 4.30 X-ray diffraction pattern of the WC-10Co-0.2Cr_3C_2 sample sintered at 1150°C, for 8 minutes at 50 MPa.

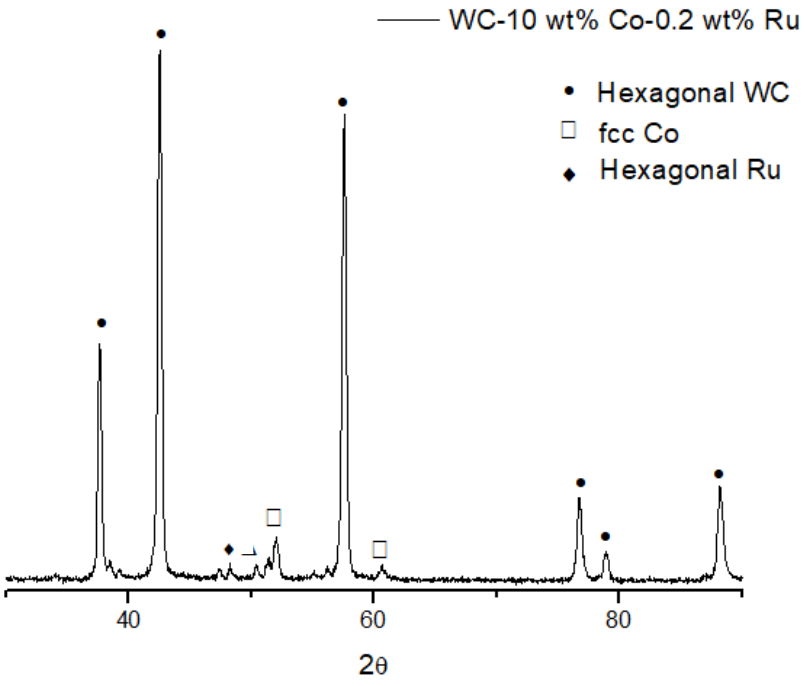

Figure 4.31 X-ray diffraction pattern of the WC-10Co-0.2Ru sample sintered at 1150°C, for 8 minutes at 50 MPa.

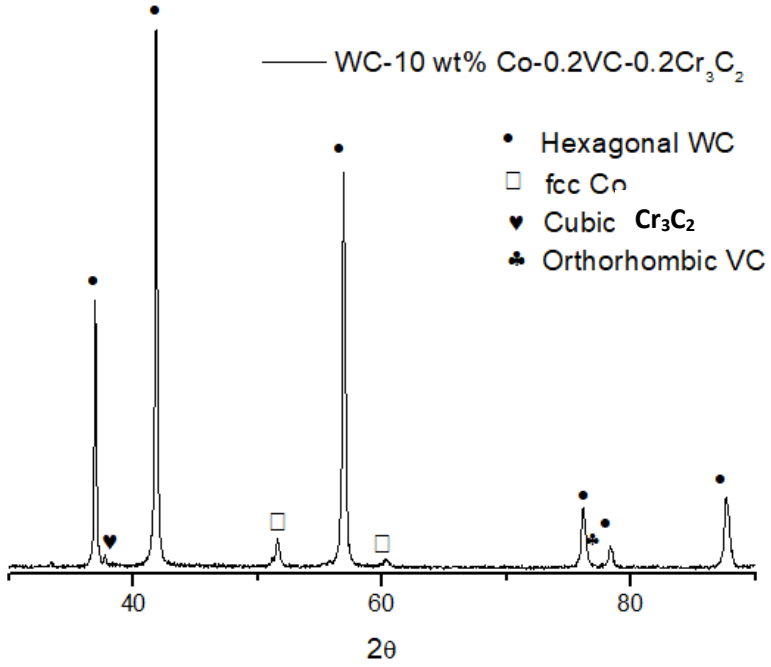

Figure 4.32 X-ray diffraction pattern of the WC-10Co-0.2VC-0.2Cr_3C_2 sample sintered at 1150°C, for 8 minutes at 50 MPa.

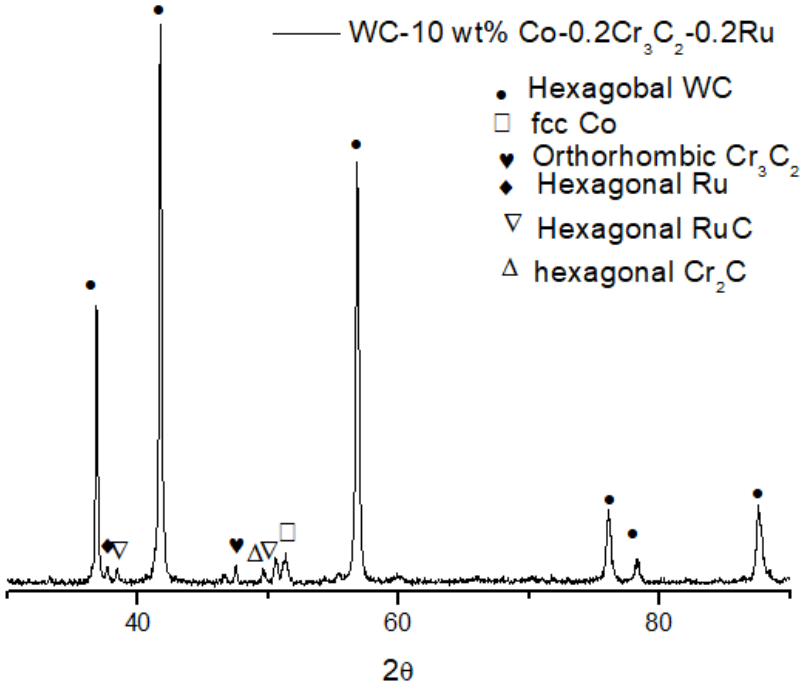

Figure 4.33 X-ray diffraction pattern of the WC-10Co-0.2Cr_3C_2-0.2Ru sample sintered at 1150°C, for 8 minutes at 50 MPa.

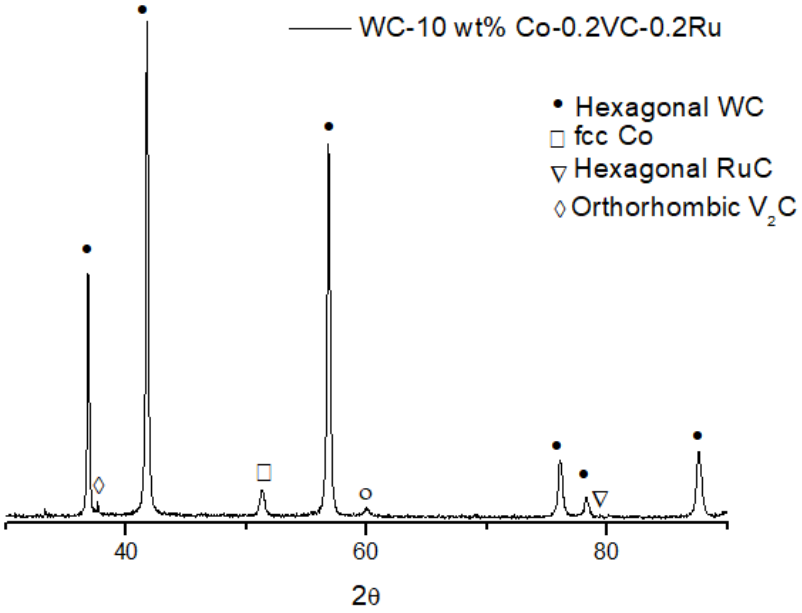

Figure 4.34 X-ray diffraction pattern of the WC-10Co-0.2VC-0.2Ru sample sintered at 1150°C, for 8 minutes at 50 MPa.

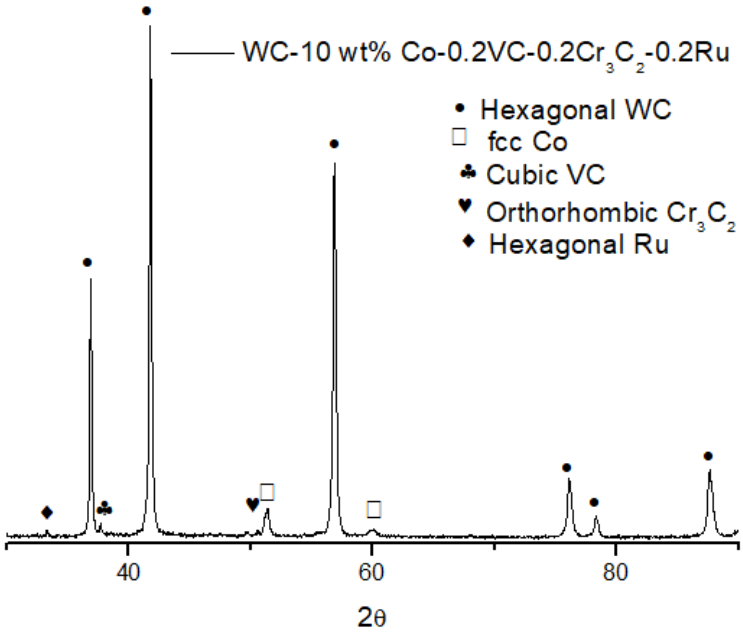

Figure 4.35 X-ray diffraction pattern of the WC-10Co-0.2VC-0.2Cr_3C_2-0.2Ru sample sintered at 1150°C, for 8 minutes at 50 MPa.

Tungsten carbide additives introduced new peaks on the X-ray diffraction patterns, with WC hexagonal and fcc Co remaining the same in all samples and showing no discernible shifts. This was due to the relatively large amounts of WC and Co (~90 wt% WC and 10 wt% Co) compared to the additives. The fcc V_2C originated from the VC addition, orthorhombic Cr_3C_2 was identified, Ru was hexagonal, Ru phase present while VC + Cr_3C_2 showed cubic Cr_3C_2 and orthorhombic VC. The Cr_3C_2 + Ru additive combination gave orthorhombic Cr_3C_2, hexagonal Ru, hexagonal RuC and hexagonal Cr_2C phases. The VC + Ru combination had hexagonal RuC and orthorhombic V_2C phases present. When all the additives were added, orthorhombic Cr_3C_2 and hexagonal Ru were found in X-ray diffraction patterns.

4.9. Mechanical properties

4.9.1. Fracture toughness

The mechanical properties and grain sizes of the samples sintered at 1150°C, for 8 minutes at 50 MPa are given in Table 4.9. Apart from the sample with both additives, the samples' grain size slightly decreased with more grain refiners (Table 4.9), and the smallest grains were observed for the sample with Cr_3C_2. This was significant as the error bars did not overlap. There was an increase in hardness as the additives were introduced from 1564 ± 22 for the base sample to 1737 ± 90 for WC-10Co+0.2Cr_3C_2+0.2Ru and a decrease in fracture toughness as expected from a fracture toughness of the base material 21.9 ± 1.04 MPa·$m^{1/2}$ to 14.6 ± 0.36 MPa·$m^{1/2}$ for WC-10Co+0.2Cr_3C_2. A sample with all the additives had an increase in hardness and fracture toughness compared to the base material. The increase in fracture toughness was 10MPa/m and the increase in hardness was 99 HV_{30}.

Table 4.9 Mechanical properties and WC grain sizes of the samples sintered at 1150°C, for 8 minutes at 50 MPa.

Alloy Composition	Hardness (HV_{30})	Fracture toughness (K_{1C}) (MPa·$m^{1/2}$)	Average grain size (μm)
WC-10Co	1564 ± 22	21.9 ± 1.04	0.524 ± 0.003
WC-10Co+0.2VC	1624 ± 23	14.0 ± 0.86	0.511 ± 0.003
WC-10Co+0.2Cr_3C_2	1672 ± 17	14.6 ± 0.36	0.489 ± 0.002
WC-10Co+0.2Ru	1717 ± 15	13.6 ± 0.47	0.507 ± 0.004
WC-10Co+0.2VC+0.2Cr_3C_2	1709 ± 21	14.1 ± 0.76	0.508 ± 0.003
WC-10Co+0.2Cr_3C_2+0.2Ru	1737 ± 90	13.2 ± 0.37	0.516 ± 0.004
WC-10Co+0.2VC+0.2Ru	1656 ± 18	13.5 ± 0.91	0.510 ± 0.003
WC-10Co+0.2VC+0.2Cr_3C_2+0.2Ru	1663 ± 19	31.4 ± 0.27	0.527 ± 0.004

Chapter Five

5. Discussion

5.1. Introduction

This chapter presents a general discussion of the results that were obtained in this study. The discussion covers the production of cemented carbides from powders to final sintered products and the mechanical properties that were obtained.

5.2. Characterisation of starting powders

The starting powders had different particle sizes as shown in Figures 4.7 – 4.11, and the $d_{0.1}$, $d_{0.5}$ and $d_{0.9}$ particle sizes (Table 4.1). The $d_{0.9}$ values, Table 4.1, matched those from the company specifications for the as supplied powders (Table 3.2). The microstructures of the as-received powders measured by SEM (Figure 4.1) complemented the particle size values.

After the starting powders were mixed and milled for 8 hours in a planetary ball mill with a ball-to-powder ratio of 4-1 (Figures 4.13 – 4.20), $d_{0.1}$, $d_{0.5}$ and $d_{0.9}$ particle size (Table 4.2) gave changes in the particle sizes. The particle sizes of the milled powders were smaller than the as-received particle sizes, as expected. The reduction in particle size after milling was due to the agglomerations being broken up, as well as the particles being reduced (Figure 4.12).

5.3. Optimisation of sintering

5.3.1. Effect of temperature on sintering

There was a temperature effect during SPS densification of WC-10wt%Co carbide as expected. As the sintering temperature was varied from 1000°C to 1450°C keeping pressure and dwell time at 50 MPa and 5 min, the densification increased with temperature (Table 4.4). This was because as the temperature rose, there was some solid solution between WC and Co, helping to close all the existing pores that were due to the incomplete sintering as shown in Figure 4.27. The sample sintered at a lower temperature (1000°C) had poor densification (63%) with high amounts of porosity, as confirmed by the level of porosity in the microstructure (Figure

4.23). The poor densification was due to incomplete sintering of the powder at the low temperature, resulting in low capillary forces and little wetting of WC which then resulted in low density density (Garcia *et al*., 2019). The increase in temperature to 1150°C improved densification to 96% (Table 4.4). As the temperature was increased to 1250°C, the density increased to 97% (Table 4.4) these results agreed with those of Bonache *et al.* (2011) where the microstructural control of ultrafine and nanocrystalline WC-12wt% Co-VC and Cr_3C_2 were consolidated by spark plasma sintering, varying temperature and additive to achieve samples with high hardness and fracture toughness.

5.3.2. Effect of time on sintering

The WC-10wt%Co sample sintered at 1000ºC had a relative density of 63.2%, meaning the sample was not properly sintered because the sintering temperature and time was low (Figure 4.23). Since densification of 99% was not reached, a different approach was made to increase the sintering dwell-time from 5 minutes to 8 minutes. Two samples of WC-10wt%Co were sintered at 1150°C and 1250°C for 8 minutes. Both samples showed a significant improvement with 1150°C at 99.3% and 1250°C at 99.5% (Table 4.5). The sintering temperature of 1150°C was chosen because of the high density that was achieved at a lower sintering temperature for 8 minutes. When sintering time was increased to 8 minutes, the average grain size decreased from 0.87 µm (Table 4.4) to 0.52 µm (Table 4.5), at shorter time there was more porosity and this might have affected the measured grain size.

5.4. Sintering WC-10wt%Co

The cemented carbide underwent solid phase sintering in which starting powders were densified in a solid state at an elevated temperature. There was a rapid initial densification (Figures 3.1- 3.8) that was observed due to capillary force that was applied on the solid particles by the wetting liquid. This was followed by an elimination of existing pores by minimising the surface energy, which was the driving force for the densification process which is similar to the work done by Thomas *et al*. (2015).

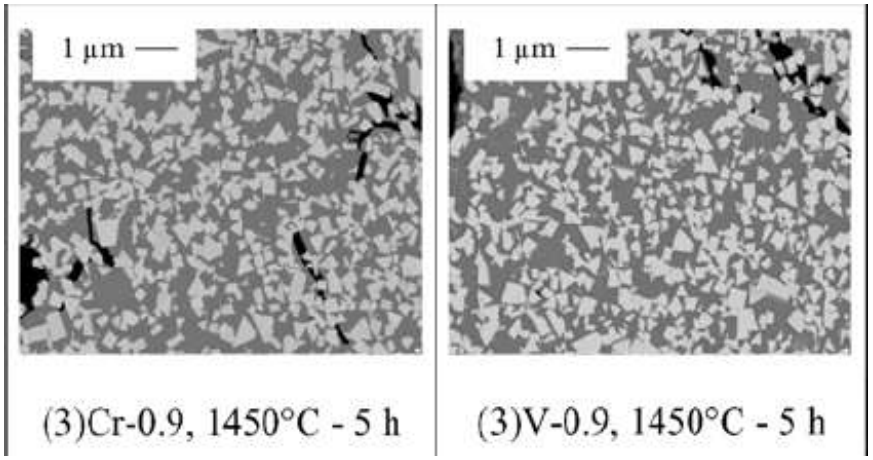

Figure 5.1 SEM micrographs of samples (3)Cr-0.9 and (3)V-0.9. (WC in white, Co in grey and C in black) Chabretou (*et al.*, 2003).

The phenomenon of solid and liquid phase sintering was observed through the SEM micrographs in comparison to work, including Chabretou *et al.* (2003) where they used liquid phase sintering process for densification (Figure 5.1). The densities of the two different sintering regimes with overlapping errors are shown in Figure 5.2 with their corresponding relative densities. The densification behaviour and grain size of WC-10wt%Co cemented carbide by SPS at different temperatures (Figure 5.2) showed that the density of the WC-10wt%Co increased with the sintering temperature. Samples sintered with SPS tended to have smaller grains (0.88 µm to 0.40 µm) in comparison with conventional sintering shown in Figure 5.1 with grain sizes ranging from 0.78 µm to 1.2 µm (Chabretou *et al.*, 2003). In conventional sintering, there can be large abnormal WC grains that are more anisotropic than the WC matrix, while in the present work, rounder and evenly distributed WC grains were seen; this is due to a fast sintering time which did not allow for grain growth.

The wettability of WC by liquid Co in both solid phase and liquid phase sintering process is important as it completes the sintering process. Complete wetting was seen in the current work where contact angles were formed by the liquid Co-based binder on the WC surface with WC/WC grain boundaries (Chabretou *et al.*, 2003). The microstructures in Figure 4.26 show samples with carbon content of about 5.6 wt% C and the excess additives of VC and Cr_3C_2 showing different contact angles of WC/WC grain boundaries with Co in Figure 4.26. Shown by arrows. This resulted in the Co diffusion from WC-Co regions having high carbon contents into regions of low carbon contents. This is shown in Figure 4.27 (SEM-BSE images

of etched WC-10Co alloys sintered at 1150°C). Cobalt diffusion occurred in regions of different WC mean grain sizes with low Co grain sizes due to their capillary forces (Garcia *et al*., 2019)., these can be seen in Figure 4.27. The Co shift resulted in Co pools which gave poor mechanical properties and inconsistent grain size (Chabretou *et al.*, 2003).

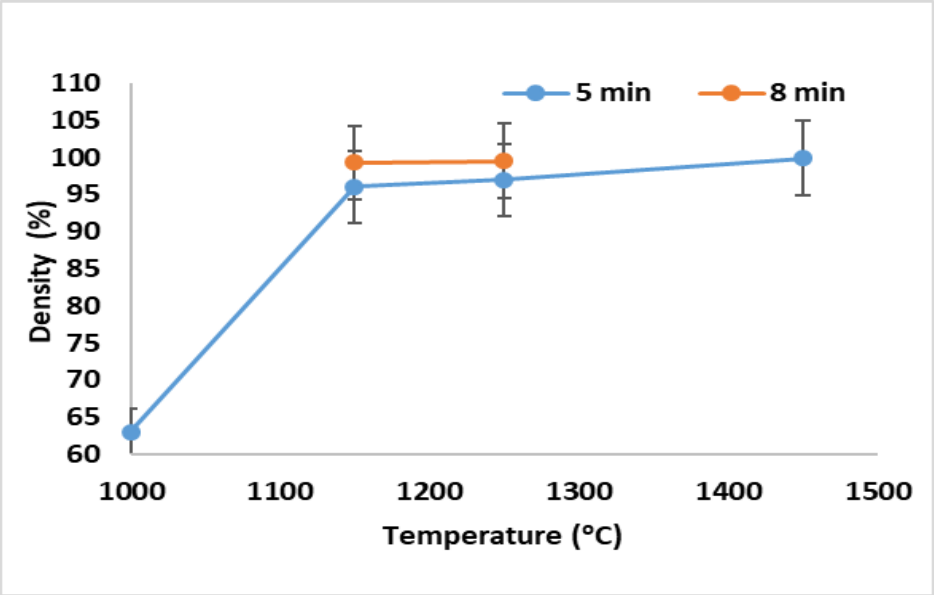

Figure 5.2 Effect of temperature on the density of WC-10wt%Co sintered at 50 MPa for 5 and 8 minutes.

5.5. Additives to WC-10wt% Co

Three carbides were added to the WC-10wt%Co base material. Although SPS produced samples with high densification and hardness (Table 4.9) amounts of 0.2 wt% Cr_2C_3, 0.2 wt% VC and 0.2 wt% Ru were added to WC-10wt%Co to improve the overall hardness of the base material (Table 3.3). The purpose of adding Ru was to study the effect it has on WC-10wt% Co compared to carbide additives (Table 4.9). Ruthenium inhibited the grain growth of WC-10wt%Co (Table 4.9 and Figure 4.27) and increased the fracture toughness of the base sample. The increase in toughness was due to the hardening of Co binder. Contrary to Shing *et al*. (2001), the hardening of WC-10wt%Co due to Ru additive was greater than for the VC additive. Shing *et al*. (2001) found that there was a larger decrease in WC grain size and an increase in hardness when there were small additions of VC compared to that of Ru additive.

These differences were due to the difference in experimental procedure, where Shing et *al.* (2001) used similar base alloy WC-10 wt%Co with additives of different compositions ranging from 0.4 to 3.0 wt% Ru and VC. All their samples were SPSed at 1410°C which was close to the onset melting temperature of the alloys and above their eutectic temperatures.

The Cr_3C_2 additive has been found to have a positive influence on the properties of WC-10wt%Co. The current results agree with Huang *et al*. (2006), Sun *et al*. (2008) and Siwak *et al*. (2016) that alloys with Cr_3C_2 additions possess high hardness and toughness as seen in Table 4.9: WC-10Co+0.2Cr_3C_2 had a hardness of 1672 ± 17 HV_{30} while WC-10Co+0.2VC+0.2Cr_3C_2 had a hardness of 1709 ± 21 HV_{30}. Figure 5.3 shows that the hardness of 10Co-0.2 Cr_3C_2 was much lower, and the fracture toughness was slightly higher than that of Sun *et al.* (2008) which might be due to larger Co pools of about an average of 1-2 µm with an average grain size of 435 nm after sintering.

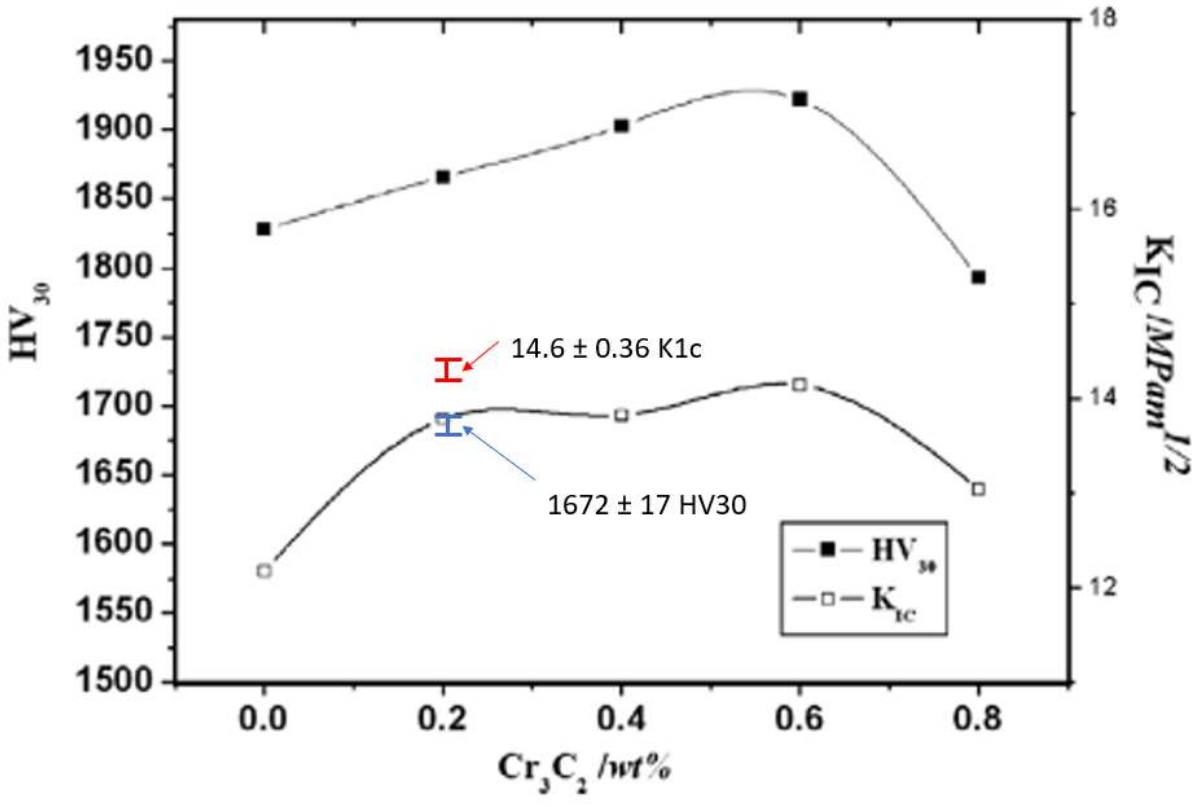

Figure 5.3 Effect of Cr_3C_2 on WC-Co mechanical properties by Sun *et al.* (2008) with WC-10Co-0.2 Cr_3C_2 added (Blue-Fracture toughness, Red-Hardness).

The XRD patterns of all sintered samples shown in Figures 4.29 to 4.36, and all compositions had similar patterns, consisting of hexagonal WC and cubic Co. The alloys sintered at 1150°C for 8 minutes at 50 MPa in vacuum (WC-10wt%Co) had poorly distributed binder, with pools of the Co binder (Figure 4.27). The Cr_3C_2 addition was detected by SEM which is shown as the medium contrast in Figure 4.27 and was shown by the EDX analysis Table 4.7. The EDX analysis was done on the largest areas possible, to avoid the possibility of collecting signals from the surrounding phases (Goldstein et al., 2014). Figure 5.4 shows that Thanjekwayo *et al.* (2009) could not detect the 0.4 wt% Ru additive in WC-10wt%Co since it was below the 1 wt% detection limit. Figure 5.5 shows the similar findings by Kurasha (2017) where XRD patterns for sintered alloys with less than 1 wt% additives of Ta and Nb did not detect the Ta and Nb by XRD.

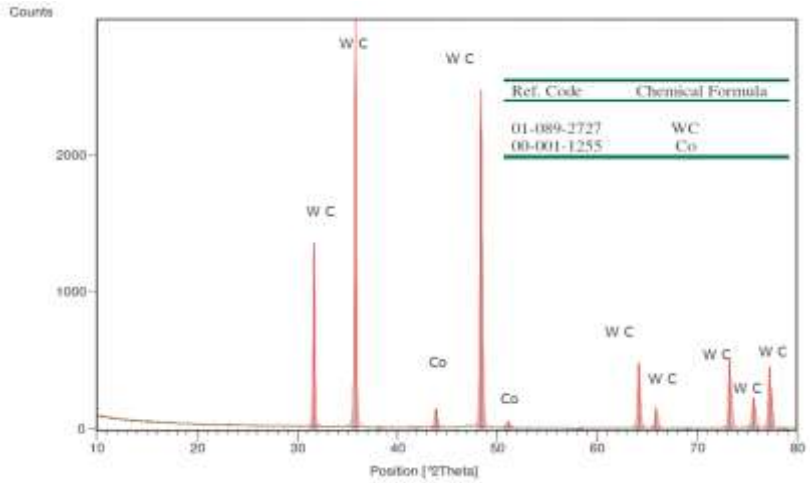

Figure 5.4 XRD pattern for WC-10%Co-1.5%Ru alloy (Thanjekwayo *et al.*,2009).

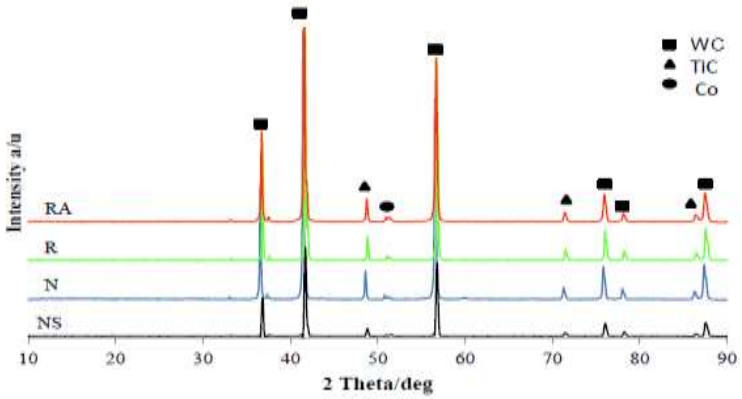

Figure 5.5 XRD patterns for alloys NS(WC-Co-Ti), N(WC-Co- TaC), R(WC-Co- NbC), and RA(WC-Co- TiCN), showing the WC, TiC and Co peaks (Kurasha, 2017).

The medium contrast regions observed in the SEM-BSE indicates the solid solution of V and Cr with Co. The microstructure of the samples shown in Figure 4.27 had some different contrasts of WC, which appeared to be solid solutions, and further analyses confirmed that these were different compositions and contrasts of WC, and in some areas solid solutions with the additives were detected by the microstructural and composition analyses in Table 4.8 and Figure 4.26.

Figure 4.27 shows a wide grain size range with many WC/WC contacts but without a continuous Co binder for samples with Cr_3C_2. The microstructures in Figure 4.27 shows that Cr_3C_2 is a good grain growth inhibitor since the material after sintering had a lower grain size (Table 4.9) compared to the base WC-10Co. Although Cr_3C_2 had a small grain size, there were several cobalt pools compared to the Ru additive alloy. The VC alloy (WC-10Co-0.2VC) (Figure 4.27) on the other hand had more binder pools than the base sample, WC-10Co-0.2Cr_3C_2 and WC-10Co-0.2Ru; this might be since V is less soluble in Co than Ru and Cr (Massalski, 2009).

The solid solutions observed in the microstructures were due to the elements of the WC phase diffusing in Co binder. The effect of Ostwald ripening was not as effective. In areas of low Co content, some grain boundaries of the particles were not wetted (Figure 5.26). Grain growth in such areas plays an important role; in Figure 4.27 these were more WC/WC interface contacts which restricted grain growth and thus limiting the Ostwald ripening effect (Massalski, 2009). The effect of SPS played an important role in avoiding grain growth, as this process is fast and does not allow time for grain growth in comparison with the conversional sintering method that would take 24 hours to sinter (Upadhyaya, 2001).

The Co pool presently determined are consistent with those previously reported by Sun *et al.* (2008) for alloys with similar Cr or V contents. The phase (V,W)C_x was not detected because either the V content was slightly lower than the limit to form this carbide or the diffusion time is not sufficient (Sun *et al.*,2008).

The combined additives of the alloys showed interesting microstructural changes compared to the base sample. Both WC-10Co-0.2VC-0.2Cr_3C_2 and WC-10Co-0.2Cr_3C_2-0.2Ru had similar binder distributions, they both had binder pools compared to the WC-10Co-0.2VC-0.2Ru

which had relatively low binder pools. This proves that Ru remains in solution with Co binder (Shing *et al*., 2001) which then strengthens the binder. This translates to the increase in mean free path as grain size increased (Figure 5.6).

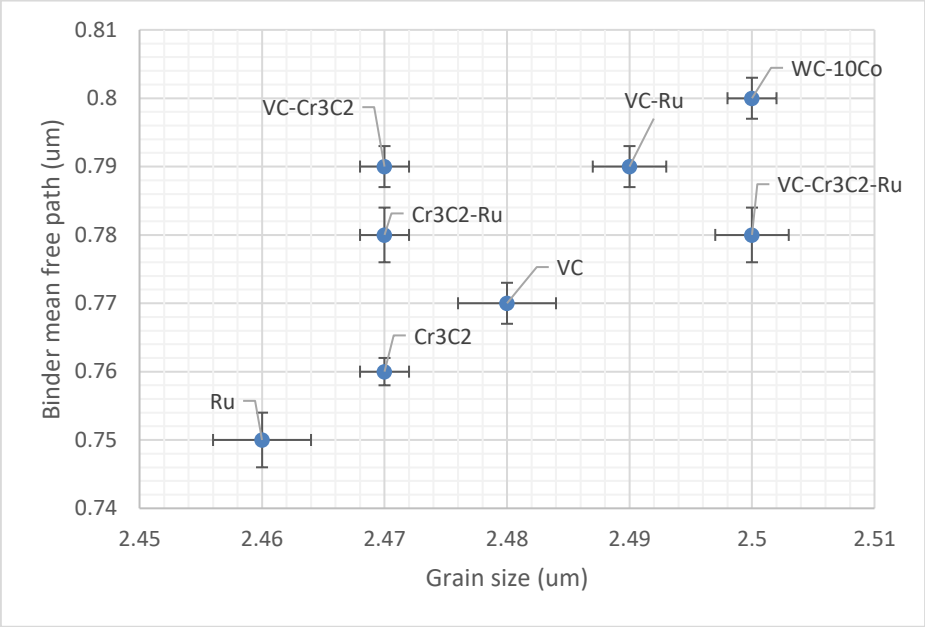

Figure 5.6 Effect of grain size of WC-10wt%Co alloys in binder mean free path.

Contiguity is defined as the fraction of the total internal surface area of the phase that is shared by particles of the same phase (Luyckx and Love, 2006). Therefore, by this definition, contiguity of a sample can vary between zero and close to but not equal to one. In cemented carbide as the volume fraction of cobalt binder phase tends to one, the contiguity of the carbide phase tends to zero and when the cobalt volume fraction tends to zero the contiguity of the carbide phase tends to one (Luyckx and Love, 2006). The alloys with VC-Cr_3C_2 and VC-Ru had the same binder mean free path but different d_{WC} grain sizes. Other samples such as VC-Cr_3C_2, Cr_3C_2-Ru and Cr_3C_2 had the same carbide grain size with different binder mean free path. The general trend shows that as the grain size increases, so did mean free path. An overall inverse proportional relationship was observed between carbide grain size and WC contiguity (Figure 5.7): there was a decrease in WC contiguity as the carbide grain size increased.

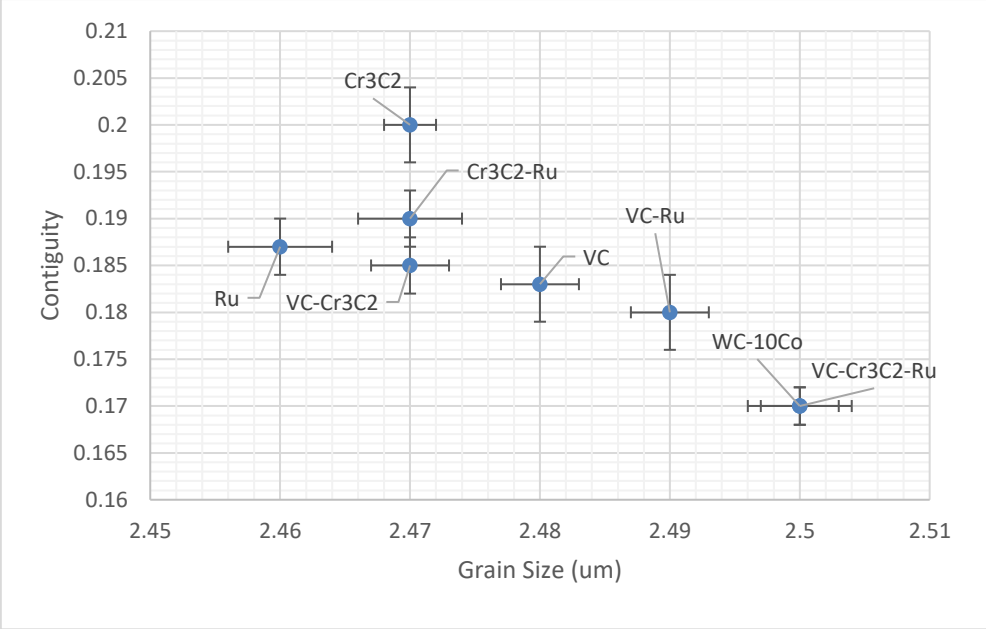

Figure 5.7 Relationship between average WC grain size and WC contiguity.

There is an inverse proportional relationship between the binder mean free path and WC contiguity (Figure 5.8): i.e. the binder mean free path decreased with increased WC contiguity of the samples, with VC alloy as an outlier. The good relationship between WC contiguity and binder mean free path was due to even distribution of Co binder and good solubility of Co with WC as well as the wetting of WC with Co.

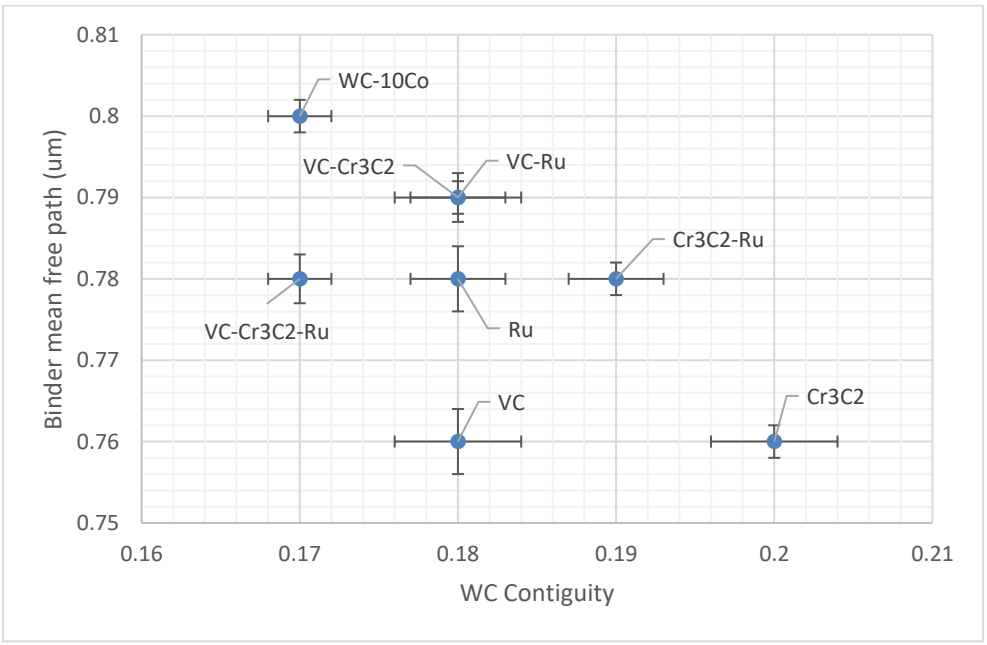

Figure 5.8 Relationship between binder mean free path and WC contiguity of the WC-10wt%Co alloys sintered at 1150 °C for 8 hours at 50 MPa.

The increase in hardness occurred because of the decrease in grain size of the samples as a result of the additives introduced to the WC-10wt%Co base alloy. The base sample had a Vickers hardness of 1564 ± 22 with a grain size of 0.524 ± 0.002 µm, when the additives were introduced the hardness slightly increased to 1624 ± 23 (0.2 wt% VC) with a slightly reduced grain size of 0.511 ± 0.004 µm. A small increase in hardness was again observed when there was an addition of 0.2 wt% Cr_3C_2 in the base sample to 1672 ± 17 with a reduction in grain size to 0.489 ± 0.004 µm. The highest increase in hardness was observed when 0.2 wt% Ru and 0.2 wt% Cr_3C_2 was introduced to 1737 ± 9 with a corresponding grain size of 0.516 ± 0.002 µm. Although there was a small change in grain size of the samples, the relationship was demonstrated clearly.

There was a general positive correlation between grain size of the alloyed samples with fracture toughness: as the grain size of the samples increased so did fracture toughness. The additives of Cr_3C_2, VC + Cr_3C_2, Ru, VC + Ru, VC, and Cr_3C_2 + Ru had similar facture toughness values. The increase in fracture toughness can be seen in comparison to the base material and the alloy with VC + Cr_3C_2 + Ru additives. These results confirmed the claims that Ru additions increase the hardness of the WC-Co (Shing *et al*., 2001). In this project 0.2 wt% Ru was used while Shing *et al.* (2001) used 0.4 to 3 wt% with the highest hardness observed at 2 wt% Ru additives (Figure 2.16). However, contrary to the claims by Shing *et al*. (2001), these results show that Ru additives can decrease the toughness of the WC-Co.

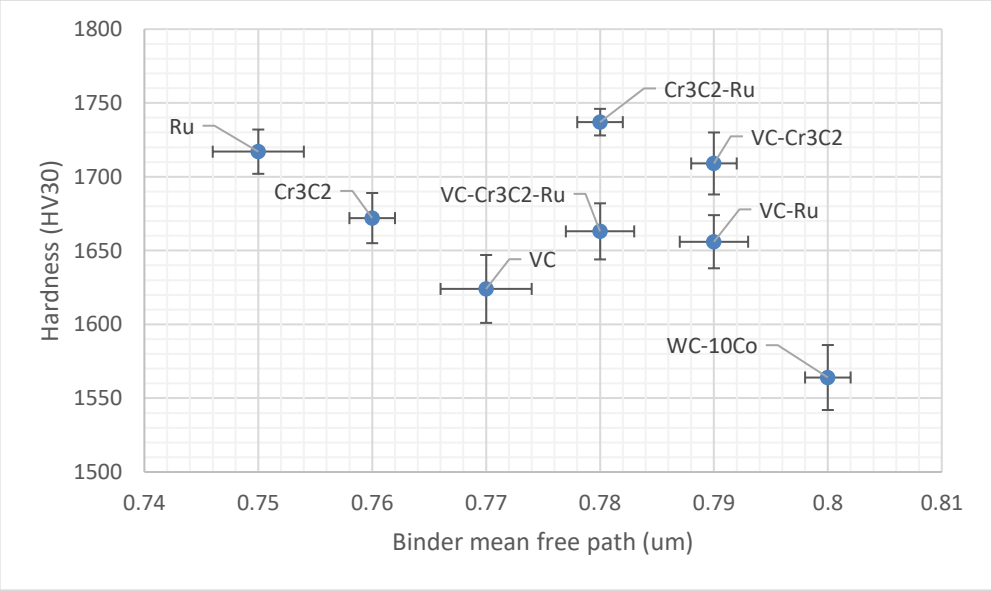

Figure 5.9 Effect of binder mean free path of WC-10wt%Co alloys on hardness.

There was a linear relationship between binder mean free path and hardness (Figure 5.9), which confirms the studies by Gruter (1959) and Exner and Fischmeister (1966). An increase in hardness was observed as a result of the additions to the WC-10wt%Co base sample. Hardness was found to be 1564 ± 22 HV_{30} for WC-10wt%Co, the highest hardness that was observed in a single additive was Ru at 1717 ± 15 HV_{30}, and 1737 ± 9 HV_{30} when Cr_3C_2 was introduced.

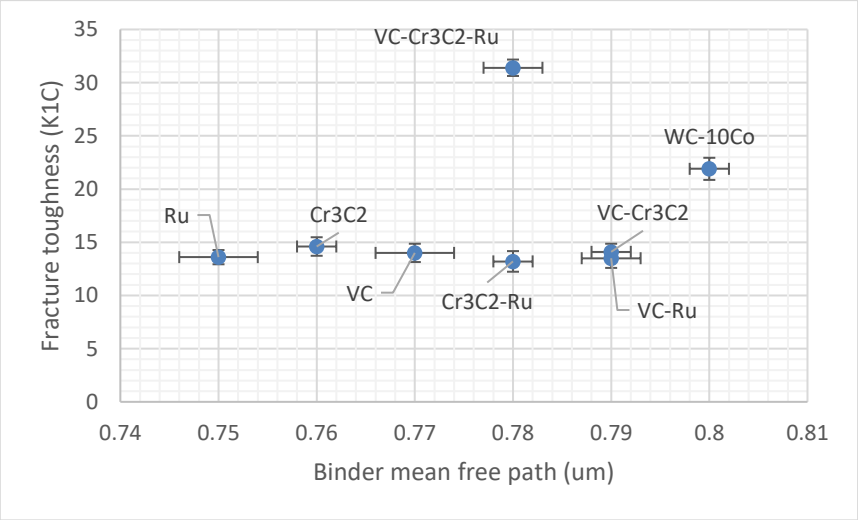

Figure 5.10 Relationship between fracture toughness and binder mean free path of the WC-10wt%Co alloys sintered at 1150°C for 8 minutes at 50 MPa.

The relationship between fracture toughness and binder mean free path shows that the rate of increase in toughness corresponds to the decrease in hardness, which is higher for coarse carbide grains size distribution (Figure 5.10). The high toughness in WC-Co alloys was attributed to the large binder mean free path. This was due to the grain growth inhibitors preventing WC grain growth, thus decreasing binder mean free path.

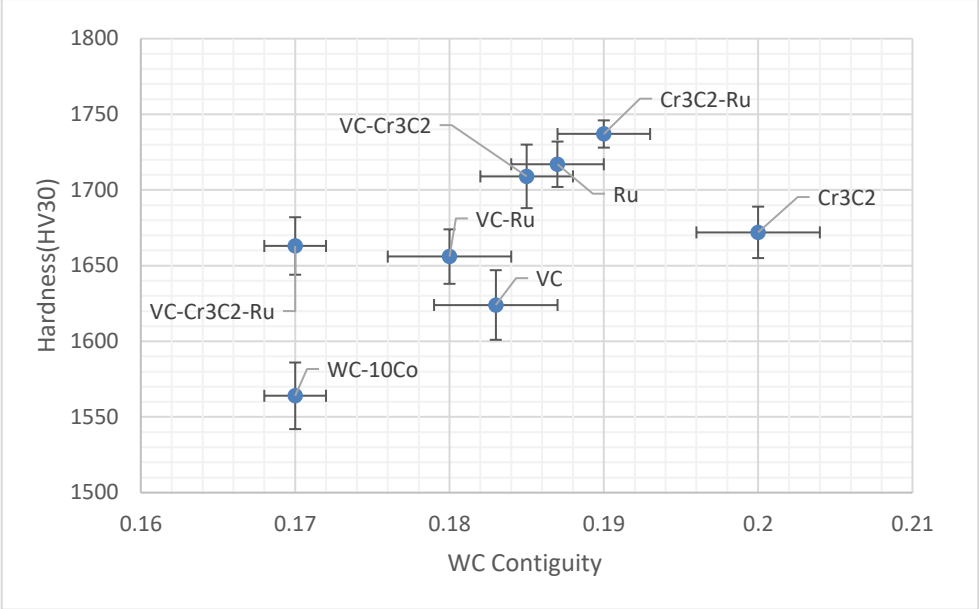

Figure 5.11 Relationship between Vickers hardness and WC contiguity in WC-10wt%Co alloys.

The effect of contiguity on both fracture toughness and hardness (Figures 5.11 and 5.12) on WC-Co alloys was not surprising as the morphology of individual phases played a crucial role on mechanical deformation in all samples. All samples with single additives had large WC contiguities, and as a result, low fracture toughness and high hardness.

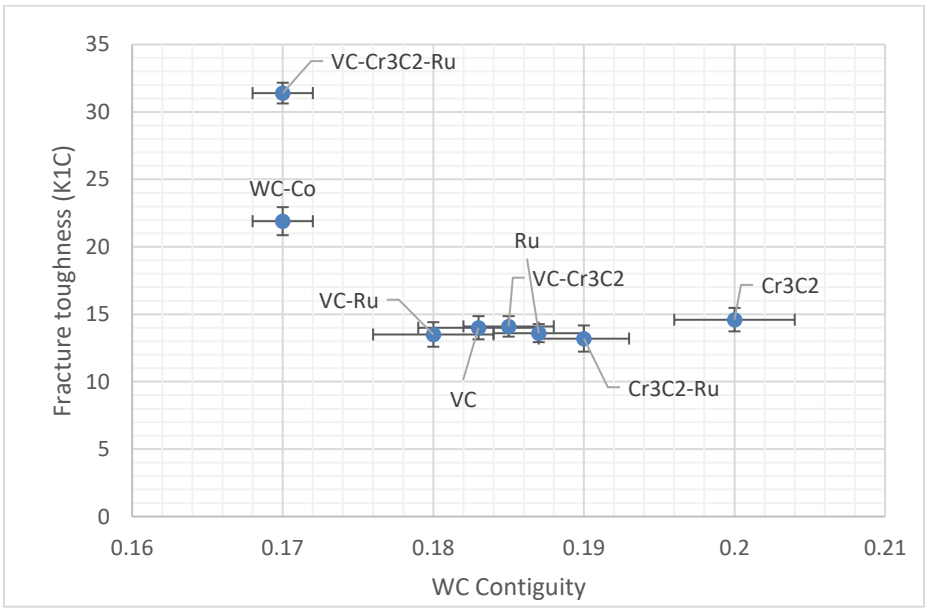

Figure 5.12 Relationship between fracture toughness and WC contiguity of the WC-10wt%Co alloys sintered at 1150 °C for 8 minutes at 50 MPa.

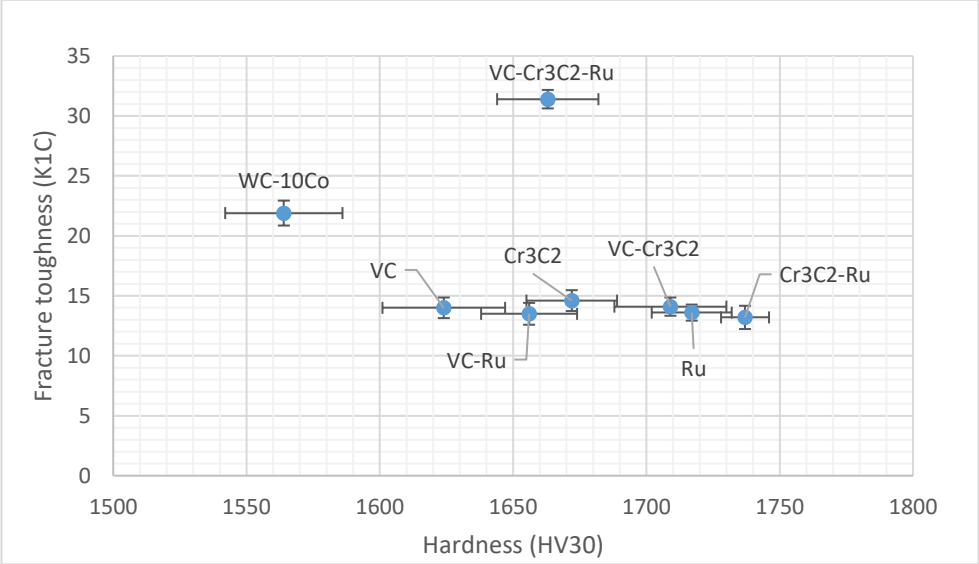

Figure 5.13 Relationship between fracture toughness and Vickers hardness of the WC-10wt%Co alloys sintered at 1150 °C for 8 minutes at 50 MPa.

Fracture toughness for each sample given in Table 4.9 show they are strongly dependent upon the free mean path of the cobalt binder, and the contiguity and mean size of the WC grains (Figure 5.6 – 5.12). A linear relationship between hardness and toughness is found for all alloys (Figure 5.13), as harness increase the fracture toughness decrease, this proves the indirect measurement of mechanical properties by measuring WC contiguity and binder mean free path. A consistent relationship was found between fracture toughness and microstructure, indicating the intrinsic character of the fracture parameter as a material property. The effect of combining carbide grain size and cobalt content with additives are rationalised through microstructural parameters such as carbide contiguity and binder thickness. As shown in Tables 4.8 and 4.9, fracture toughness had a rising trend with increasing mean free path and decreasing carbide contiguity. Therefore, Ru and Cr_3C_2 were shown to have the best mechanical properties when added in 0.2 wt% in WC-10wt%Co. The best sample was WC-10Co-0.2Cr_3C_2 because the sample had a good balance between hardness and fracture toughness.

Although the SPS parameters used in this research did not produce optimum results, the SPS sintering process reduced sintering time compared to conventional sintering, increased mechanical properties and reduced Ostwald ripening effect while increasing WC contiguity and binder mean free path. However, further parameter optimisation is needed to produce much better results, mainly sintering temperature and time, and additive amounts. The best alloy was WC-10Co+0.2Cr_3C_2+0.2Ru with a hardness of 1737 ± 90 HV_{30}, fracture toughness of 13.2 ± 0.37 MPa·$m^{1/2}$, mean carbide grain (d_{WC}) of 2.47 ± 0.33 µm, WC continuity of 0.19 ± 0.003 and binder mean free path of 0.78 ± 0.04 µm.

Chapter Six

6. Conclusions

The effect of VC, Cr_3C_2 and Ru additives on mechanical properties of WC-10wt%Co sintered in spark plasma sintering (SPS) furnace at 1150°C with a heating rate of 200°C resulted in overall relative densifications of greater than 98% for all samples. Although all samples with additives had an additive of 0.2 wt%, samples with additives of Cr_3C_2 and Ru had much better results. When comparing results of single additives to the base sample, additive with Cr_3C_2 had a hardness of 1672 ± 17, Ru with 1717 ± 15 and VC was 1624 ± 23.

Introducing additive resulted in finer WC grain size for all samples relative to the base sample. The samples with Cr_3C_2 additives had much smaller WC grain sizes which is evidence by the hardness. The poor binder distribution in samples Figure 4.26 lead to high WC contiguity Table 4.8 which allowed an increase in WC/WC interface fracture in Figure 4.27. The increase in mean free path (Table 4.8) theoretically reduces the abrasive were resistance which was not teased during this project. Samples with Cr_3C_2 and Ru had much high binder mean free path which was 17% greater than the base material and 7% higher than for the other additives.

Of the materials examined, that with the best combination of properties was WC-10Co+0.2Cr_3C_2+0.2Ru with a hardness of 1737 ± 90 HV_{30}, fracture toughness of 13.2 ± 0.37 $MPa{\cdot}m^{1/2}$, mean carbide grain (d_{WC}) of 2.47 ± 0.33 µm, WC continuity of 0.19 ± 0.003 and binder mean free path of 0.78 ± 0.04 µm.

7. REFERENCES

Allibert, C., Marty, P., Gagnoud, A. and Fautrelle, Y. (2000). Estimate of the diffusion coefficient in Co based liquids, International Journal of Heat Mass Transfer. 43 (3): pp. 437–445.

Bonache, V., Salvador, M., Rocha, V. and Borrell, A. (2011). Microstructural Control of Ultrafine and Nanocrystalline WC–12Co–VC/Cr_3C_2 Mixture by Spark Plasma Sintering. Ceramics International 37: pp. 1139–1142.

Borgh, I., Hedström, P., Odqvist, J., Borgenstam, A., Ågren, J., Gholinia, A., Winiarski, B., Withers, P.J., Thompson, G.E., Mingard, K. and Gee, M.G. (2013). On the three-dimensional structure of WC grains in cemented carbides. Acta Materialia. 61(13): pp. 4726-4733.

Brookes, K. World Directory and Handbook of Hard-metals and Materials. (1975). United Kingdom: Metal Powder Industry.

Cha S., Hong H. and Kim B. (2003). Spark plasma sintering behaviour of nanocrystalline WC–10Co cemented carbide powders, Materials Science and Engineering. A 351: pp. 31–38.

Chabretou, V., Allibert, C., Missiaen, J. (2003). Quantitative Analysis of the Effect of the Binder Phase Composition on Grain Growth in WC-Co Sintered Materials. Journal of Materials Science. 38: pp. 2581 – 2590.

Cho, Y., Yoon, D. and Kim, B. (2004). Surface roughening transition and coarsening of NbC grains in liquid cobalt-rich matrix, Journal of the American Ceramic Society. 87 (3): pp.443–448.

Choi, K., Hwang, N., and Kim, D. (2000). Effect of VC Addition on Microstructural Evolution of WC–Co Alloy: Mechanism of Grain Growth Inhibition. Powder Metallurgy. 43(2): pp. 168–72.

Deng, N., Gang, M. and Zhao, Z. (2013). Interfacial Behaviour of Micro-Cellular Structural $Al_90Mn9Ce_1/TiO_2$ Composite Prepared by Spark Plasma Sintering. Materials Science Forum. 749: pp. 589-594.

Exner, H. and Fischmeister, F. (1966). Structure of sintered tungsten carbide-cobalt alloys. Archiv für das Eisenhüttenwesen. 37: pp. 417–426.

Farag, S., Konyashi, I. and Ries, B. (2020). The Influence of Grain Growth Inhibitors on The Microstructure and Properties of Submicron, Ultrafine and Nano-Structured Hardmetals – A Review. International Journal of Refractory Metals & Hard Materials.77: pp. 12-30

Fernandes, C., Senos, A (2011). Cemented carbide phase diagrams: A review. International Journal of Refractory Metals & Hard Materials & Hard Materials. 29: pp. 405–418.

Froschauer, L. and Fulrath, R. (1976). Direct observation of liquid-phase sintering in the system tungsten carbide-cobalt, Journal of Material Science. 11 (1): pp.142–149.

Garcia, J., Cipres, V., Blomqvist, A. and Kaplan, B. (2019). Cemented carbide microstructures: a review. International Journal of Refractory Metals & Hard Materials. 80: pp. 40-68.

Gurland, J. (1958). The measurement of grain contiguity in two-phase alloys. Trans A1ME, 212: pp. 452–455.

Goldstein, J. Newbury, D., Echlin, P. Joy, C. Fiori, C. and Lifshin, E. (2014) Scanning Electron Microscopy and X-Ray Microanalysis: A Text for Biologists, Materials Scientists, and Geologists. New York and London. 4th Edition.

Golovchan, V. and Litoshenko, N. (2003). On the contiguity of carbide phase in WC-Co hardmetals. International Journal of Refractory Metals & Hard Materials Hard Materials. 21 (5–6): pp. 241–244.

Gruter M. (1959). Thesis: Untersuch ungen in den Systemen Co–C, Co–WC. Germany, Münster.

Guillermet AF. (1987). Use of phase-diagram calculations in selecting the composition of Fe–Ni bonded WC tools. International Journal of Refractory Metals & Hard Materials Hard Materials. 6 (1): pp. 24–7.

Hall, E.O. (1951). The Deformation and Ageing of Mild Steel: III Discussion of Results. Proceedings of the Physical Society: London. 64 (9): pp. 747–753.

Han, X., Sacks, N., Milman, Y. and Luyckx, S. (2009). On plastic deformation mechanisms of WC–15 wt% Co alloys at 1000°C. International Journal of Refractory Metals & Hard Materials 27: pp.274–281.

Haung, S., Vanmeensel, K., Van der Biest, O. and Vleugels, J. (2007). VC, Cr_3C_2 and NbC Doped WC-Co Cemented Carbides Prepared by Pulse Electric Current Sintering. International Journal of Refractory Metals & Hard Materials. 25: pp. 417-422.

Hui, W., Meiqin, Z., Jiangwen, L., Zhongcheng, L., Zhenua, S., Liuzhang, O. and Min, Z. (2015). One-Step Synthesis of Ultrafine WC–10 Co Hard-Metals with VC/V_2O_5 Addition by Plasma Assisted Milling. International Journal of Refractory Metals & Hard Materials 48: pp. 97–101.

Human, M., and Exner, H. (1996). Electrochemical behaviour of tungsten-carbide hardmetals. Materials Science and Engineering A. 209 (2): pp. 180–191.

Hochstrasser, S., Mueller, Y., Latkoczy, C., Virtanen, S. and Schmutz, P. (2007). Analytical characterization of the corrosion mechanisms of WC-Co by electrochemical methods and inductively coupled plasma mass spectroscopy. Corrosion Science. 49 (4): pp. 2002–2020.

Hwan-Cheol, K., Dong-Young, O. and In-Jin, S. (2004). Sintering of nanophase WC-15 vol.%Co Hard Metals by Rapid Sintering Process. International Journal of Refractory Metals & Hard Materials. 22: pp. 197-203.

Hyoung, R. and Deug, J. (2003). Role of Vanadium Carbide Additive during Sintering of WC-Co: Mechanism of Grain Growth Inhibition. Department of Materials Engineering, Sungkyunkwan University, Suwon. pp. 440-746, Korea.

James, M. and Buck, O. (1980) Quantitative non-destructive measurements of residual stresses. *CRC Critical Reviews in Solid State and Materials Sciences.* pp: 61-105.

Jaydeep, S. (2014). In: Devices. Elsevier. Amsterdam

Jones, F., Ryffel, H., Oberg, E., McCauley, C. and Heald, R. (2004). Machinery's Handbook. Industrial Press. USA. California.

Kumar, V., Fang, Z., Wright, S. and Nowell, M. (2006). An analysis of grain boundaries and grain growth in cemented tungsten carbide using orientation imaging microscopy, Metallurgical and Materials Transactions. A 37 (3): pp. 599 - 607.

Lavergne, O., Robaut, F., Hodaj, F. and Allibert, C. (2002). Mechanism of solid-state dissolution of WC in Co-based solutions, Acta Mater. 50 (7): pp. 1683–1692.

Lee H., Kim D., and Hwang N. (2002). Effect of Anorthite Liquid on the Abnormal Grain Growth of Alumina. Journal of the European Ceramic Society. 22: pp. 317–21.

Lin, N., Jiang, Y., Zhang, D., Wu, C., He, Y. and Xiao, D. (2011). International Journal of Refractory Metals & Hard Materials. 29: pp. 509-511.

Luyckx, S. and Love, A. (2006). The dependence of the contiguity of WC on Co content and its independence from WC grain size in WC-Co alloys. International Journal of Refractory Metals & Hard Materials. 24: pp. 75-79.

Luyckx, S. and Mohamed, Z. (2001). Comparison Between V_8C_7 and Cr_3C_2 as Grain Refiners for WC-Co. Materials & Design. 6 (22): pp. 507-510.

Luyckx, S. and Vekinis, G. (1986). On the relationship between the length of Palmqvist cracks and residual surface stresses in WC-Co. NDT International. 19(2): pp. 89-90.

Markström, A., Sundman, B. and Frisk, K. (2005). A revised thermodynamic description of the Co–W–C system. J Phase Equilibrium Diffusion. 26 (2): pp. 152–60.

Montes, F., Valavala, S. and Haselbach, L. (2005). A New Test Method for Porosity Measurements of Portland Cement Pervious Concrete. Journal of ASTM International. 2 (1): pp. 1-13.

Morteza, M., Hamed, A. and Farzad S. (2013). Effect of Cr_3C_2 and VC on the Mechanical and Structural Properties of Sintered WC-10 wt% Co Nano Powders. World Journal of Nano Science and Engineering. 3: pp. 35-39.

Morton, C., Wills, D. and Stjernberg, K. (2005). The temperature ranges for maximum effectiveness of grain growth inhibitors in WC–Co alloys. International Journal of Refractory Metals and Hard Materials. 23: pp. 287-93.

Nan, L., Yuehui, H., Chonghu, W., Quankun, Z., Jin, Z. and Zhongwei, Z. (2012). Fabrication of tungsten carbide–vanadium carbide core–shell structure powders and their application as an inhibitor for the sintering of cemented carbides. Scripta Materialia. 67: pp. 826-829.

Orru, R., Licheri, R., Locci, A., Cincotti, A. and Cao, G. (2009). Consolidation/synthesis of materials by electric current activated/assisted sintering. Material Science and Engineering R-reports. 63: pp. 127-287.

Östberg G. Mechanisms of plastic deformation of cemented carbide and cermet cutting tools. PhD Thesis, Chalmers University of Technology, Sweden, 2005. pp.274–281.

Ostwald, W. (1896). Lehrbuch der Allgemeinen Chemie, vol. 2, part 1. Leipzig, Germany

Owais, M (2013). Impact of pressure on sintering of cemented carbides. KTH Industrial Engineering and Management. Master of Science Thesis Stockholm, Sweden.

Penrice, T. (1987). Alternative Binder for Hard-Materials. Journal of Material Science. Shaping Technol. 5: pp.35-39.

Park, Y., Hwang, N. and Yoon, D. (1996). Abnormal growth of faceted (WC) grains in a (Co) liquid matrix. Metallurgical and Materials Transactions. 27: pp. 2809–19.

Pirso, J., Juhani, K., Tarraste, M., Viljus, M. and Letunovitš, S. (2014). The Effect of VC, TiC and Cr_3C_2 on The Microstructure and Properties of WC-15 wt% Co Hard-metals Fabricated by the Reactive Sintering. International DAAAM Baltic Conference. pp. 24-26.

Pollock C.B, Stadelmaier H.H. (1970). The eta carbides in the Fe–W–C and Co–W–C systems. Metallurgical Transactions. 1: pp. 767–770.

Potgieter. J.H, Thanjekwayo, N., Olubambi, P., Maledi, N.B., and Potgieter-Vermaak, S.S. (2011), The influence of Ru additions on the corrosion behaviour of WC-Co cemented carbide alloys in sulphuric acid, International Journal of Refractory Metals & Hard Materials. 29 (4): pp. 478-487.

Renqi, M., Shaodong, J., Haiyan, C. and Chenyang, S. (2017). Effect of Cobalt Content on Microstructures and Wear Resistance of Tungsten Carbide–Cobalt-Cemented Carbides Fabricated by Spark Plasma Sintering. IOP Conference Series: Materials Science and Engineering, 207.

Roebuck, B. and Bennett, E. (1986). Phase size distribution in WC/Co hardmetal. Metallography. 19 (1): pp. 27–47.

Roebuck, B., Gee, M., Bennett, E. and Morrell, R. (1999) Measurement, “Good Practice Guide No. 20, Mechanical Tests for Hard Metals”, Centre for Materials Measurement and Technology, National Physical Laboratory, Middlesex, UK, pp. 1368–6550.

Scholl, H., Hofman, B., and Rauscher, A. (1992). Anodic polarization of cemented carbides of the type [(WC, M): M = Fe, Ni or Co] in sulphuric acid solution. Electrochimica Acta. 37(3): pp. 447–452.

Schubert W., Bock A., Lux B. (1995). General aspects and limits of conventional ultrafine WC powder manufacture and hard metal production. International Journal of Refractory Metals & Hard Materials. 13: pp 281–96.

Schwarzkopf, P., Kieffer, R. (1960). *Cemented Carbides*. New York: Macmillan.

Shetty, D., Wright, I. Mincer, P. and Clauer, A. (1985). Indentation fracture of WC-Co cements. Journal of Materials Science. 20: pp.1873-1882.

Shing, T., Luckyx, S., Northrop, I., Wolff, I. (2001). The Effect of Ruthenium Additions on the Hardness, Toughness and Grain Size of WC–Co. International Journal of Refractory Metals and Hard Materials. 1 (19): pp. 41-44.

Sivaprahasam, D., Chandrasekar, S. and Sundaresan, R. (2007). Microstructure and mechanical properties of nanocrystalline WC–12Co consolidated by spark plasma sintering. International Journal of Refractory Metals & Hard Materials. 25: pp. 144–152.

Siwak, P. and Garbiec, D. (2016). Microstructure and Mechanical Properties of WC-Co, WC-Co-Cr_3C_2 and WC-Co-TaC Cermet Fabricated by Spark Plasma Sintering. Transactions of Nonferrous Metals Society of China (English Edition). 10(26): pp. 2641-2646.

Siwak., P., Garbiec, D., and Rogalewicz, M. (2017). The Effect of Cr_3C_2 and TaC Additives on Microstructure, Hardness and Fracture Toughness of WC-6 wt% Co Tool Material Fabricated by Spark Plasma Sintering. Materials Research. 20 (3): pp. 780-785.

Sommer, M., Schubert, W., Zobetz, E. and Warbichler, P. (2002). On the formation of very large WC crystals during sintering of ultrafine WC–Co alloys, International Journal of Refractory Metals & Hard Materials. 20. pp. 41–50.

Sun, L., Chengchang, J., Ruijun, C. and Chenguang, L. (2008). Effects of Cr_3C_2 Additions on the Densification, Grain Growth and Properties of Ultrafine WC-11Co Composites by Spark Plasma Sintering. International Journal of Refractory Metals & Hard Materials. 26: pp. 357-361.

Sun, L., Jia, C. and Xian, M. (2007). A research on the grain growth of WC–Cocemented carbide. International Journal of Refractory Metals & Hard Materials. 25: pp. 121–4.

Sutthiruangwong, S. and Mori, G. (2003). Corrosion properties of Co-based cemented carbides in acidic solutions. International Journal of Refractory Metals & Hard Materials. 21(4): pp. 135-145.

Tillamann, W. Elrefaey, A. Wojarski, L. (2013). Advances in Brazing. Brazing of Cutting Materials. Science, Technology and Applications. Technical University of Dortmund, Germany. pp. 423-471.

Tomas A., Charles R., Waltraud, M. and Charles, P. (2015). Effects of time, temperature, and pressure on the microstructure of spark plasma sintered silicon carbide. Journal of Ceramic Processing Research. 16(3): pp. 303-307.

Upadhyaya G.S. (2001). Materials Science of Cemented Carbides - An Overview. Materials and Design. 22: pp. 483-489.

Underwood, E. (1970). Quantitative stereology, Addison Wesley, Reading, MA.

Wang, X., Fang, Z. and Sohn, H. (2008). Grain growth during the early stage of sintering of nanosized WC–Co powder, International Journal of Refractory Materials & Hard Material. 26 (3), pp. 232–241.

Warren, R. (1968). Carbide grain growth during the liquid phase sintering of the alloys NbC-Fe, NbC-Ni and NbC-Co, Journal of Less Common Metals. 17: pp. 65–72.

Wei, S., Sun, Y., Yang, H., Zhang, X. and Ruan, J. (2015). Effect of TaC on Microstructure and Mechanical Properties of Coarse-Grained WC-9Co Cemented Carbides. Transactions of Nonferrous Metals Society of China. 25 (4): pp. 1194-1199.

Wentzel, E. and Allen, C. (1997). The erosion-corrosion resistance of tungsten-carbide hard metals. International Journal of Refractory Metals & Hard Materials. 15 (3): pp. 81–87.

Whitefield, D.J. (2011). “The Optimisation and Evaluation of VC-WC-Co Hardmetals”, PhD thesis, University of the Witwatersrand, Johannesburg.

Whitefield, D.J. Luyckx, S., Witcomb, M.J. and Cornish, L.A. (1997). Microstructure and properties of fine-grained WC-VC-Co hardmetal with cobalt content ranging from 10 to 15 wt %, Proceedings of the 14th International Plansee Seminar, 2, pp. 477–484.

Wittmann, B., Schubert, D. and Lux, B. (2002). WC grain growth and grain growth inhibition in nickel and iron binder hardmetals. International Journal of Refractory Metals & Hard Materials. 20: pp. 51–60.

Zackrisson, J., Jansson, B., Uphadyaya, G. and Andren, H. (1998). WC-Co Based Cemented Carbides with Large Cr_3C_2 Additions. International Journal of Refractory Metals & Hard Materials. 16: pp.417-422.

Zhong, Y. and Shaw, L. (2011). Growth mechanisms of WC in WC–5.75 wt% Co, Ceramic International. 37 (8). pp.3591–3597.

Zhu, H., Huang, W. and Zhao, F. (2003). Preparation of Nanocrystalline WC-10 wt % Co-0.8 wt% VC by Spark Plasma Sintering. Journal of Materials Science Letters. 22: pp. 1631–1633.

8. Appendix

Publication from the work

S.T. Luthuli, L.A. Cornish and D.J Whitefield, Effect of VC, Cr_3C_2 and Ru Additives on Mechanical Properties of WC-10Co, 56th Annual Microscopy Society of Southern Africa Conference, Volume 48, p. 39, Mykonos Resort, Langebaan, Western Cape, 1st – 5th December 2019. ISBN 978-0-6398435-0-6

EFFECT OF VC, Cr_3C_2 AND Ru ADDITIVES ON THE MECHANICAL PROPERTIES OF WC-10Co

S.T. Luthuli , L.A. Cornish and D.J. Whitefield

School of Chemical and Metallurgical Engineering, University of the Witwatersrand, and DST-NRF Centre of Excellence in Strong Materials, hosted by University of the Witwatersrand, Johannesburg

Tungsten carbide cobalt, WC-Co, is a composite of tungsten particles with metallic cobalt as a binder, usually made from powders, pressed and sintered at a high temperature[1]. Cemented carbides possess superior mechanical properties and excellent abrasive wear resistance[2], and are commonly used in cutting tools, drilling and wear resistant machine parts. Typical hard-facings on softer materials include WC-Co of varying Co contents. Under abrasive wear conditions, the binder is rapidly removed (being softer), which then allows the hard WC particles to be easily removed[3]. Thus, a technique for strengthening the binder is needed.

To study physical and mechanical properties of WC-Co, samples of different compositions were made. As-received WC, Co, Ru, VC and Cr_3C_2 powders were analysed in a Mastersizer 2000 for particle size, then powders of different compositions, WC-10Co powder mixtures with different additions, were milled in a planetary ball mill with a 4:1 ball-to-powder ratio. The different powder mixtures were then sintered in a spark plasma sintering furnace at 1150°C and 50 MPa for 8 minutes dwell-time. The sintered samples were tested for density in a Sartorius ED224S machine. Specimens were prepared metallographically, by grinding and polishing, and etched with Murakami's reagent. Microstructural analysis was done in a Zeiss FE-SEM with energy dispersive X-ray spectroscopy to study the microstructures and analyse the overall and phase compositions.

The microstructure of the samples are shown in Figs. 1-3. There are limit significant microstructural differences. Fine WC grains were seen in all the samples, as a result of Ru, VC and Cr_3C_2 additives being partially successful as grain growth inhibitors. Figure 2 shows a wide grain size range with many WC/WC contacts without a continuous Co binder. In general, the Co solid solution was not well distributed between the WC grains and as a result Co pools were formed. The VC and Cr_3C_2 dissolved in WC, and Ru dissolved in the binder.

An increase in hardness was observed as a results of the additives introduced to the WC-10Co base material. Hardnesses were calculated to be 1709 ± 36HV_{30} (Fig. 1), 1737 ± 42HV_{30} (Fig. 2) and 1656 ± 35HV_{30} (Fig. 3) compared to the WC-10Co base material with 1564 ± 75HV_{30}. The best additive for improved hardness was found to be Cr_2C_3.

References:
1. Upadhyaya, G. (2002) Materials and Design 22(6), 483.
2. Chabretou, V., Alibert, C. and Missiaen, J. (2003) J. Mater. Sci. 38(12), 2581.
3. Siwak, P. and Garbiec, D. (2016) Nonferrous Met. Soc. China, 26(10), 2641.

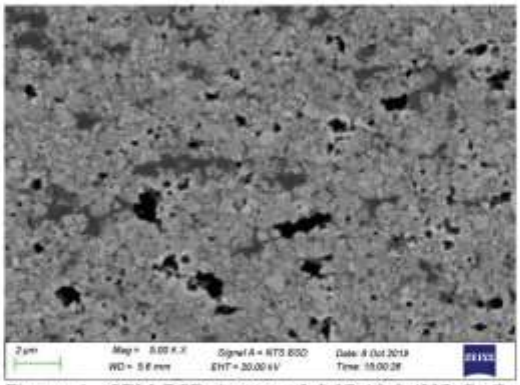

Figure 1. SEM-BSE image of WC-10-0.4VC-Cr_3C_2 showing Co pools (dark contrast) and WC (light).

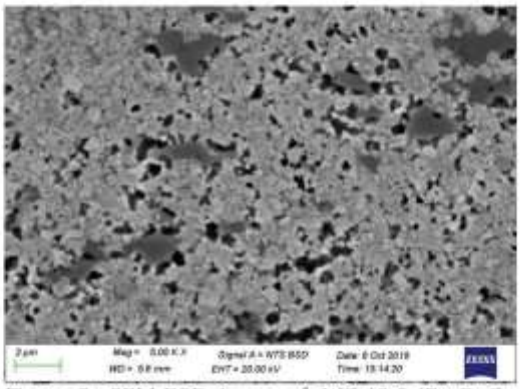

Figure 2. SEM-BSE image of WC-10-0.4Ru-Cr_3C_2 showing WC (light) and Co (dark contrast) with different sized WC grains.

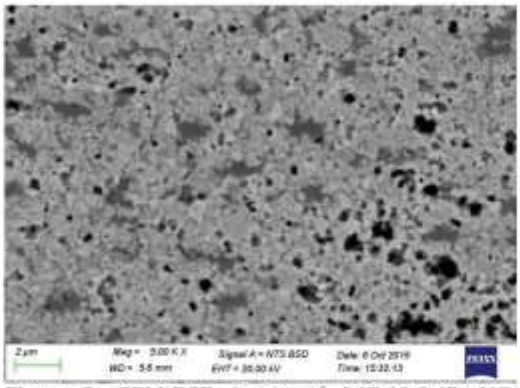

Figure 3. SEM-BSE image of WC-10-0.4Ru-VC showing WC (light) and Co (dark contrast) with more rounded WC particles.

Corresponding author: 900957@students.wits.ac.za